DISSERTATION

# QUANTUM DOT STUDIES WITH TIME-RESOLVED SUPER-RESOLUTION MICROSCOPY

Submitted by

Megan Kathryn Dunlap

Department of Chemistry

In partial fulfillment of the requirements

For the Degree of Doctor of Philosophy

Colorado State University

Fort Collins, Colorado

Summer 2021

Doctoral Committee

Advisor: Alan Van Orden
Co-advisor: Martin Gelfand

Diego Krapf
Amy Prieto
Gzegorz Szamel

ABSTRACT

QUANTUM DOT STUDIES WITH

TIME-RESOLVED SUPER-RESOLUTION MICROSCOPY

Quantum dots (QDs) are semiconductor nanoparticles whose optical properties make them ideal candidates for a myriad of applications including fluorescence imaging and light harvesting technologies. They are highly emissive and their stochastic switching between states of low and high intensity, called blinking, lends them particularly well to super-resolution (SR) microscopy studies. This thesis is devoted to the development and application of a SR microscope with exceptionally high temporal resolution, so that the fluorescence lifetime, intensity, and emitter location can be simultaneously monitored. This time-resolved SR microscope is used to characterize CdSe/CdS core/shell QDs and clusters of QDs. Small clusters of ~2-5 QDs exhibited fluorescence intensities and lifetimes indicative of directed energy transfer, and regions were resolved within the clusters that were responsible for donating and accepting energy. Correlated images of the same clusters with scanning electron microscopy were used to verify the true distances between QDs in an attempt to confirm the distance-dependence of the Förster energy transfer rate. A new analysis method was developed for resolving non-blinking emitters based on the lifetime information accessible with the time-resolved SR microscope.

# ACKNOWLEDGEMENTS

Many people have been a source of inspiration and support during my time in graduate school. I am extremely grateful to my advisor, Alan Van Orden, who gave me a wonderful environment to grow as a scientist. His ceaseless guidance and optimism made research enjoyable. I am also thankful for the support of my co-advisor, Marty Gelfand, who took a constant interest this research, and provided careful help and feedback with theoretical aspects of my work. I am grateful to all the people that I have met and worked with in the Van Orden group, including John Gann, Farshad Abdollah-Nia, David Thoma, and Courtney Hazelton-Harrington.

I had the pleasure of conducting research at Los Alamos National Laboratory for three years, and the opportunity to work with many excellent scientists while I was there. I would like to thank Peter Goodwin and James Werner, who welcomed me into their fluorescence microscopy group, providing guidance and resources. I am indebted to Peter Goodwin, who was my mentor at Los Alamos National Laboratory. His insightful suggestions and assistance with experiments helped me overcome many stumbling blocks in research, and his patience and generosity were greatly appreciated. I am thankful to Duncan Ryan, whose attentive guidance with experiments and data analysis drove this work forward.

Jen Hollingsworth and her group were instrumental in this project, providing me with samples and answering all of my questions related to synthesis and quantum dots over the years. I am thankful to Somak Majumder, whose samples have provided me with a seemingly endless source of light and questions to explore. I am also grateful to Chris Sheehan for his careful correlated electron microscopy imaging.

I am thankful for the support and friendship of my officemate in Los Alamos, Alejandra Londoño-Calderon. I enjoyed being a part of the chemistry department at CSU and am thankful for the friendship of fellow graduate students Clara Tibbetts and Yusef Farah. My coursework was wonderful thanks to the teaching of Grzegorz Szamel, Amy Prieto, Martin McCullagh, Amber Krummel, and Justin Sambur. I am especially grateful to Karolien Denef and Claudia Boot, who were amazing mentors during my teaching assistantship in the Central Instruments Facility at CSU.

Lastly but most importantly, I am thankful for the boundless love and support of my parents, Jean and David, and my brother, Matthew.

DEDICATION

To my family

TABLE OF CONTENTS

LIST OF FIGURES

# CHAPTER 1. INTRODUCTION

Nanocrystals made up of hundreds to thousands of semiconductor atoms first drew attention in the 1980s when researchers observed their size-dependent optical properties caused by confinement of the electron-hole pair (the exciton) to spaces smaller than the exciton radius[1]. These crystals act like spherical potential wells, giving rise to discrete atomic-like energy transitions, and are named "quantum dots" (QDs) after this effect[2,3]. The valance and conduction bands edges of the QD where the hole and electron respectively reside are analogous to the highest occupied molecular orbital (HOMO) and lowest unoccupied molecular orbital (LUMO) of a molecule, and the energy between them can be adjusted based on the size of the QD. For CdSe QDs, arguably the most extensively studied QDs because their photoluminescence can be tuned across the visible spectrum, the exciton radius is 5.6 nm[4]. The diameter of the CdSe QDs examined in this thesis are ~5.6 nm, putting our system in what is referred to as the "strong confinement regime"[5].

Aside from their tunable band gaps, QDs exhibit remarkable photostability, quantum yields, and thermal stability, making them ideal candidates for optoelectronic devices such as solar cells and light emitting diodes (LEDs), for use in lasing technology, and for imaging and biomedical applications[6–11]. QDs also exhibit an intermittency in their photoluminescence, temporarily and stochastically switching between emissive "ON" states to non-emissive or less emissive "OFF" states[12–15]. This phenomenon is commonly referred to as blinking, and it can be desirable or not depending on the application. For the super-resolution microscopy work done in this thesis, blinking is essential, as we will discuss later. In an effort to understand the physical

properties that govern blinking, much research has been devoted to characterizing and modeling the behavior[12–14,16–22].

Based on spectroscopic studies of single QDs, the most widely accepted explanation for blinking is that it occurs when the QD becomes charged because one of the charge carriers associated with the exciton, the electron or the hole, becomes trapped on the surface or ejected entirely from the QD[20,23]. The remaining charge triggers a process called Auger recombination in which subsequently formed excitons transfer their energy to the extra charge, allowing nonradiative relaxation to occur through phonon modes. The rate of Auger recombination is much higher than the radiative decay of the exciton, so the system is effectively in the OFF state. This persists until the trapped charge returns and neutralizes the QD, after which the ON state is resumed.

Since their first discovery, the photostability and quantum yields of QDs have been improved upon by growing inorganic shells on their surface, which reduce the effects of environmental changes, photo-oxidation, and surface chemistry on the photoluminescence properties[24–28]. Past studies in our group focused on the photoluminescence behavior of CdSe/ZnS (core/shell) QDs, while our more recent studies have examined CdSe/CdS QDs and this is the system examined in this thesis. A CdSe/CdS QD has a band structure referred to as quasi type-II because the conduction and valance bands of the CdS shell lie below those of the CdSe core. This means the electron can migrate throughout the core and shell whereas the hole is confined only to the core. For CdSe cores with exceptionally thick shells, for example 16-19 monolayers of CdS, there is nearly a complete suppression of blinking[29] . The QDs studied in this thesis have ~5 monolayers of CdS, and in this case the blinking behavior is still prevalent.

Multiple QDs in close proximity will transfer energy to one another through dipole-dipole coupling that is referred to as Förster resonance energy transfer (FRET)[30–32]. For some QD technologies, such as QD-LEDs, energy transfer can harm their performance[29], whereas for other technologies, such as luminescent solar concentrators[33], efficient nonradiative transfer is desired. Either way, the characterization and control of energy transfer among QDs is valuable and has been the subject of many studies, both at the single molecule and ensemble level. FRET is described in the context of energy transfer between a donor QD and an acceptor QD and has a rate

$$F = \frac{1}{\tau_D}\left(\frac{r_0}{d}\right)^6 \tag{1.1}$$

that depends inversely on the distance $d$ between donor and acceptor pair raised to the sixth power[34]. In Eqn. 1.1, $\tau_D$ is the relaxation rate of the isolated donor emitter, and $r_0$ is called the Förster radius, which is the separation distance $d$ at which the donor relaxation rate $1/\tau_D$ for an isolated QD is equal to $F$. The Förster radius depends on the donor quantum yield, the relative orientations of the donor and acceptor transition dipole moments, and the overlap of the donor emission wavelength and the acceptor absorption coefficient[1]. It has been measured experimentally in thin films of mixed donor and acceptor QDs[31,35–37] or in bilayers of donor films and acceptor films[38–40] by monitoring the decreased lifetime,

$$\tau_{DA} = \frac{\tau_D}{1 + F\tau_D} \tag{1.2}$$

of the donor emission in the presence of the acceptor. For these referenced studies, a variety of QDs materials, sizes, and ligands have been used, and $r_0$ varied substantially, ranging between ~4-

[1] It is convenient to know the relationships $r_0 = d\left(\frac{\tau_D}{\tau_{DA}} - 1\right)^{1/6} = d(F\tau_D)^{1/6}$.

12 nm. Curiously, several QD FRET studies have pointed out a discrepancies in their experimentally measured $r_0$ compared to theoretical predictions[35], while others have reported reduced distance dependencies of $1/d^4$, suggesting the Förster model may be inadequate for describing the energy transfer among QDs[39].

In an effort to better characterize the energy transfer between QDs, several groups, including our own, have used single molecule spectroscopic techniques to probe the interactions among small clusters of 2-5 QDs. These systems can transfer energy but are small enough to exhibit emission behavior that does not suffer from ensemble averaging, and their behavior provides clues about their interactions. Our group's interest in these systems began in 2006 when Yu and Van Orden observed more rapid blinking of CdSe/ZnS QDs in clusters compared to single QDs[41]. Later, Shepherd, et. al. observed enhanced blinking along with the presence of a lower intensity and shorter lifetime emission within clusters that could be explained with a model of energy transfer to QDs with smaller band gaps[42], and Whitcomb, et. al. showed that the altered blinking was a consequence of the ON/OFF switching of acceptor QDs. In addition to lifetime and intensity information, some spectroscopic methods allow one to collect the time delays between single photon arrivals and explore the correlations between these photon pairs. Members of our group found that energy transfer was also evidenced in the photon pair correlations[43].

To study the relationship between the size and structure of clusters and their energy transfer efficiency, and to uncover the roles of individual QDs in clusters as donors or acceptors, our group then began imaging the clusters with fluorescence microscopy. The spatial resolution of conventional fluorescence microscopy is limited by the diffraction of light so that emitters closer than ~200 nm cannot be resolved. Uncovering structural information about the clusters required a method with spatial resolution approaching the diameter of the QDs, which was attainable with

super-resolution (SR) microscopy. This technique relies on identifying the peak of the emission profile, the emission centroid, so that *single* emitters can be located with high precisions between 1-100 nm depending on the efficiency of the detection scheme and brightness of the emitters[44,45]. Unfortunately, if multiple emitters contribute to the emission profile, the centroid is located at a weighted average of their individual positions, and there is nothing super about that. However, if the emitters undergo blinking, the centroid position will shift among their individual locations in time. Compiling these centroid locations and applying filtering techniques such as intensity thresholding to remove centroids for which multiple emitters likely contributed to the emission profile, one obtains a SR image. Thus the inherent blinking and brightness of QDs makes them excellent emitters for SR microscopy[46–48].

In our group, Ryan, et. al. imaged clusters of CdSe/ZnS QDs with SR microscopy and resolved multiple regions within the clusters by taking advantage of their blinking properties[49,50]. Some regions had significantly higher intensity that others, and by imaging the same clusters with scanning electron microscopy (SEM), the authors were able to see which QDs within the cluster were responsible for different quantum yields. Highly emissive QDs were hypothesized to be energy acceptors while those with lower intensity were hypothesized to be energy donors. Additionally, the authors also observed that the intensity of the emission from clusters was lower than would be expected based on the number of QDs measured in the SEM images, suggesting that energy transfer to QDs that are predominantly in the OFF state might be occurring. However, it was equally possible that the different quantum yields of the QDs in the clusters were independent of energy transfer and caused entirely by heterogeneity among the QDs. To further probe these findings, our group developed a time-resolved SR microscope that was capable of accessing both the quantum yield *and* lifetime of the photoluminescence of the QDs.

This thesis discusses the development of this microscope and its accompanying data analysis tools, as well as its application to the study of CdSe/CdS QDs.

Chapter 2 describes the time-resolved SR microscope setup and its application to the study of single and clustered CdSe/CdS QDs[51]. We found a correlation between shorter lifetime and lower intensity emission within QD clusters that was consistent with the behavior expected for donor QD(s) in the presence of acceptor QD(s). For single isolated QDs, we observed the emission centroids distributed about a single mean location with ~5 nm precision every 0.1 sec (with 10,000 collected counts). For QD clusters, we observed the centroids were distributed about multiple mean locations, from which we attempted to infer the underlying structure of the QD clusters. Moreover, different regions of the SR image were revealed to have different lifetimes and intensities, allowing us to hypothesize about the donor and acceptor roles of different portions of the cluster. We hypothesized that directed energy transfer would be facilitated by the ±1 nm size distribution in our samples, which would cause a distribution in the band gaps of the QDs and allow them to act as donors and acceptors.

Chapter 3 details how we located the emission centroid with our detection scheme. We used maximum likelihood estimation (MLE) to do this, which meant maximizing a likelihood distribution (formulated in Section 3.1) for the location of the emitter given the counts arriving in the pixels of our camera. Special care had to be taken because our detection scheme had only four pixels, so the information we could extract about the system was limited. We found that we could locate an emitter and compute the total number of emitted counts with MLE using only the counts arriving in the four pixels, but this required knowledge of the emission PSF. Unfortunately, the PSF could not also be determined from MLE of a four-pixel image, unless we already knew the

emitter location. This led us to develop an independent method for measuring the PSF which is described in Section 3.3.

Chapter 4 returns to the study of CdSe/CdS QD clusters, this time introducing scanning electron microscopy (SEM) images of clusters that were also imaged with the time-resolved SR setup. This provided us with a way of examining how the number of QDs and their separations from one another impacted their photoluminescence properties. In Section 4.1, we highlight images of pairs of QDs that have decreasing separation distances. In Section 4.2, we present some simple kinetic models to describe the quantum yield, photon arrival time distribution, and average photon arrival time for single emitters, and pairs of both noninteracting and interacting emitters. The models for a single emitter are used to interpret the behavior of isolated QDs in Section 4.3, for which we find that a model incorporating a single radiative decay pathway and competing nonradiative decay pathway does a very good job describing our data. We return, in Section 4.4, to the pairs of QDs. Unlike the clusters from Chapter 2, we find that we cannot confirm the presence of energy transfer among these cluster. Given the substantial variation in the lifetimes of the single QDs, the lifetime and intensity variations observed in clusters may be completely attributed to the heterogeneity in the individual QD photoluminescence. We also interpret the QD pair behavior in terms of the kinetic models we presented for emitter pairs. Ultimately, we find that we are, in the best-case scenario, one parameter short of being able to quantify the Förster transfer rate among these QDs.

Chapter 5 returns to the subject of localizing a single emitter with MLE. An assumption of continuous wavelength (CW) excitation went into the formulation of the likelihood distribution that we used in the analysis in Chapter 3. Although this formulation is prevalent in the literature, it is technically an inappropriate model for our purposes because we excite the emitters with pulsed

excitation. To remedy that, we have formulated a likelihood distribution for of the location of an emitter that is undergoing pulsed excitation. Conveniently, our approach allows us to fold in information about the photon arrival times that we also collect with our setup. In maximizing this new distribution for the emitter location, we find that it can achieve superior localization precision for emitters in the presence of high background. To the extent which we have applied MLE, we find that both the likelihood distribution from Chapter 3 and our newly formulated likelihood distribution for pulsed excitation provide the same location for single emitters.

Chapter 6 extends the pulsed likelihood distribution derived in the previous chapter so it includes temporal information about the photon arrival times in each pixel. We show that for the time-resolved MLE, multiple emitters can be simultaneously located if their lifetimes are sufficiently disparate. In other words, we demonstrate the ability to super-resolve non-blinking emitters, thanks to the temporal information provided by our microscope. We apply this method to simulated emitters in Section 6.1, for which emission centroids spaced 5 nm apart are resolved.

# CHAPTER 2. Examining Quantum Dot Interactions Part 1: Time-Resolved Super-Resolution Imaging

In this chapter, we present an overview of our time-resolved SR microscope before delving into data we collected on CdSe/CdSe core/shell QDs which highlights the capabilities of the microscope[2]. This work was motivated by previous studies of small clusters of CdS/ZnS QDs (2-5 QDs in contact) by our group, dating back to 2004, in which the presence of energy transfer among QDs was indicated by correlations between lower intensity/shorter lifetime emission and higher intensity/longer lifetime emission[42,52]. Additionally, camera-based SR imaging studies of CdS/ZnS QD clusters conducted by past members of our group revealed localized regions of high and low intensity emission within clusters that may have been facilitated by energy transfer[49]. As we will see, the time-resolved SR microscope allows us to explore both of those findings by simultaneously monitoring the arrival times of photons with sub-nanosecond time resolution and monitoring the emission centroid location with ~5 nm precision[3]. Ultimately, the

[2]Some of the text and figures in this chapter appear in our Applied Phys. Letters paper[51]. For this paper, Megan Dunlap collected and analyzed the data, and wrote the manuscript. Duncan Ryan provided technical assistance with the optical alignment and provided feedback during the development of the localization algorithm. Peter Goodwin assisted with data interpretation, photon counting electronics, and optics. James Werner provided the equipment for the time-resolved super-resolution microscope and assistance with the single photon counting electronics. Jennifer Hollingsworth and Somak Majumder provided the QD samples and assisted with data interpretation. Martin Gelfand assisted with the development of the localization algorithm and data interpretation. Alan Van Orden assisted with developing of the microscope and localization algorithm. All authors contributed to editing the manuscript.

[3]Precision scales with the square root of the number of detected photons, and ~5 nm precision is achieved with $10^4$ detected photons.

spatial mapping of the emission intensity and lifetime allows us to identify energy transport pathways among QDs within clusters.

## 2.1: Time-resolved super-resolution microscope overview

Numerous optical microscopy techniques have been developed in the past two decades that surpass the resolution limits imposed by the diffraction of visible light, such that emitters separated by less than ~200 nm can be spatially resolved[53]. Single-molecule localization microscopy (SMLM) is a subset of these super-resolution (SR) techniques in which multiple closely spaced emitters can be resolved by locating the centroid of the emission profile of single molecules with a high degree of precision[54]. Resolution in the tens of nanometers is typical, and ~1 nm resolution has been reported under favorable conditions[55,56]. Though emission is typically collected by a charge-coupled device (CCD) camera or a complementary metal-oxide semiconductor (CMOS) camera, several recent SR demonstrations have greatly improved the temporal resolution by employing single-photon avalanche photodiode (SPAD) detectors in conjunction with time-correlated single-photon counting (TCSPC) hardware[57–59]. In TCSPC, which is illustrated in Fig. 2.1, the arrival time of each registered photon relative to the start of the experiment (the time of day), called the "macro-time", and the arrival time relative to the excitation laser pulse, called the "micro-time", are recorded with resolutions down to ~50 ps[60,61]. The simultaneous acquisition of TCSPC data and SR images allows for observation and characterization of dynamic processes that are inaccessible in conventional camera-based SR imaging.

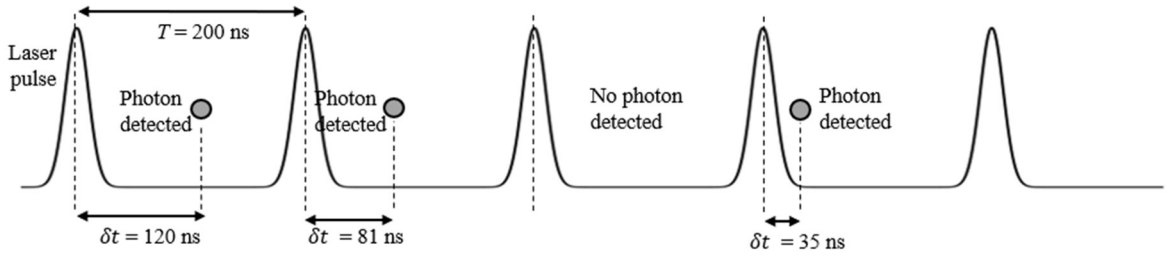


**Figure 2.1 Time-correlated single photon counting**. Laser pulses with a period *T* excite the system. Electronics record the micro-time δt, the interval of time that elapses between the detection of an emitted photon and the most recent laser pulse preceding the photon detection, which we use to determine the lifetime of the emission. In addition, the amount of time that elapsed between the start of the experiment and the arrival of each photon is recorded. We use that information to determine the number of counts that arrived in each pixel during a specified segment of time.

To date, high spatiotemporal resolution imaging has been implemented with two different detection schemes: arrays of optical fibers that are coupled to individual SPAD detectors, and SPAD array detectors. The latter has been used to resolve emitters spaced by ~80 nm[58], and a theoretical study used photon pair correlations to accurately extract the number of non-interacting emitters in an image containing overlapping emission profiles[62]. Additionally, the array's timing resolution has been exploited for fluorescence lifetime imaging with a resolution slightly better than the diffraction limit[59]. Despite the large number of pixels (256 to 66,000) within SPAD arrays, optical fibers coupled to a small number of individual detectors (4 to 16) offer a competitive alternative because they have higher collection efficiencies[61]. In the context of SR imaging, Israel et al. has located emission centroids based on the photons collected by 16 optical fibers coupled to SPAD detectors[57]. In this study, the TCSPC data was used to identify and reject the contribution from multiple emitters based on photon pair correlations, and that processing method was shown to aid in resolving two emitters separated by ~100 nm.

Our time-resolved SR setup also employed optical fibers coupled to SPAD detectors. It was adapted from a similar optical configuration developed by several members of our team for 3-D tracking of single molecules in solution[63–66]. Fig. 2.2 displays a diagram of the

microscope, and a more detailed setup description is provided in Section 2.4. In brief, 485 nm pulses with a width of ~100 ps were delivered at a frequency of 5 MHz and focused onto the surface of a glass coverslip. QDs were sparsely dispersed on the coverslip, and the piezoelectric stage was raster scanned to locate photoluminescent spots from individual QDs and QD clusters. The emission from each spot was collected by an objective and then focused by a tube lens, resulting in an overall 250× magnification of the emission PSF. A 2 × 2 bundle of square optical fibers was placed at the focus of the tube lens, and the fibers transmitted the emission to four single photon counting avalanche photodiode (APD) detectors. Each time a detector registered a photon, it sent a pulse to the TCSPC hardware. Another pulse called the "sync pulse" was also sent from the laser driver to the TCSPC hardware each time an excitation pulse was released. The hardware recorded the time difference between the sync and the detector pulse to measure the micro-time, and it recorded the total number of sync arrivals in a given time window to measure the macro-time.

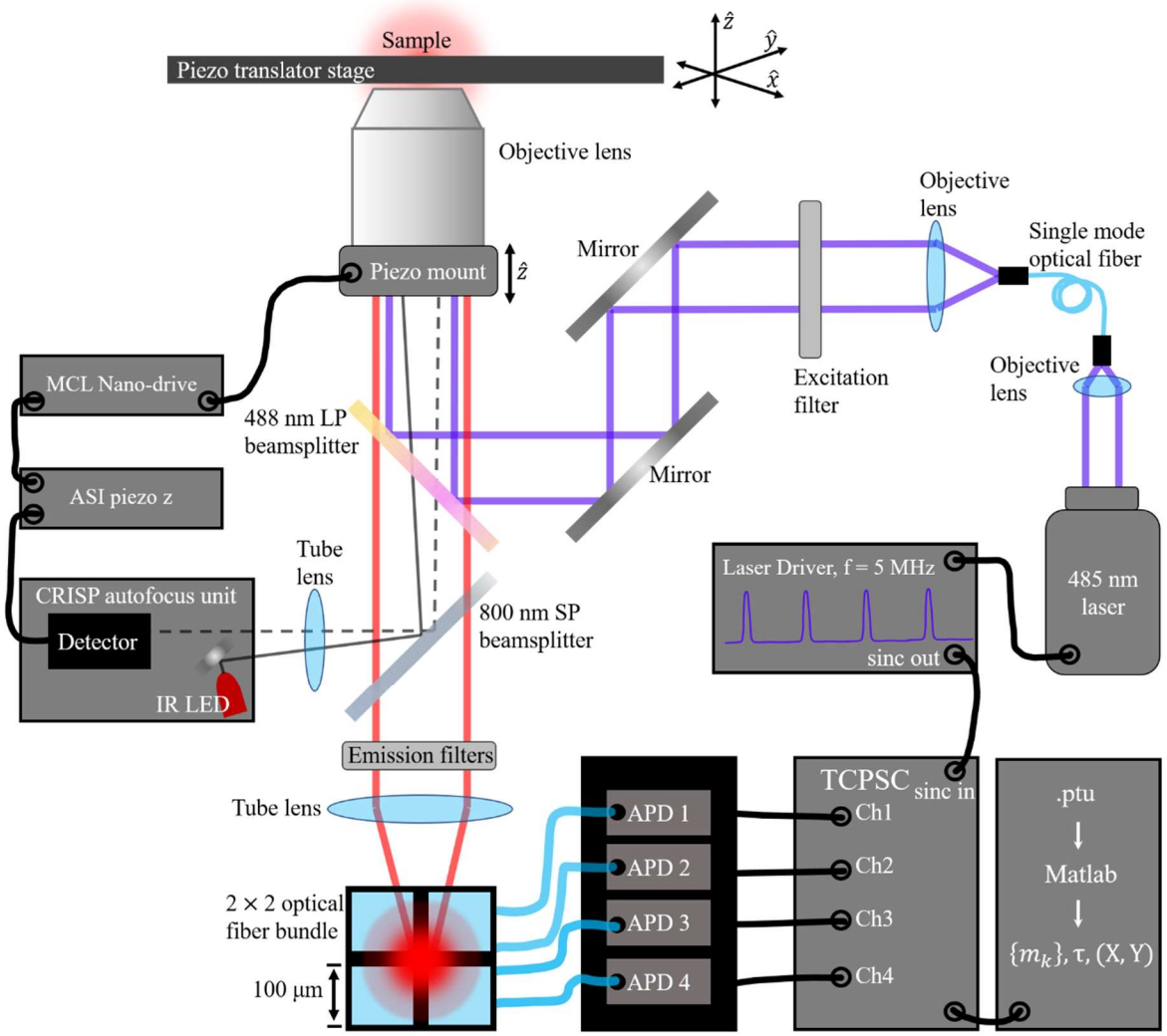


**Figure 2.2 Time-resolved super-resolution microscope.** 485 nm pulses delivered at a frequency of 5 MHz were directed to an objective lens that focused the light on the surface of a glass coverslip where QDs were dispersed. The piezo stage was raster scanned to identify QDs on the surface and place them in the center of the probe region for observation. The z focus was maintained by adjusting the height of the objective with a piezo mount. Feedback for that was provided by an autofocus unit that monitored an image of scattered infrared (IR) light from the surface of the sample. The 850 nm IR light was directed to the objective with an 800 nm short pass (SP) dichroic beamsplitter. The QD emission was collected by the objective, and transmitted by the 488 nm long-pass (LP) dichroic beamsplitter and SP beamsplitter. A 800 nm SP filter blocked stray IR light that was leaked by the SP beamsplitter, and a 488 nm LP filter blocked stray excitation light that was leaked by the LP beamsplitter. A tube lens focused the emission onto a bundle of four optical fibers. The fibers act like pixels, directing the light to four avalanche photodiode detectors that send a pulse to TCSPC hardware upon registering each photon. Using these arrivals in conjunction with the arrivals of the sinc pulse from the laser driver, the micro-times and macro-times corresponding the photon arrivals in each detector were recorded.

Before collecting data, the microscope stage was adjusted so that each sample was in the center of the probe region. Counts were then recorded for 500-1,000 sec from each photoluminescent spot. The binary data from the TCSPC hardware was saved, and then read and analyzed with Matlab. From the macro-times, we determined the average number of counts $m_1$, $m_2$, $m_3$, and $m_4$ that were collected in each of the pixels for every 100 ms time window $\Delta t$. From the micro-times, we determined the lifetime $\tau$ of the emission. In this chapter, we define $\tau$ as the average of the micro-times recorded during each $\Delta t$. (Later on, we will histogram the micro-times and find the lifetimes from that distribution.)

It was necessary to maintain the z position of the sample throughout each experiment to preserve the PSF size. For reasons that will be described in Section 3.3, this must be provided to the localization algorithm, but we cannot measure and monitor it while we acquire data from QDs. This is problematic because the objective drifts in z over the course of an experiment, significantly altering the PSF size. To prevent this, we maintained the distance between the sample and objective using a commercial autofocus unit that imaged scattered infrared light off the surface of the coverslip. As the focus changed (due to drift or adjusting the position of the stage to examine a new fluorescent spot), the image of the scatter changed. In turn, that change was used to generate a voltage for driving a piezoelectric mount that adjusted the z position of the objective. The PSF widths had to be re-measured and the autofocus unit relocked each time the z position was adjusted to maximize the counts. For QDs on a glass coverslip, it was necessary to do this once per coverslip; the PSF size remained constant as long as the autofocus remained on, regardless of adjustments to the microscope stage.

The procedure for measuring the PSF width is detailed in Section 3.3. Briefly, measured the PSF by placing a single QD in the center of probe region and acquiring data before and after

moving the stage by 50 nm. We located the emission centroid with MLE for data collected before and after the movement, and then we solved for the PSF width that would allow the distance between the calculated centroid positions to agree with the 50 nm true distance. For these experiments, the FWHM of the PSF in the image plane was ~100 μm, which happened to be equal to the width of each optical fiber.

## 2.2: Interpreting time-resolved images of single QDs

Samples were prepared by spin coating nanomolar solutions of QDs in toluene onto the surface of glass coverslips that had been plasma cleaned and silanized with (3-Aminopropyl) triethoxysilane (919-30-2) via vapor deposition. Spin coating was done at 5,000 rpm and 50 μl of the solution was deposited dropwise, resulting in a coverage of ~0.01 QDs or QD clusters/$\mu m^2$ on the surface of the coverslip. The QDs were synthesized by a member of the Hollingsworth group at Los Alamos National Laboratory using the synthesis described by Chen, Bawendi, et. al.[67]. This produced cores with ~5.6±0.6 nm diameters and total particle diameters of 9±1.0 nm, as measured from SEM images of the samples (displayed below in Fig. 2.3a and b, respectively). Octadecylamine, octadecene, and primarily oleates were present after the shell growth that acted as stabilizing ligands for the QDs; enough ligand was present such that the QDs formed a monodisperse colloid after being washed[4] and resuspended in toluene.

[4] For washing the QDs, we added 1 part hexane and 8 parts acetone to 1 part of the QDs in the synthesis solution, centrifuged the solution at 5000 rpm for 7 minutes, and then discarded the solvent and left the precipitated QDs to dry in air for several minutes. The acetone precipitated the QDs without displacing their ligands[106]. The QDs were then resuspended in hexane and the process of adding acetone, spinning, and drying was repeated two more times. Lastly, the QDs were resuspended in toluene.

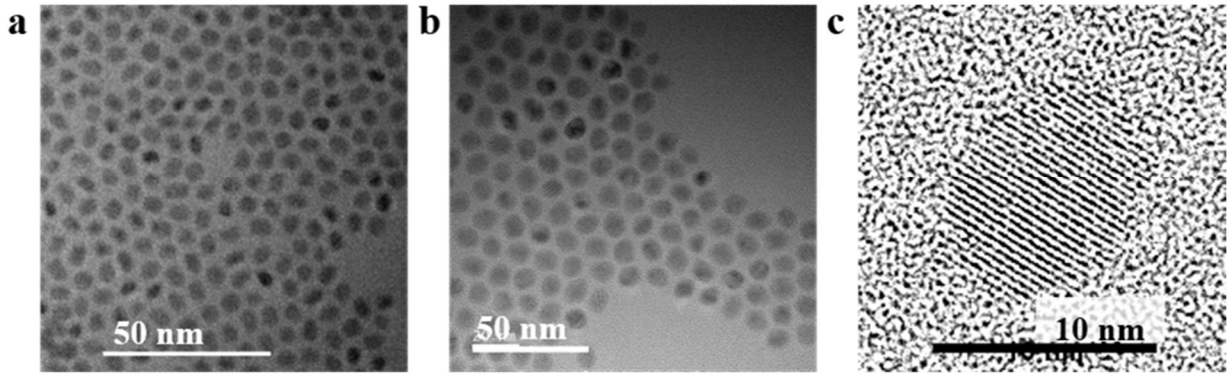


**Figure 2.3 Scanning electron microscopy (SEM) images of CdSe/5CdS QDs.** (a) The CdSe cores have a size distribution of 5.6±0.6 nm. (b) The CdSe/CdSe QDs with ~5 monolayers of CdSe shell have a size distribution of 9±1.0 nm. (c) A high-resolution SEM image of a single CdSe/5CdS QD shows the crystal lattice of the QD. Images (a) and (b) were collected by Joanna Casson, Los Alamos National Laboratory, and (c) was collected by John Watt, Los Alamos National Laboratory.

The average values for $\tau$ and the emission intensity $I = \sum_{k=1}^{4} m_k$, varied from QD to QD, as did the dynamics and distributions of those observables. To illustrate typical trends that existed in all single QDs, we will highlight data from a representative single QD. Fig. 2.4 displays 500 seconds from the QD for which the intensity, $\tau$, and x and y positions were calculated and plotted for every 100 ms of data. The intensity had a mean of 105 kcounts/sec (Fig. 2.a) and rapidly fluctuated between a high level at ~140 kcnts/sec and a continuum of lower levels. Fluctuations of this nature were exhibited in all the QDs that we examined, and they are likely caused by temporarily trapped charges on the QD that alter the radiative decay (either by offering an alternative non-radiative relaxation pathway, or by temporarily preventing the QD from emitting)[5]. The blinking events were accompanied by changes in the fluorescence lifetime. We observed that the lifetime of the QD (Fig. 2.4b) decreased significantly when the QD intensity decreased, which would be expected if this is due to opening an additional non-radiative decay pathway. This behavior is seen clearly in the data recorded between 325 and 360 seconds (Fig. 2.4a and b); the

[5] See Section 4.3 for more discussion on the behavior of single QDs.

average lifetime was 43 ns before it switched to lifetimes as short as 20 ns at the same time the intensity decreased. There were also segments, including a brief one near 375 sec, where the intensity decreased and the lifetime increased. This behavior is an artifact of the detector dark counts which were registered randomly between zero and the 200 ns period of the pulsed excitation. When the QD switched completely off for the majority of the 100 ms bin, the average of the arrival times approaches the 100 ns lifetime of the dark counts.

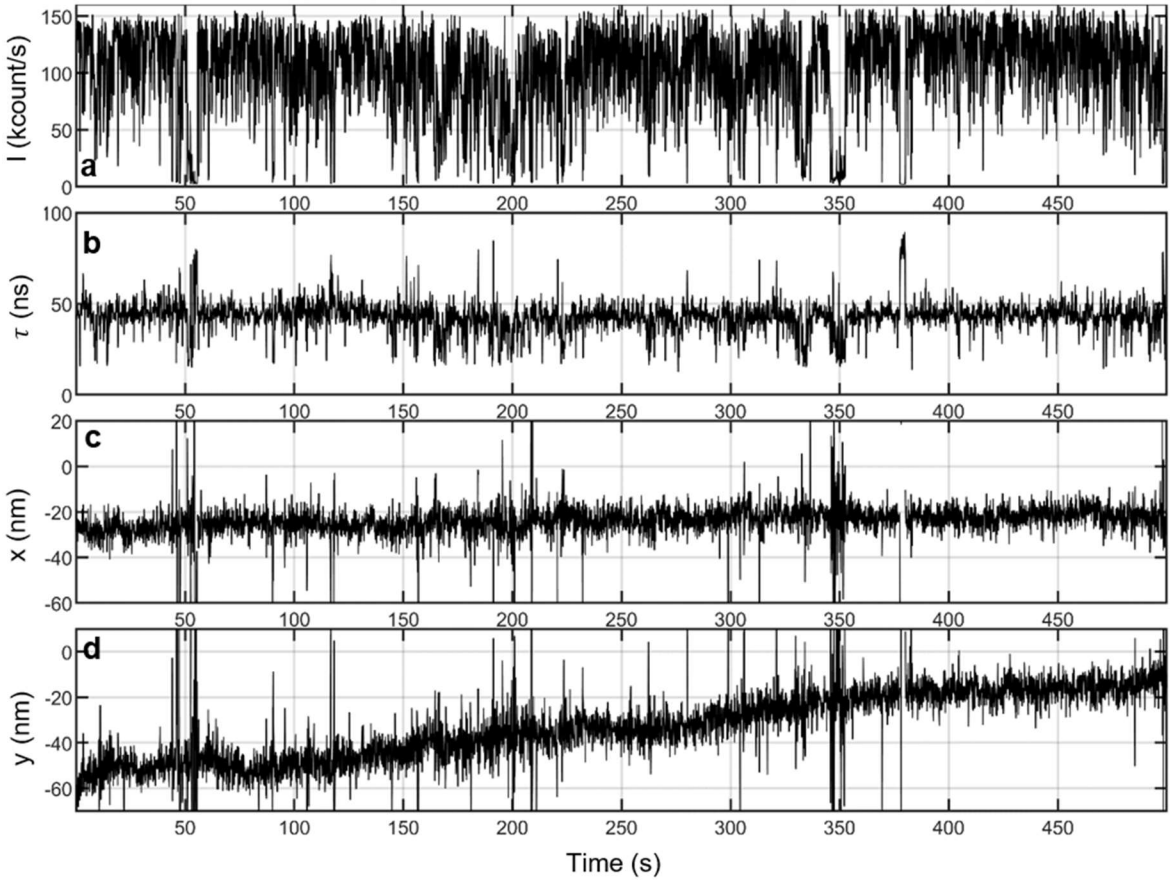


**Figure 2.4 Time-resolved microscope data from a representative isolated QD.** (a) The intensity *I* was determined every 100 ms and plotted in kcounts/s. (b) The lifetime $\tau$ in ns. (c) The x location of the centroid in nm versus time. (d) The y location of the centroid in nm versus time.

The x and y positions of the emission centroid were determined for each 100 ms time window (Fig. 2.4c and d) using maximum likelihood estimation (MLE), where a likelihood distribution for the centroid location given the counts detected in the four pixels was maximized. Chapter 3

describes this procedure. For the duration of this experiment (Fig. 2.4), the x position was static whereas there was substantial drift in the positive y direction. We corrected for the drift in each sample by selecting a short enough section of data so that the drift velocity appeared to be constant, and then we subtracted linear fits from the x and y positions versus time[6]. For this particular QD, we selected the segment between 275 and 475 seconds for linear fitting and further analysis. After drift correction, we computed the localization precision from the standard deviations of the x and y positions. In this case, the localization precision was found to be 4 nm in x and 5 nm in y for all the locations determined when the counts were greater than 100 kcounts/sec (i.e. locations determined with greater than 10,000 total counts). When the intensity is lower, the positions cannot be determined as precisely, and the distributions of the positions broadens. This precision is comparable, if not slightly better, than the single molecule localization precisions typically reported (these are usually between 1 and 100 nm) using other SR microscopes[55,68–76].

Figure 2.5 displays two projections of the drift-corrected x and y positions of the representative single QD recorded between 275 and 475 seconds; these are called the "SR images". Each point corresponds to a single centroid position found with 100 ms of data. The positions are the same in both plots, but one projection is color-scaled according to intensity (Fig. 2.5a), and the other is color-scaled according to lifetime (Fig. 2.5b). The centroid positions are scattered about a single mean, and one can see how the localization precision relates to the intensity: the yellow-colored centroids in the intensity-scaled plot that correspond to higher counts are more tightly

[6] Correcting for the drift with frequency-based filtration techniques is problematic, especially when studying quantum dot clusters which exhibit step changes in the position followed by long segments of time in a static location. The removal of low frequencies tends to attenuate these features of interest, and smear what would otherwise be a crisp SR image.

distributed about the mean whereas the purple-colored centroids (there are few of these because the QD rarely dropped below 50 kcounts/sec) are more widely distributed.

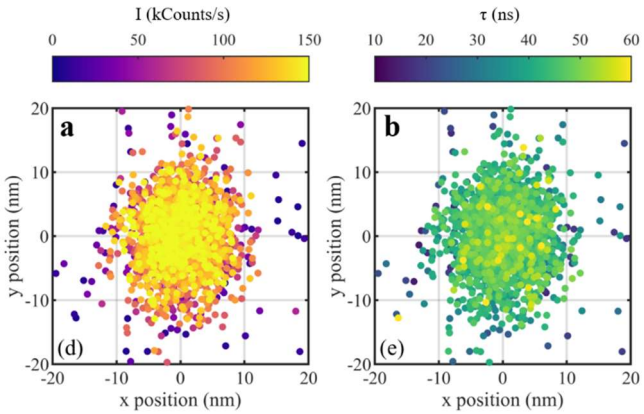


**Figure 2.5 Time-resolved super-resolution images of a single QD.** The centroid position is found every 100 ms for 200 s of data. The positions are drift-corrected and plotted with the color scale indicating intensity I in kcounts/s (a) and lifetime τ in ns (b). These are two-dimensional projections of the positions versus time that are plotted in Fig. 2.4c and d between 275 and 475 sec (after correcting for drift).

The selection of the bin time can significantly alter the information that you glean from a dataset (and your interpretation of it). If $\Delta t$ is too long, you risk averaging over important features in the data; if $\Delta t$ is too short, you lose precision and different features in the data can become smeared together into one broad distribution. Our selection of 100 ms airs on the side of being too long, and we tend to average over some important features in the lifetime and intensity. However, this bin time allows for localization precision on the spatial scale of the QDs, which is important for capturing position dynamics in the QD aggregates that we will examine in the next section. With a shorter bin time, we would be unable to detect significant changes in the position on the necessary spatial scale.

The behavior of the single QD that we have highlighted was representative of other QDs studied on glass, and Fig. 2.6 summarizes the intensity and lifetime behaviors of other single QDs. Fig. 2.6a displays normalized histograms of the intensities measured every 100 ms for 11 different

single QDs; the distributions of the binned intensities varied, and the mean intensity of each QD was between 100 and 200 kcounts/second. Fig. 2.6b displays normalized histograms of the lifetimes, also measured every 100 ms for the same 11 QDs; the mean lifetime of each QD was between 40 and 50 ns. Blinking events were infrequent and the lifetime was rarely (<1%) below 20 ns. Sample 1 in Fig. 2.6a and b corresponds to the representative single QD from Fig. 2.4 and 2.5. The heterogeneity in intensity and lifetime behavior may be caused by several different things. Firstly, the size distribution of $\pm$ 1.0 nm that QDs exhibited in both their core diameter and their overall diameter will alter the absorption cross section of the QDs, allowing some to absorb (and emit) more photons than others. It will also result in a distribution of band gaps among the different QDs[77,78]. Additionally, defects on the surface and within the crystal lattice of the QD can facilitate more charge trapping, and that will give rise to blinking that will decrease the emission intensity and lifetime.

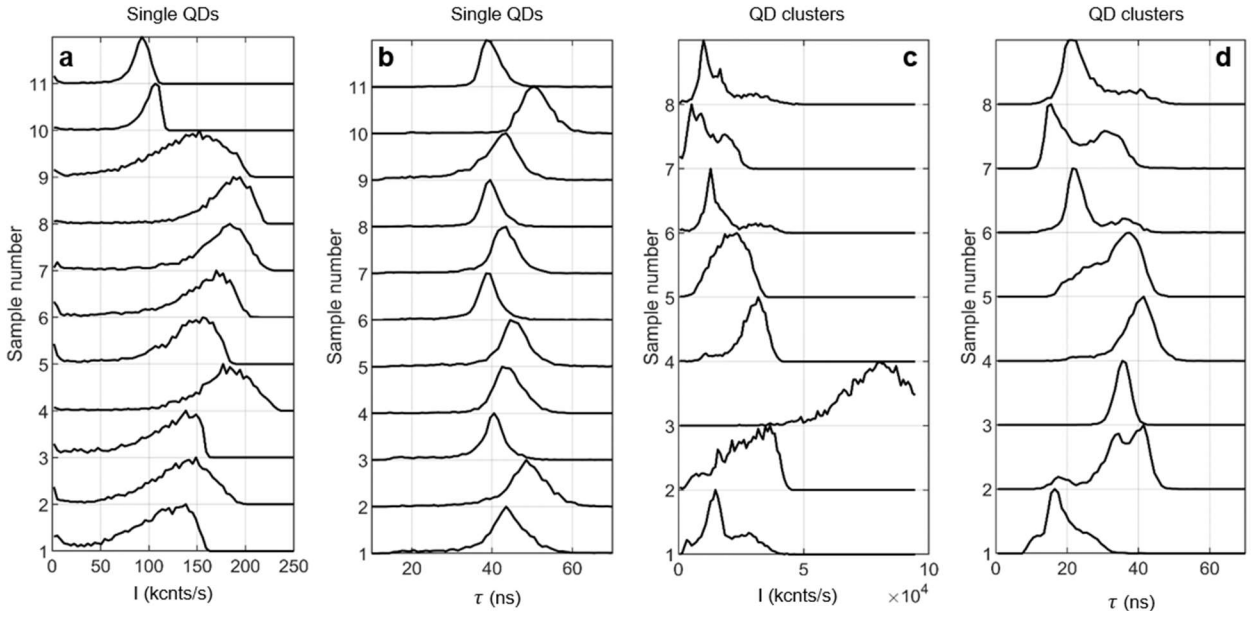


**Figure 2.6 Summary of intensity and lifetime behaviors for single QDs and QD clusters.** (a) and (b) Histograms of the total detected counts in kcnts/sec and lifetime in ns, respectively, recorded every 100 ms for 11 different single QD samples. Each sample was monitored for 500-1000 s. The peak of each distribution (of course) corresponds to the value of the intensity or the lifetime that appeared most frequently in the data. Sample number 1 in (a) and (b) is the representative QD discussed earlier. (c) and (d) Histograms of the total detected counts in kcnts/sec

and lifetime in ns, respectively, recorded every 100 ms for 8 different clusters of QDs. Each sample was monitored for 500-1000 s. Sample number 1 in (c) and (d) is the representative cluster of QDs that we discuss in Section 2.3.

The key takeaways from this section are: (1) single QDs have lifetimes of ~40-50 ns when in the on state, (2) blinking QDs exhibit shorter lifetimes that are typically 30-40 ns and rarely (<1%) less than 20 ns; (3) we can locate single emitters with ~5 nm precision with 10,000 detected counts using the time-resolved setup; and (4) single QD images show that the emission centroids are distributed about a single location.

## 2.3: Interpreting time-resolved images of clusters of QDs

To create small clusters, methanol was added to the diluted QDs (2 parts methanol to 100 parts toluene) five minutes prior to spin coating. The increased polarity of the solution may haven driven the nonpolar ligands of multiple QDs together so QD clusters were formed[79]. We could not identify the number of QDs within each cluster using our technique, but we examined the photon pair correlations, discussed in Section 2.4, to confirm that we were examining clusters rather than singles.

Unlike the centroid positions of single QDs that were distributed about a single mean, clusters often exhibited step-like behavior in the intensity and centroid position. This behavior is caused by QDs in the cluster turning on and off, so the centroid position shifts among the locations of the QDs that are emitting. When multiple QDs are in the on state, the centroid sits partway between them. In some cases, we observed that the lifetime also exhibited step changes synchronous to the position and intensity, and Fig. 2.7 displays 200 seconds of data collected from a representative cluster of QDs for which we observed that. We can identify synchronized changes in the intensity, lifetime, and x position versus time (Fig 2.7a-c, respectively), and the system appeared to switch between two discrete states. (We do not plot the y position for simplicity.) One

state had an intensity of ~300 kcounts/sec, a lifetime of ~25 ns, and centroid positions centered about x = -9 nm. Relative to the first state, the second one had a lower intensity of ~150 kcounts/sec, a shorter lifetime of ~15 ns, and centroid positions centered about x = 2 nm. A threshold of 200 kHz was chosen by inspection to separate high and low intensity segments, and we computed the average of the positions associated with intensities above and below that threshold for the entire 200 seconds of data. The distance between the two locations was found to be 12.3±0.3 nm. Repeating this procedure using a lifetime 21 ns as a threshold gave a separation of 12.2 ±0.3 nm between the two emission sites. The intensity and lifetime-scaled SR images of the representative cluster are displayed in Fig. 2.7d and e. These are projections of the x position (Fig. 2.7c) and y position for the same 200 sec of data. We clearly observe the same two states with distinct lifetimes, intensities, and positions.

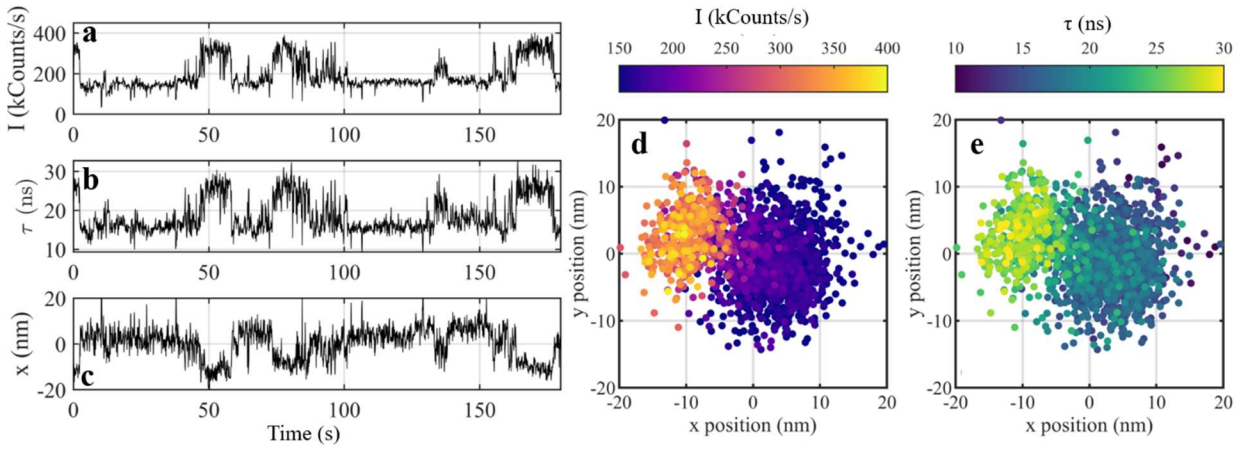


**Figure 2.7 Time-resolved data from a QD cluster.** For 200 seconds of data, the intensity *I*, fluorescence lifetime τ, x location, and y location are determined every 100 ms. (a) Plots *I* in kcounts/s. (b) Plots τ in ns. (c) Plots the x location in nm. A projection of the x and y positions gives the SR images shown in (d) and (e) which are color-scaled according to *I* and τ, respectively.

Figure 2.8 displays a selected six-second segment of the same cluster during which appears to have stepped between the two different states evidenced by Fig. 2.7d and e. In the first two

seconds of the segment, the intensity (a), lifetime (b), and x position (c), were constant. After two seconds, all three observables shifted to new values. They remained at their new values for two more seconds before recovering their initial values. The two states are spatially resolved in the SR images (Fig. 2.8d and e) compiled with six seconds of data. One then wonders why the two states appear merged once the entire 200 sec of data is incorporated in the SR image. One possible explanation is that there are other states that the system can occupy, but it does so less frequently, and we see the SR image gradually blurs as the system has enough time to occupy them.

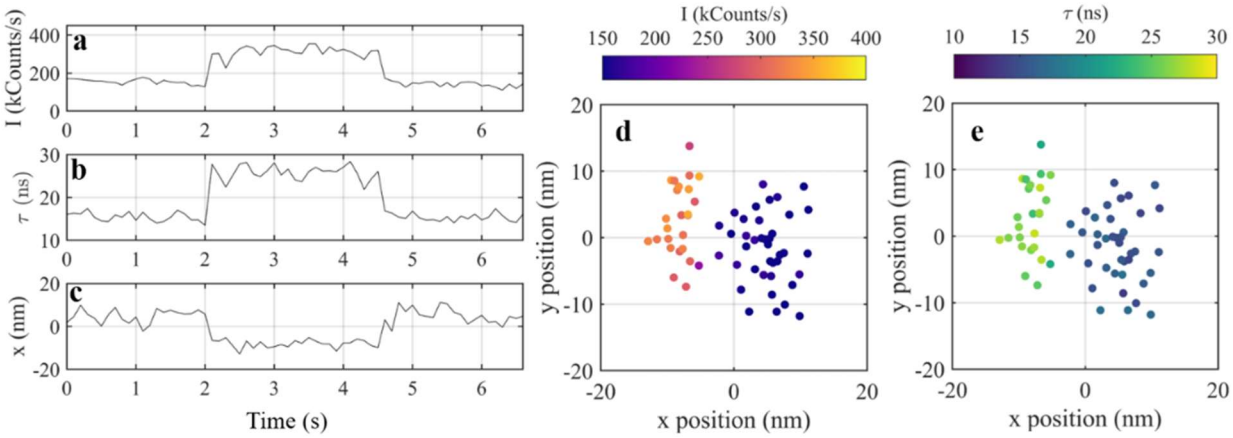


**Figure 2.8 Time-resolved data from a QD cluster, truncated.** This is a 6-second snapshot of the data from Fig. 2.7, taken from the time between -2 seconds and 4 seconds, and binned every 100 ms. (a) Intensity *I* (kHz) versus time. (b) Fluorescence lifetime τ in ns. (c) x location of the centroid in nm versus time. Superpositions of the x and y centroid locations for the six seconds give the super-resolution images in (d) and (e) that are color-scaled according to *I* and τ.

We would like to uncover the structure of the QD cluster and possible interactions among the QDs that give rise to the behavior we observe in Figs. 2.7 and 2.8. The simplest model we can consider for explaining the cluster's behavior during the six seconds displayed in Fig. 2.8 is that of two QDs. The simultaneous ~2× intensity increase and position shift at ~t = 2 sec would indeed occur if one QD was is the on state, and another QD exhibiting similar intensity switched from the off state to the on state. Continuing to assume this simple model, we can use the average locations of the two spatially resolved regions in Fig. 2.8d and e, which are at (3, -2) nm and (-8, 4) nm, to

identify the locations of both (QDs. The one that remains on during the entire six seconds is located at (3, -2) nm. Assuming the two QDs have equal intensities, the region at (-8,4) nm is halfway between the two QDs, so the second QD is located at (-19, 10) nm, and the center-to-center distance of the QDs is ~25 nm.

The simple model breaks down when we examine the lifetime behavior of the system. The ~15 ns lifetime of the region centered about (3, -2) nm is significantly shorter than the lifetimes of any QDs that we observed (see the lifetime distributions of singles in Fig. 2.6b). To explain the short lifetime, we hypothesize that energy transfer was occurring within the system. This is known to give rise to emission with a truncated lifetime from the donor particle, as transfer competes with the radiative decay of the donor. This is easily shown with kinetic models, which we formulate later in Section 4.2 for the purpose of quantifying the energy transfer rate in confirmed pairs of QDs. As we learned in the introduction, for energy transfer to take place efficiently, the QDs must be separated by ~6 nm, so the energy transfer rate would approach zero for two QDs separated by 25 nm. This suggests the model must be more complicated.

Along with the truncated lifetime of the donor particle, we expect to observe a decrease in the intensity of the donor emission as the energy transfer rate increases. Assuming the emission region centered about (3, -2) nm is donating energy, as its lifetime suggests, we might expect to see evidence of decreased emission. This is not the case; the intensity of the "donor" region is ~150 kcnts/sec, which is notably similar to intensities observed in single QDs (Fig. 2.6a). A possible explanation for this is that the donor region of the cluster may have been comprised of at least two QDs.

Many other clusters also exhibited signatures of energy transfer based on the presence of significantly shorter lifetime emission. Fig. 2.6c and d display histograms of the intensity and

lifetime of eight different QD clusters. Sample #1 is the representative QD cluster that we have been discussing. From the histograms, we observe that the shortest lifetimes of the single QDs in Fig 2.6b are still significantly longer than the lifetimes exhibited by some of the clusters shown in Fig. 2.6d[7]. SR images of the clusters showed that some behaved like the representative one, exhibiting multiple regions with correlated position, lifetime, and intensity changes which allowed us to hypothesize about direction of energy transfer through the cluster (Fig. 2.9). This may have been facilitated by the ~10% distribution of core sizes and particle sizes found within the synthesis batch that resulted in a distribution of band gaps among individual QDs[77,78]. The distribution of band gaps among individual QDs may have allowed them to take on preferred roles as either energy donors or acceptors within the clusters.

[7] There are also some interesting features in the lifetimes of the clusters where they exhibit bi-modal or even tri-modal distributions, which is in contrast to the single QDs which all have uni-modal distributions. This may be caused by a combination of heterogeneity among the lifetimes of the different QDs within the clusters, as well as the effects of energy transfer.

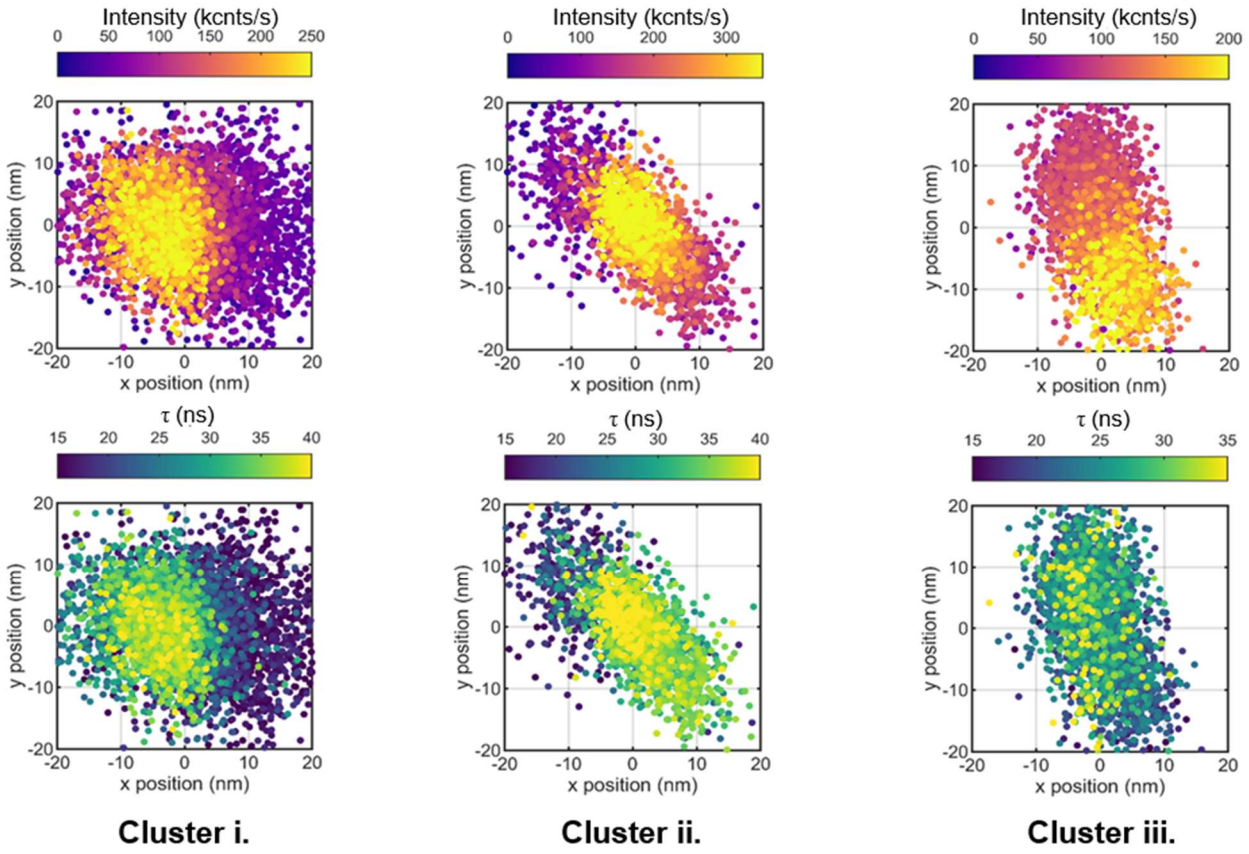


**Figure 2.9 Super-resolution images of QD clusters.** Three different QD clusters are displayed in the three panels. Images in the top row are color-scaled according to intensity *I* in kcounts/s, and images in the bottom row are color-scaled according to lifetime τ in ns. Cluster i. appears to be two QDs with centers spaced 9 nm apart. The truncated lifetime on the right that is signnificantly shorter than the lifetimes of isolated QDs suggests energy transfer in the system from right to left. Cluster ii. appears to have at least 3 spatially distinct regions of emisison. The high intensity in the center of the image may be a result of energy transfer toward the center, and the truncated lifetime of the region in the upper left supports this hypothesis. Cluster iii. does not exhibit emission with a truncated lifetime compared to single QDs, suggesting energy transfer may not be present. The high intensity associated with the region surrounding y = -10 nm suggests that the emission from multiple QDs is contributing to the centroids located in that region.

Returning to the representative cluster (Figs. 2.7 and 2.8), it appears that the significantly shorter lifetime and lower intensity of the centroids located near the origin occurs because QD(s) on that side of the cluster were transferring energy to the QD(s) on the left side. We speculate that the highest intensity and longest lifetime emission comes from the largest QD with the lowest energy band gap, and when that QD blinks off, we observe emission from the QD with the next

lowest band gap. In that case, the centroid position may shift between the locations of the two lowest-energy QDs within the cluster. It is notable that the longest lifetime contribution from many of the QD clusters (Fig. 2.6d) is shorter than typical lifetimes of individual QDs (Fig. 2.6b), including the representative cluster. This could possibly be caused by stripping of the ligand during the clustering process which alters the radiative decay pathways compared to the single QDs that are not exposed to the non-solvent. We did not explore this feature further.

In summary, we have described a SR lifetime imaging technique capable of assessing dynamic processes within small QD clusters, such as the presence and direction of energy transfer based on lifetime and intensity mapping.

## 2.4: Unabbreviated time-resolved SR microscope setup

Pulses with a ~100 picosecond full-width at half max (FWHM) were delivered at a repetition rate of 5 MHz from a 485 nm diode laser (PicoQuant LDH-P-C485 with a PDL-800-B driver). The repetition rate was approximately three times slower than the typical relaxation rates (1/60 ns = 17 MHz) of QDs, which ensured they had a high probability of relaxing before the arrival of the next pulse. If the system does not relax before the arrival of the next laser pulse, something called "wrap-around" occurs in which photons with lifetimes longer than the pulse period will appear to be caused by excitation from a subsequent laser pulse. This can alter early parts of the arrival time distribution and prevent one from accurately computing fluorescence decay parameters[8]. Directly after the laser head, two mirrors steered the light into a 20× air objective which then coupled the light into a single mode optical fiber that removed higher modes from the laser beam. Upon exiting

[8] An exception can be made for the case in which the decay is mono-exponential, for which it can be shown that wrap-around (aka "pile-up") will have no impact on the fluorescence decay histograms, and one can still accurately measure the decay rate.

the fiber, the light was collected and re-columnated by a 10× air objective. To remove possible IR contributions in the excitation, the light was filtered with 485 nm notch filter. Next, two mirrors steered the light into the back port of an inverted microscope (Olympus IX-71) and a dichroic mirror (D101 488, Semrock) reflected it into an infinity corrected 1.3 numerical aperture (NA) oil objective with a 100× magnification (Olympus). To achieve a tightly focused probe region, the light must be correctly steered into the center of the back of the objective. To ensure this, we focus light onto the surface of a glass coverslip and collect an image of the scattered excitation when the top surface of the coverslip is in focus (which is when the scattered excitation has the highest intensity). When the beam is misaligned, this image will appear elliptical, and it will change in both orientation and location as the z position of the objective is adjusted above and below the focus. When the beam is aligned, this image will appear more symmetrical, and it will only expand and contract about one location as we adjust the z position of the objective relative to the coverslip[9].

The ~630 nm emission from QDs deposited on the surface of a substrate (usually a glass coverslip) was collected by the same objective, transmitted through the same long-pass dichroic filter, and directed out of the microscope by a full mirror. (Immediately upon exiting the microscope, the light passed through a 800 nm short pass (SP) dichroic filter and a 800 nm SP filter (Edmund optics). These are part of the focal lock system we will describe later.) Before focusing the columnated emission with a 450 mm tube lens (resulting in an overall 250× magnification), the light was filtered with a 488 nm long pass filter (Semrock) to remove contributions from the scattered excitation. At the focus of the tube lens, the emission was collected

[9] To collect this image, we put a pellicle beamsplitter behind the back port of the objective. Most (98%) of the excitation passes through it on the way to the coverslip. Some scattered excitation is reflected by the dichroic beamsplitter back to the pellicle, and a small fraction of that scatter is then focused onto a camera (Thorlabs).

by a bundle of four square optical fibers (03208-REVA, CeramOptec). Each fiber aperture ("pixel") had a 100 μm width (area 100 × 100 $\mu m^2$) and the four were arranged in a 2 × 2 array with 15 μm of cladding separating each aperture. Each fiber was connected via an FC fiber coupler to a single photon counting avalanche photodiode detector (SPCM AQ 4C, Perkin Elmer).

The APD detectors released a transistor-transistor logic (TTL) pulse each time a photon was detected that was inverted and attenuated to -200 mV before passing to a counting module (Hydraharp 400, Picoquant). A nuclear instrument modules (NIM) pulse, referred to as the "sync pulse", was also passed to the Hydraharp from the laser driver synchronous to each time it released an excitation pulse. By recording the arrivals of these pulses, the Hydraharp allowed us to employ a method called time-correlated single photon counting (TCSPC), in which the arrival time of each photon relative to the start of the experiment ("macro-time") and the arrival time of each photon relative to the most recent laser pulse ("micro-time") were recorded. We used the macro-time to monitor the number of detected counts per unit time; the Hydraharp measured the macro-time by counting the sync pulses. We used the micro-time to monitor the fluorescence decay and determine photon pair correlations, which will be discussed later in the thesis; the Hydraharp measured the micro-time with a time-to-digital converter (TDC) by measuring the time delay between the sync pulse arrival and the TTL pulse arrival. After recording a micro-time, the TDC had a dead time of ~80 ns during which time it could not record another micro-time. Each detector had its own TDC, so the relative time between different photon detections occurring within 80 ns of one another could be measured, provided the photons were registered by different detectors. Symphotime 64

software (Picoquant v 2.4) compiled the digital output from the Hydraharp into binary files with a .ptu tag, and we read[10] and analyzed the .ptu files with Matlab.

The short duration of the excitation pulses ensured we could precisely record their arrival time, which was necessary so that we could then precisely record the arrival time of photons relative to when the system was excited (the micro-times). The variation in the arrival times of the sync pulses and other pulses in the electronics contributed to the overall instrument response function (IRF), though the main contribution to the IRF came from the APD detectors. The convolution of the IRF with the true decay gives the measured decay, so it was important to measure the IRFs for each detector if we wanted to recover parameters from the true decay that are on the same or shorter timescales as the IRF. We don't show any results from extracting these shorter time components in this thesis, but we include some documentation of how to do this here for future reference. To measure the IRF, we removed the LP 488 filter and acquired photons from scattered laser excitation off the surface of a glass coverslip[11]. Fig. 2.10a shows the IRFs for the four channels. We found that the data in each detector fit reasonably well to a bi-exponential decay convoluted with a fit to IRF for that respective detector. While many IRFs reported in literature for setups employing APD detectors are well-fit by a Gaussian, that was not so in our case. We found a reasonable fit (shown in Fig. 2.10b) to our IRFs required a five-parameter function with the form,

[10] The Matlab code for reading raw .ptu files was adapted from the Picoquant demo code and written by Omri Bar-Elli and Ron Tenne and is currently available here: https://www.mathworks.com/matlabcentral/fileexchange/61789-read_ptu_v1-filepath

[11] Ideally, one measures the IRF at the wavelength of their emission of interest. To do this, we would measure the decay from a fluorophore with a well-characterized decay that emits near 630 nm, and then back out the IRF from the data, which is the convolution of the known fluorophore decay with the IRF.

$$IRF(t) = \left[1 + \tanh\left(A(t - t_0)\right)\right]\left[Be^{C(t-t_0)}\right] + D, \quad (2.1)$$

which accommodated their fast rise and exponentially decaying tail. The *D* parameter accounted for the dark count contribution. We suspect that a Gaussian was not representative of the IRFs in our system because the light from the optical fibers was not directed onto the most responsive regions of the APD detectors when we used the FC couplers.

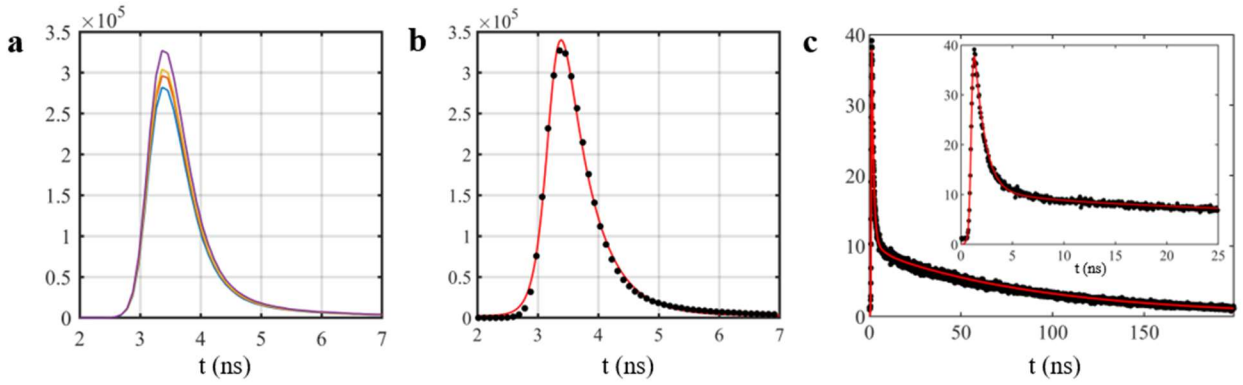


**Figure 2.10 Instrument response functions and fitting the fluorescence decays.** (a) Measured instrument response functions (IRFs) for the four channels. (b) A fit (red) using Eqn. 2.1 to the IRF in one channel (black points) for which *A* was 4.5e5, *B* was 2.6e5, *C* was 2.1, *D* was 2,000, and $t_0$ was 3.25 ns. (c) The fluorescence decay in one channel (black points) and its fit (red line) to the convolution of a bi-exponential decay and the fitted IRF. The inset shows the early part of the decay.

Apart from the $t_0$ parameter, which was responsible for shifting each channel forward or backward in time, the IRFs were not significantly different among the detectors. We measured the IRF each time we turned the detectors on because their $t_0$ values changed by ± 0.1 ns from day-to-day. We fit the decays to the four channels separately to accommodate the different IRFs in each channel[12]. To fit them, we used the convolution of a bi-exponential with Eqn. 2.1. Fig. 2.10c shows a fit to the data recorded from a cluster of QDs which had a 66% contribution of a 100 ns

[12] We should not forget the ± 0.1 ns variations of $t_0$. While small compared to the lifetimes of the emitters we study, these "temporal misalignments" may have unanticipated consequences for the time-resolved localization analysis that we present in Chapters 5 and 6.

lifetime, and a 34% contribution of a 0.7 ns lifetime. The temporal precision is limited by our ability to confidently fit the convolution of the IRF with the decay.

We placed the optical fiber bundle at the focus of the tube lens, which we identified using fluorescence correlation spectroscopy (FCS) of Rh110 in water. The correlation function provided by FCS allowed us to extract the brightness per molecule and width of the probe region, which were, respectively, maximized and minimized when the optical fibers were placed at the focus of the tube lens. For collecting FCS, we swapped the oil objective for a water objective, which had a longer working distance. This allowed us to collect light from deeper within the solution, avoiding the effects of fluorophore-surface interactions on the correlation function. We also adjusted the lateral position of the optical fiber bundle with a translation stage so that only one of the four detectors was receiving signal before collecting FCS data.

In addition to collecting the IRF at the start of the experiment, we also had to measure the relative collection efficiencies of the four detectors and align the fiber bundle in x and y. To measure the collection efficiencies (which were all within 10% of one another), we illuminated the fibers with uniform white light from an overhead lamp, and then took the ratio of the average counts in each detector to the average counts in detector 1, each measured over a 20 second period. This was done with all the emission filters mentioned above (488 LP and 800 SP) in place. To align the x and y position of the optical fiber bundle, we placed an aqueous solution of QDs (Invitrogen) on the surface of a coverslip and adjusted the objective focus ~5 nm above the surface of the coverslip. The x and y positions of the bundle were then adjusted the fiber bundle location with the translator stage until the average counts in each detector (now corrected for by taking the product of the relative efficiency of that detector with its true average) were approximately equal.

This ensured that when the QD was in the center of the probe region, the emission of the QD was in the center of the four fibers.

Each time a new sample was examined, the optimal z position of the objective relative to the sample surface was identified and maintained. For this, we placed a QD in the center of the probe region and adjusted the objective height to maximize the counts received by the detectors. It was necessary to maintain this focus so the size of the PSF, was also maintained. For this, another piezo stage (Mad City Labs Nano F Series) holding the microscope objective received feedback from a piezo driver (Nano-Drive, Mad City Labs). Input for the driver was obtained by monitoring the image of 850 nm light reflected from the surface of the sample using a CRISP autofocus unit and ASI piezo Z. An 800 nm dichroic SP (Edmund Optics) directed the infrared light from the source to the coverslip, and it directed the reflected light back to the autofocus unit for imaging[13]. Each time we acquired a new focus, it was necessary to measure the size of the PSF. The procedure for this is detailed in Section 3.3.

To complicate matters, the entire fiber bundle could be rotated so that the y axis was not orthogonal to the plane of the ground. This is akin to taking a picture while you hold a camera diagonally instead of portrait or landscape. This rotation, if significantly large, must be accounted for when measuring the PSF and correlating images collected on this microscope with images of

[13] For record keeping purposes, we note the z position maintained with a different system prior to June of 2020. The objective height was still adjusted by the same piezo holder (Mad City Labs Nano F Series), and feedback was provided by monitoring IR light reflected off the surface of the sample coverslip. For this image, a 785 nm laser beam (LDM 785, Thorlabs) was directed through the side port of the microscope and into the objective by a notch dichroic (NF D01 785, Semrock) and the reflected IR light was collected on a camera (DCC 1645C HQ, Thorlabs). The image moved as a function of z due to astigmatism introduced by purposely misaligning the IR beam. From that position, proportional and integral feedback were computed by a LabVIEW program, and the output, via a breakout box (NI-PCIe-6321 I/O, NI SCB 68A, National Instruments), was sent to the piezo driver (Nano-Drive, Mad City Labs).

the same sample collected on other microscopes. We have adjusted the fibers so this angle is <3 degrees (see Section 3.3), and we do not account for it when correlating images of samples examined with multiple microscopes.

To distinguish singles from clusters, we analyzed the photon pair correlation, $g^2(t)$, for each dataset. $g^2(t)$ is a histogram made up of the number of coincident photon arrivals between pairs of detectors for a given lag time between the arrival of photons in each detector. Fig. 2.11a and b show such photon pair correlations, $g^2(t)$, for the representative single QD and cluster of QDs described in Sections 2.2 and 2.3, respectively. The y axis displays the number of photon pair coincidences, $g^2(t)$, and the x axis displays the lag time. We note that unlike a traditional Hanbury Brown and Twiss scheme that has two independent single photon counting channels, we have a total of four channels. This enables us to measure six distinct pair correlations, and here we report their sum. Peaks are visible at nonzero integer multiples of the laser pulse period ($T$ = 200 ns). The ratio of the peak at zero lag time to the average of the peaks at other lag times, $g^2(0)/ g^2(T)$, is indicative of the presence of an isolated emitter or multiple emitters, as there is a low probability of collect a pair of photons from a single QD after a single laser pulse has arrived. We found $g^2(0)/ g^2(T)$ was greater than 0.5 for all clustered samples (in which non-solvent was added) and it was less than 0.3 for all single QD samples prepared. It was computed by dividing the area of the $T$=0 peak (from -100 ns to 100 ns) to the average of the area of the side peaks centered at -600, -400, 400, and 600 ns.

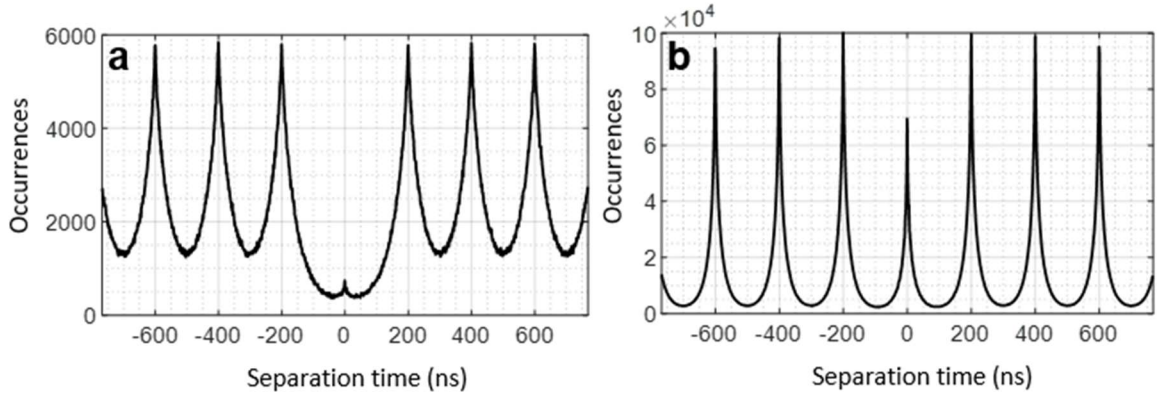


**Figure 2.11 The second-order correlation function, $g^2(t)$.** (a) $g^2(t)$ plotted for the representative QD single and (b) representative QD cluster that were described in Sections 2.2 and 2.3, respectively. Each correlation function is accumulated from 500 seconds of data. $g^2(0)/\ g^2(T) = 0.2$ for the single and $g^2(0)/\ g^2(T) = 0.7$ for the cluster.

# CHAPTER 3. Locating a single emitter with four pixels

Despite the minimal information contained in a four-pixel image, we can use it to locate the centroid of the emission profile created by a sample in our microscope to within several nanometers. If the emission profile is created by a single emitter, such as a single quantum dot (QD), the centroid of the point spread function (PSF) corresponds to the location of that emitter. If the emission profile is created by *multiple* emitters spaced closer than the diffraction limit, it is not possible to locate each of the emitters by locating the centroid in a single image. For those systems, which includes the small QD clusters that we have studied, the centroid will be located at a weighted average of all the emitters' locations. To circumvent this issue, researchers purposely examine emitters that go through states of high and low emissivity ("blinking")[14], and they locate the emission centroid in many consecutive images. This so-called super-resolution image shows the centroid location dancing among and between the true locations of the different emitters as they blink on and off, and this is the premise behind super-resolution microscopy[15]. The true locations of the individual emitters can be extracted from the SR image by filtering out data for which the intensity is high, this way it becomes more likely that only a single emitter is contributing to the emission profile at any one time.

[14] Blinking of an organic fluorophore occurs when the emitter temporarily enters a "triplet state". In contrast, blinking of a QD occurs when a charge is trapped on the nanoparticle, which opens nonradiative relaxation pathways that compete with (and outcompete when the QD blinks off) the radiative pathways.

[15] Another method for SR microscopy called stimulated emission depletion microcopy (STED) does not rely on the stochastic blinking of emitters, but instead uses a doughnut shaped laser beam to stimulate emission from all but the few (or ideally one) remaining emitters located at the center of the doughnut. The emission from these emitters arrives much later than the stimulated emission, and they are known to be located at the center of the stimulated emission beam.

To locate the emission centroid in our images, we use a method called maximum likelihood estimation (MLE), which involves maximizing a likelihood distribution for the location of an emitter given the counts recorded in a set of pixels in a designated time interval (usually between 10-100 ms). This location corresponds to the most likely emitter location given the counts recorded in the four pixels. The MLE approach is generally cited as the best method for single molecule localization[45]. In the first section of this chapter, we derive an expression for the likelihood distribution for the location of an emitter. In Section 3.2, we show how the likelihood distribution can be maximized to locate an emitter from the data recorded with our time-resolved SR microscope, and we discuss the localization precision that is achievable.

One reason that we get away with using only 4 pixels to precisely locate the emitter is because we provide the likelihood distribution with the size and shape of the PSF. Without that information, we would not be able to converge on a single most-likely location. Section 3.3 describes why this is the case and how we measure the PSF in an experiment. Other parameters that impact the localization precision are discussed in Section 3.2, including the magnification, the number of pixels, and the distance of the emitter from the origin.

## 3.1: A likelihood distribution $\mathcal{L}_{CW}$ for the location of an emitter undergoing continuous excitation

Most groups that apply MLE in the super-resolution community use a standard form of the likelihood distribution to describe their data. Surprisingly, we could not locate a reference that provided more than paltry details on how to formulate it[71]. To remedy this, we provide a

comprehensive derivation of the standard form in this section[16]. We will see one critical assumption—that the emitter undergoes continuous wave (CW) excitation – must be made to arrive at the standard likelihood distribution, so we ultimately refer to it as $\mathcal{L}_{CW}$. Readers may notice this is one of several likelihood distributions for the location of a single emitter that are derived in this dissertation; the other distributions are derived in Chapter 6 and account for the pulsed excitation that our setup uses. Aside from being correct, there are other advantages to using those distributions and we take advantage of them in Chapters 6 and 7. However, for cases of locating a single emission centroid in our experiments, we have found that $\mathcal{L}_{CW}$ achieves the same accuracy and localization precision.

In general, a likelihood distribution is constructed as follows: one writes down an expression for the probability of an event occurring given some inputs about the system, and then the expression is used in reverse, so the probability distribution of an event given the inputs becomes the likelihood distribution of the inputs given the event[80]. In our case, the event is that a certain number of photons are collected in each pixel after the emitter has been illuminated for a period of time. The probability of our event depends of inputs such as the location of the emitter.

[16] Some of the text in this chapter copied directly from two of our papers[51,93]. For reference 93, Megan Dunlap collected and analyzed the data, and wrote the manuscript. Duncan Ryan provided technical assistance with the optical alignment and provided feedback during the development of the localization algorithm. Peter Goodwin assisted with data interpretation, photon counting electronics, and optics. James Werner provided the equipment for the time-resolved super-resolution microscope and assistance with the single photon counting electronics. Jennifer Hollingsworth and Somak Majumder provided the QD samples. Martin Gelfand assisted with the development of the localization algorithm and data interpretation. Alan Van Orden assisted with developing of the microscope and localization algorithm. A.V.O., M.G., P.G., M.D., and D. R. edited the manuscript.

We begin by considering a simplified scenario in which a total of *N* photons strike a total area *A*, and a sub-area $A_1$ receives a portion of those photons. Assuming the photons are distributed uniformly, it follows that the probability of photons striking the sub-area is $p = \frac{A_1}{\mathrm{A}}$, and the probability that photons strike outside the sub-area is $q = 1 - \frac{A_1}{\mathrm{A}}$ . The probabilities of different possible outcomes are the terms of the binomial expansion, $(q+p)^N = \sum_{i=0}^{N} \binom{N}{i} q^{N-i} p^i$; a single term, $p(m_1; N) = \frac{N!}{m_1!(N-m_1)!}\left(1 - \frac{A_1}{A}\right)^{N-m_1}\left(\frac{A_1}{A}\right)^{m_1}$, in the summation represents the probability $p(m_1; N)$ that $m_1$ photons strike $A_1$, given that *N* photons strike *A*. For the case of several sub-areas receiving some of the *N* total photons, the probability of $m_1$ photons striking $A_1$, $m_2$ photons striking $A_2$, and so on, can be written as a term in a multinomial expansion:

$$p(m_1, m_2, \ldots; N) = \frac{N!}{m_1! m_2! \ldots (N - m_1 - m_2 - \cdots)!}\left(\frac{A_1}{A}\right)^{m_1}\left(\frac{A_2}{A}\right)^{m_2} \ldots \left(1 - \frac{A_1 + A_2 + \cdots}{A}\right)^{N - m_1 - m_2 - \cdots}. \quad (3.1)$$

The semicolon is used to indicate this is the conditional probability for $m_1, m_2, \ldots$ *given N* photons.

It is often assumed an emitter under continuous illumination in a time window $\Delta t$ has a Poisson distribution of *N*. Let us recall the conditions that give rise to the Poisson distribution before we use it in our likelihood analysis. For radiative decay from a single pathway the emission follows an exponential distribution with a characteristic emission lifetime of $\tau$, so the normalized distribution of emission times is $\psi(t) = \frac{1}{\tau} \cdot \mathrm{e}^{-t/\tau}$ . Integrating this gives the probability $p_{emit} = \int_0^{\Delta t} d\,t' \cdot \psi(t') = 1 - \mathrm{e}^{-\frac{\Delta t}{\tau}}$ that the fluorophore will emit between time zero and $\Delta t$. (It follows that the probability of not emitting is $1 - p_{emit} = \mathrm{e}^{-\frac{\Delta t}{\tau}}$.) The probability $p(1, \Delta t; \tau)$ that the

emitter gives off one, and only one photon during a time interval $\Delta t$, is the probability that emission takes place at a time $t'$ between zero and $\Delta t$, multiplied by the probability that no photons are emitted in the remainder of the interval between $t'$ and $\Delta t$.

$$p(1,\Delta t;\tau) = \int_0^{\Delta t} d\,t' \cdot \psi(t') \cdot \left[1 - \int_0^{\Delta t - t'} d\,t'' \cdot \psi(t'')\right] \rightarrow p(1;\,\Delta t,\tau) = \frac{\Delta t}{\tau} \cdot \mathrm{e}^{-\Delta t/\tau} \tag{3.2}$$

By writing the probability that no photons are emitted between $t'$ and $\Delta t$ as $1 - p_{emit}$ we are tacitly assuming that the emitter is immediately re-excited after emitting a photon at $t'$. Following the same reasoning, the probability of getting two photons, and only two photons, from a single emitter during $\Delta t$ is the product of the probability to emit the first photon at a time $t'$ between 0 and $\Delta t$, and the probability to emit the second photon at a time t'' between $t'$and $\Delta t$, integrated over all values of $t'$ and $t''$,

$$p(2,\Delta t,\tau) = \int_0^{\Delta t} d\,t' \cdot \psi(t') \cdot \int_0^{\Delta t - t'} d\,t'' \cdot \psi(t'') \left[1 - \int_0^{\Delta t - t' - t''} d\,t''' \cdot \psi(t''')\right] \tag{3.3}$$

$$= \frac{1}{2}\left(\frac{\Delta t}{\tau}\right)^2 \mathrm{e}^{-\Delta t/\tau}$$

Continuing this exercise for 3, 4, .... photons, we can deduce the probability to emit *N* photons in a time $\Delta t$ is

$$p(N;\Delta t,\tau) = \frac{1}{N!}\left(\frac{\Delta t}{\tau}\right)^N \mathrm{e}^{-\Delta t/\tau}. \tag{3.4}$$

The Poissonian expressed by Eq. 3.4 is valid for an emitter undergoing continuous wave (CW) excitation with the caveat that the emitter is immediately re-excited after each emission. Perhaps

that is common knowledge for researchers in our field, but we found no discussion of this, at least in the SR microscopy literature.

Multiplying Eq. 3.1 and Eq. 3.4 and summing over all N gives the probability to find counts $m_1, m_2, \ldots$ in the respective sub-areas during $\Delta t$,

$$p(m_1, m_2, \ldots; \Delta t, \tau) = \sum_{N=0}^{\infty} p(m_1, m_2, \ldots; N) p(N; \Delta t, \tau) \tag{3.5}$$

$$= \sum_{N=m_1+m_2+\cdots}^{\infty} \frac{N!}{m_1! m_2! \ldots (N-m_1-m_2-\cdots)!} \left(\frac{A_1}{A}\right)^{m_1} \left(\frac{A_2}{A}\right)^{m_2} \ldots \left(1 - \frac{A_1+A_2+\cdots}{A}\right)^{N-m_1-m_2-\cdots} \frac{1}{N!} \left(\frac{\Delta t}{\tau}\right)^{N} \mathrm{e}^{-\Delta t/\tau}.$$

The expression is simplified if we let $N' = N - m_1 - m_2 - \cdots$, and the sum in Eq. 3.5 is recognizable as the series expansion of an exponential,

$$p(m_1, m_2, \ldots; \Delta t, \tau) = \frac{\left(\frac{A_1 \Delta t}{A\ \tau}\right)^{m_1} \left(\frac{A_2 \Delta t}{A\ \tau}\right)^{m_2} \ldots}{m_1! m_2! \ldots} \mathrm{e}^{-\Delta t/\tau} \sum_{N'=0}^{\infty} \frac{1}{N'!} \left(1 - \frac{A_1+A_2+\cdots}{A}\right)^{N'} \left(\frac{\Delta t}{\tau}\right)^{N'}, \tag{3.6}$$

from which it follows that the probability to receive counts $m_1, m_2, \ldots$ in the sub-areas $A_1, A_2,$ during $\Delta t$ given an emission lifetime $\tau$ is equal to

$$p(m_1, m_2, \ldots; \Delta t, \tau) = \frac{\left(\frac{A_1 \Delta t}{A\ \tau}\right)^{m_1} \left(\frac{A_2 \Delta t}{A\ \tau}\right)^{m_2} \ldots}{m_1! m_2!} \mathrm{e}^{-\Delta t/\tau} \mathrm{e}^{\left(\frac{\Delta t}{\tau}\right)\left(1 - \frac{A_1+A_2+\cdots}{A}\right)} = \prod_k \frac{\left(\frac{A_k \Delta t}{A\ \tau}\right)^{m_k}}{m_k!} e^{\frac{A_k \Delta t}{A\ \tau}}. \tag{3.7}$$

Eq. 3.7 is a product of Poisson distributions for each subarea $A_k$. We note that the ratio $\frac{\Delta t}{\tau}$ is the average number of total photons $\bar{N}$ that strike the area A, and the product $\frac{A_k}{A}\frac{\Delta t}{\tau} = \frac{A_k}{A}\bar{N}$ is the average number of photons that strike the sub-area $A_k$. In summary, the Poissonian in Eq. 3.4 turns the multinomal probability distribution in Eq. 3.1 into the Poissonian probability distribution displayed in Eq. 3.7.

We should not that people will often approximate a multinomial as a Poissonian for entirely different reasons than ours. One way is by assuming that the average number of photons, $\mathrm{N}(\mathrm{A}_1 + \mathrm{A}_2 + \mathrm{A}_3 +)/\mathrm{A}$, is much less than the total possible number of photons, *N*. That gives a Poissonian distribution, which is defined as the limit of the multinomial as both N and A go to infinity while the two sums, $\mathrm{A}_1 + \mathrm{A}_2 + \mathrm{A}_3 + \cdots$ and $\mathrm{m}_1 + \mathrm{m}_2 + \mathrm{m}_3 + \cdots$, remain finite[81]. In our case, we cannot apply this approximation because A represents our PSF, which does not go to infinity. Another way to arrive at the Poissonian is by arguing that $(\mathrm{A}_1 + \mathrm{A}_2 + \mathrm{A}_3 + \cdots)/\mathrm{A} \ll 1$. Once again, that is not the case for our detection scheme, where the pixels are collecting a large fraction (~60%) of the total photons emitted.

The background counts $b_\mathrm{k}$ in each pixel can be incorporated into the expression in a remarkably simple manner. The background is characterized during the experiment by exciting a portion of the coverslip with no emitters. It is made up of dark counts from the APD detectors, scattered excitation light that is transmitted through the detection filters, and fluorescence of the glass coverslip to which the emitters are attached. All four pixel' backgrounds are well-described by a Poisson distribution $p_b^{(\mathrm{k})}(b_k;\beta_k) = \frac{\mathrm{e}^{-\beta_k}}{b_k!}(\beta_k)^{b_k}$ where $\beta_k$ is the average number of background counts in pixel $k$[82]. Fig. 3.1 shows histograms of the background counts we recorded for exciting a glass coverslip and Poissonian fits to each of them.

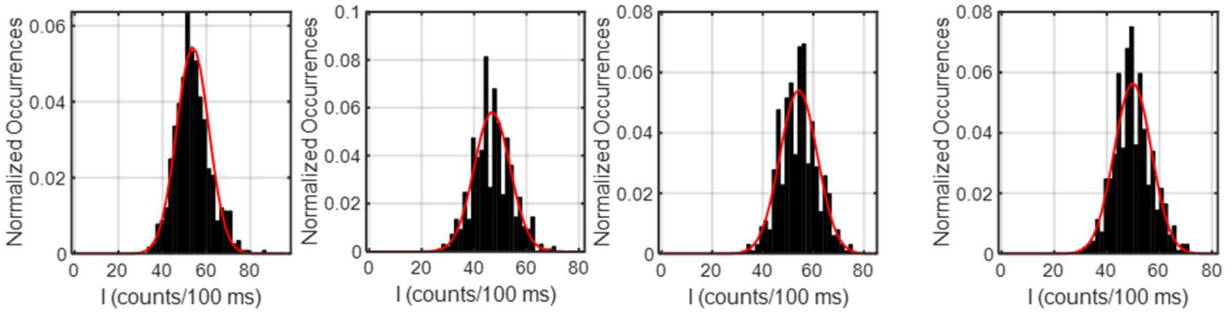

**Figure 3.1 Poissonian distribution background counts recorded in each detetor.** The normalized histograms of background counts for all four pixels are shown above with overlays of Poisson distributions with means $\beta_1 = 54$, $\beta_2 = 47$, $\beta_3 = 54$, and $\beta_4 = 50$ counts, per 100 ms, for each pixel. Detector dark counts, autofluorescence of the glass coverslip, and leaked excitation light through the spectral filters contribute to the background.

While $m_\mathrm{k}$ is the photon count acquired in each pixel, the actual count that is measured in an experiment $M_\mathrm{k} = m_\mathrm{k} + b_\mathrm{k}$ is made up of both detected photon arrivals and background counts. We can express the probability in terms of the measured counts in all four pixels $\{M_\mathrm{k}\}$ as the discrete convolution of Eq. 3.7 and $p_b^{(k)}(b_\mathrm{k})$,

$$P(\{M_\mathrm{k}\}; \bar{N}) = \sum\nolimits_{b_1, b_2, \ldots} p(M_1 - b_1, M_2 - b_2, \ldots; \bar{N}) \quad p_b^{(1)}(b_1)\, p_b^{(2)}(b_2) \ldots. \tag{3.8}$$

This can be simplified. Let us modify a portion of the expression involving only one pixel after putting in the explicit forms for

$$p(M_1 - b_1) = \frac{\left(\frac{A_1}{A}\bar{N}\right)^{M_1 - b_1}}{(M_1 - b_1)!} \text{ and } p_b^{(1)}(b_1) = \frac{\mathrm{e}^{-\beta_1}}{b_1!}(\beta_1)^{b_1}. \tag{3.9}$$

Multiplying and dividing by $M_1!$ leaves us with a summation that can be recognized, conveniently, as a multinomial expansion,

$$\frac{\mathrm{e}^{-\beta_1}}{M_1!} \sum_{b_1 = 0} \frac{M_1!}{(M_1 - b_1)! b_1!} \left(\frac{A_1}{A}\bar{N}\right)^{M_1 - b_1} (\beta_1)^{b_1} = \frac{\mathrm{e}^{-\beta_1}}{M_1!}\left(\frac{A_1}{A}\bar{N} + \beta_1\right)^{M_1}. \tag{3.10}$$

For multiple pixels, the contribution from each is modified by the background counts in the same way. The result is that the probability of the set of pixel counts $\{M_\mathrm{k}\}$ given a Poisson distribution of signal and a Poisson distribution of background is

$$P(\{M_{\mathrm{k}}\};\bar{N},\ \{\beta_k\}) = \left[\mathrm{e}^{-\bar{N}\left(\frac{A_1+A_2+\cdots}{A}\right)}\right]\cdot\left[\frac{\left(\frac{A_1}{A}\bar{N}+\beta_1\right)^{M_1}\mathrm{e}^{-\beta_1}}{M_1!}\cdot\frac{\left(\frac{A_2}{A}\bar{N}+\beta_2\right)^{M_2}\mathrm{e}^{-\beta_2}}{M_2!}\cdot\ldots\right]. \tag{3.11}$$

We note that this expression the same form as Eq. 3.7, except that each factor $\left(\frac{A_{\mathrm{k}}}{A}\bar{N}\right)^{M_{\mathrm{k}}}$ in Eq. 3.7 has been replaced by $\left(\frac{A_{\mathrm{k}}}{A}\bar{N}+\beta_{\mathrm{k}}\right)^{M_{\mathrm{k}}}$.

The location (X,Y) of the emitter is incorporated by expressing the area overlap $\frac{A_{\mathrm{k}}}{A}$ as the integral of the PSF over the cross-sectional area of the optical fiber aperture.

$$\frac{A_{\mathrm{k}}}{A} = \eta_k\int_{x_k-\frac{a}{2}}^{x_k+\frac{a}{2}}\int_{y_k-\frac{a}{2}}^{y_k+\frac{a}{2}}\mathrm{d}x\,\mathrm{d}y\,\frac{1}{2\pi w_x w_y}\mathrm{e}^{-(x-\mathrm{X})^2/2{w_x}^2}\mathrm{e}^{-(y-\mathrm{Y})^2/2{w_y}^2}. \tag{3.12}$$

Here we assume a Gaussian PSF characterized by widths $w_x$ and and $w_y$, and optical fibers with square apertures with side lengths $a$ located at $(x_k, y_k)$. The values of $\eta_{\mathrm{k}}$ account for the differences in efficiency among the four detectors, and they are determined for each pixel by illuminating the pixels with lamp light, collecting photon counts, and calculating the constants that would give uniform counts on each of the pixels. The integral can be factorized and simplified[17] to give $\frac{A_{\mathrm{k}}}{A} = \eta_k I_x I_y$, where

$$I_x = \frac{1}{2}\cdot\left[erf\left(\frac{\frac{a}{2}+x_k-\mathrm{X}}{\sqrt{2{w_x}^2}}\right)-\mathrm{erf}\left(\frac{-\frac{a}{2}+x_k-\mathrm{X}}{\sqrt{2{w_x}^2}}\right)\right], \tag{3.13}$$

and

[17] Substitute $u = (\mathrm{x}-\mathrm{X})/\sqrt{2{w_x}^2}$

$$I_y = \frac{1}{2} \cdot \left[ erf\left( \frac{\frac{a}{2} + y_k - \mathrm{Y}}{\sqrt{2{w_y}^2}} \right) - \mathrm{erf}\left( \frac{-\frac{a}{2} + y_k - \mathrm{Y}}{\sqrt{2{w_y}^2}} \right) \right]. \tag{3.14}$$

The number of expected counts in each pixel is then $\mu_{\mathrm{k}} = \frac{A_{\mathrm{k}}}{A} \overline{N}$. Having incorporated the emitter location and PSF width, the probability to get a set of counts $\{M_{\mathrm{k}}\}$ in each pixel is

$$\mathrm{P}(\{M_{\mathrm{k}}\}; \overline{N},\ \{\beta_k\}, w, X, Y) = [\mathrm{e}^{-\mu_1 + \mu_2 + \cdots}] \cdot \left[ \frac{(\mu_1 + \beta_1)^{M_1} \mathrm{e}^{-\beta_1}}{M_1!} \cdot \frac{(\mu_2 + \beta_2)^{M_2} \mathrm{e}^{-\beta_2}}{M_2!} \cdot \ldots \right]. \tag{3.15}$$

At this point, we reverse the independent and dependent variables, and identify the probability distribution for the counts $\{M_{\mathrm{k}}\}$ given the location $(\mathrm{X}, \mathrm{Y})$ and given the average counts $\overline{N}$ as the (unnormalized) likelihood disttribution $\mathcal{L}_{CW}(\mathrm{X}, \mathrm{Y}, \overline{N})$ for $\mathrm{X}, \mathrm{Y}$, and $\overline{N}$ for an emitter undergoing CW excitation[80],

$$\mathcal{L}_{CW}(X, Y, \overline{N}; \{M_{\mathrm{k}}\},\ \{\beta_k\}, w) = [\mathrm{e}^{-\mu_1 + \mu_2 + \cdots}] \cdot \left[ \frac{(\mu_1 + \beta_1)^{M_1} \mathrm{e}^{-\beta_1}}{M_1!} \cdot \frac{(\mu_2 + \beta_2)^{M_2} \mathrm{e}^{-\beta_2}}{M_2!} \cdot \ldots \right]. \tag{3.16}$$

Since we are only concerned with determining the position of the centroid, we integrate over all of $\overline{N}$ to get a reduced distribution. If we express $\overline{N}$ as the dimensionless variable $Z = \sum_k \mu_k$, and use $r_i = \frac{\mu_i}{\sum_k \mu_k}$ to denote the relative fraction of counts in each pixel, the reduced distribution can be expressed as an integral over *Z*,

$$\mathcal{L}_{CW}(X, Y; \{M_{\mathrm{k}}\}, \{\beta_k\}, w) = \int_0^\infty d\overline{N} \mathcal{L}_{CW}(X, Y, \overline{N}) = \int_0^\infty dZ\ e^{-Z} e^{\sum_{k=1}^{4} M_k \ln(r_k Z + \beta_k)}. \tag{3.17}$$

Because the integrand is strongly peaked when $\{M_{\mathrm{k}}\} \gg 1$, we can make the Gaussian approximation by expanding the argument of the exponential to second order in *X, Y,* and *Z*. In that case, the integral over *Z* gives the same result as replacing the integral with its the integrand evaluated at its peak $Z_{max(X,Y)}$ (apart from a normalization constant). When evaluating the $\mathcal{L}_{CW}$

for different values of $X$ and $Y$ we use this replacement procedure; we solve for the value of $Z(X,Y)$ that maximizes the expression by taking the derivative of the exponent

$$\frac{d}{dZ}\left(-Z+\sum_{k=1}^{4} M_k \ln(r_k Z+\beta_k)\right) = -1+\sum_k \frac{r_k M_k}{r_k Z_{max}+\beta_k} = 0, \tag{3.18}$$

and setting it to zero each time the likelihood is computed for a given $X$ and $Y$. The reduced likelihood distriubtion in its final form is

$$\mathcal{L}_{CW}\,(X,Y;\{M_{\mathrm{k}}\},\{\beta_k\},w) = e^{-Z_{max}} e^{M_1 \ln(Z_{max} r_1+\beta_1)} e^{M_2 \ln(Z_{max} r_2+\beta_2)}. \tag{3.19}$$

The position of the centroid for each set of $\{M_{\mathrm{k}}\}$ is located by numerically finding the values of $X_{max}$ and $Y_{max}$ that maximize $\mathcal{L}_{CW}$ (Fig. 3.2). For this we use the downhill simplex method[83], which involves climbing to the top of the surface and decreasing the step sizes as we approach the maximum[18].

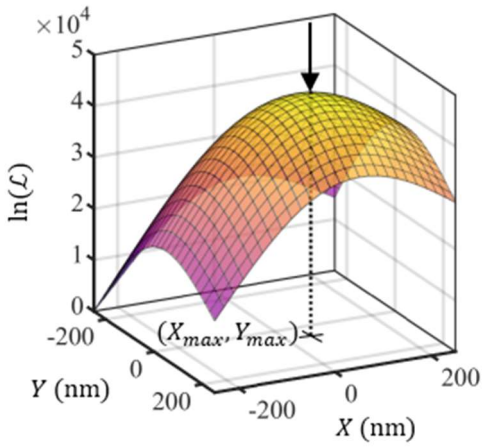


**Figure 3.2 Log-likelihood distribution for $X$ and $Y$.** We plot the log of the (unnormalized) likelihood distribution $\mathcal{L}_{CW}\,(X,Y;\{M_{\mathrm{k}}\},\{\beta_k\},w)$ for the centroid location, $(X,Y)$, given the total counts in each of the four pixels, $\{M_{\mathrm{k}}\}$, the background counts in each of the pixels, $\{\beta_k\}$, and the width $w$ of the PSF. This is maximized to find the values $X_{max}$ and $Y_{max}$ that correspond to the most

[18] After identifying $X_{max}$ and $Y_{max}$, the most likely value of $\bar{N}$ can be determined from $Z_{max}$, where $\bar{N} = Z_{max}\left(\sum_{k=1}^{4} c_k \frac{A_k(X_{max},Y_{max})}{A}\right)^{-1}$.

likely location of the centroid. The counts were generated from a Monte Carlo simulation of an emitter located at (50,50) nm. Parameters in the simulation mimicked the $w$, $\{\beta_k\}$, and total photons $\bar{N}$ that are found in experiments. The values $X_{max}$ and $Y_{max}$ that correspond to the maximum of $\mathcal{L}$ are determined by numerically locating the peak of the $\ln(\mathcal{L})$. The log distribution has a smaller gradient than $\mathcal{L}$, making it computationally tractable to compare values when the surface is strongly peaked.

## 3.2: Locating single emitters with $\mathcal{L}_{CW}$ and characterizing the localization precision

Now that we know the assumptions that go into $\mathcal{L}_{CW}$, we can use it to analyze data from single QDs that are sparsely dispersed on the surface of a glass coverslip. Data is typically collected for 60-600 sec, and then spit into many shorter time windows $\Delta t$. For each $\Delta t$, we bin the detected photons to get $\{M_{\mathrm{k}}\}$ and then compute the most likely centroid location ($X_{max}$, $Y_{max}$) . Fig. 3.3 shows the centroid location of a single QD measured from the counts acquired for $\Delta t$=100 ms over the course of a 100 s experiment. The origin is defined as the center of the optical fiber bundle, which is roughly (10 nm, 30 nm) relative to the location of the QD. Before acquiring data, we align the optical fiber bundle so that that its center corresponds to the center of the optical probe region where the excitation power is highest. In the figure, we do not correct for the slow <0.1 nm/s lateral drift of the sample in the positive direction that is visible in the trajectory of $Y_{max}$.

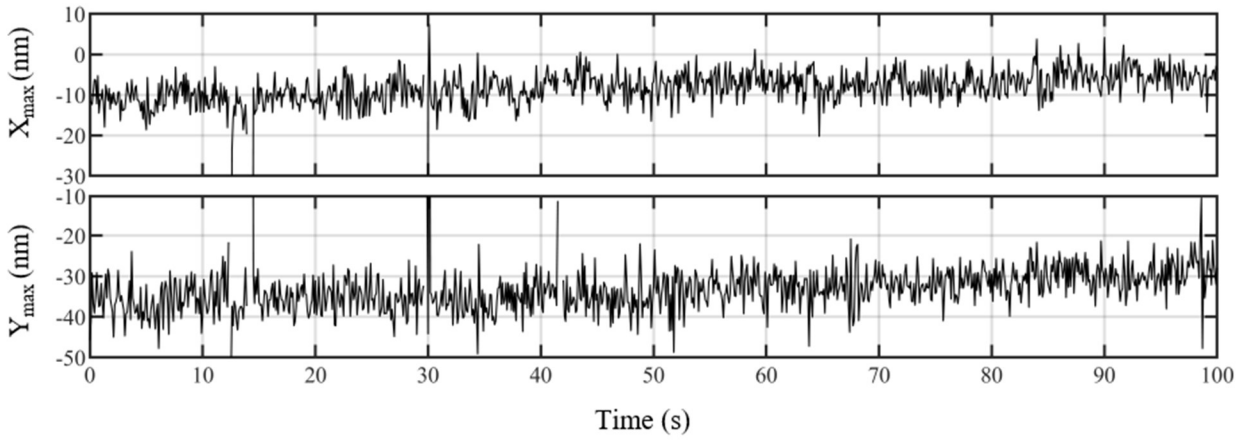


**Figure 3.3 Centroid location ($X_{max}$, $Y_{max}$) of a single QD monitored over time.** The location is computed every 100 ms for 100 s of data. The brief segments where no location is plotted, for instance near 14 s, are times during which the signal has fallen close to the level of background counts and no centroid location can be discerned. There is slow lateral drift of the sample which can be seen from the gradual movement <0.1 nm/s of both $X_{max}$ and $Y_{max}$ in their respective positive directions.

Assuming fluctuations in the position of a single QD monitored in an experiment are entirely due to shot noise, the localization precision $\sigma_X$ and $\sigma_Y$ in X and Y, respectively, can be accurately estimated by computing standard deviation of many measurements of $X_{max}$ and $Y_{max}$ over the course of time. However, mechanical drift of the sample in the $x$ and $y$ directions is inevitable in our experiment and serves to increase $\sigma_X$ and $\sigma_Y$, making the calculated localization uncertainty larger than reality. This can be partially corrected for by fitting the sequence of X and Y positions to straight lines, or by low frequency filtering, before calculating their distributions. Alternatively, $\sigma_X$ and $\sigma_Y$ can be determined for relatively short segments of time during which the drift is insignificant. Using the latter approach for the positions shown Fig. 3.3, we determined the standard deviations for ten segments of the data, each one lasting 10s of the data. We found a precision of ~4 nm for each segment. Most commonly, we select longer segments of data over which the drift is approximately linear (as a rule, that is almost always the case), and we compute the precision from the standard deviation of the locations after a linear fit to the x and y positions.

It is useful to explore how $\sigma_X$ and $\sigma_Y$ change as a function of different parameters such as $\bar{N}$, the number of pixels in the camera, and PSF size. We do this by analyzing Monte Carlo simulated data sets[84]. First, we explore the precision for different simulated datasets with four pixels where the PSF size and background levels mimic what we see in experiments[19], and the value of $\bar{N}$ is varied. For each dataset, we repeated the following "study" 1,000 times: first, we generated $N$ photons drawn from a Poisson distribution with an average $\bar{N}$. Each photon was given a coordinate drawn from a Gaussian PSF with a fixed width located at the center of four pixels. Next, we collected the photons in four pixels and we determined $X_{max}$ and $Y_{max}$ using the MLE procedure described in Section 3.2. We determined the localization uncertainty for a particular $\bar{N}$ from the standard deviation of the distribution of $X_{max}$ and $Y_{max}$. We repeated the study for different values of $\bar{N}$, and we observed that the localization precision scales as $1/\sqrt{\bar{N}}$, as expected from the central limit theorem. Fig. 3.4 illustrates this relationship; each marker corresponds to the precision $\sqrt{\sigma_X^2 + \sigma_Y^2}$ determined from a simulated dataset that used a particular $\bar{N}$. Within an experiment, the total photons collected from a single QD are $\bar{N}$~20,000-30,000, corresponding to a localization precision of 3-5 nm (Fig. 3.3)[20]. To compare our results from experiments with results from simulations, consider the QD for which the centroid locations are plotted in Fig. 3.3. The total counts $\sum_{k=1}^{4} M_k$ were ~17,000 counts/100 ms for $\bar{N}$~30,000 photons. A simulation that mimicked

[19]We select values for the parameters in the simulation that are equal to what we observe in experiments, so $w_x = w_y = 160$ nm and $\beta_1 = \beta_2 = \beta_3 = \beta_4 = 50$ counts/100 ms.

[20] The most probable value of $\bar{N}$ is centered around 30,000 photons/100 ms for the QD examined in Fig. 3.3. When the emitter is close to the origin, ~40% of $\bar{N}$ constitutes counts that strike the cladding that surround each fiber rather than the optical fiber aperture where the photons are detected, so the typical detected counts from a single QD is ~18,000 counts/100 ms under these excitation conditions

the counts, PSF width, and location of that QD yielded a slightly better localization precision of ~3 nm[21].

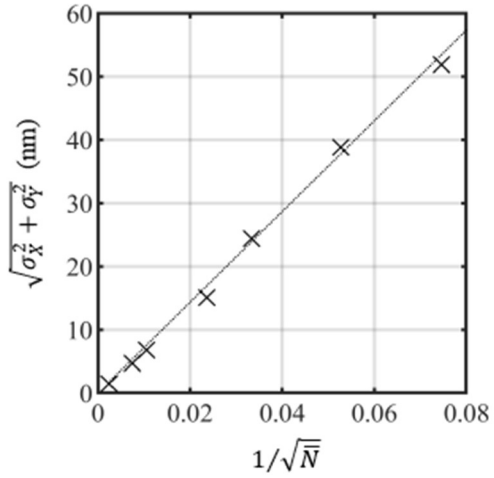


**Figure 3.4 Localization precision follows the central limit theorem.** The markers indicate the localization precision $\sqrt{\sigma_X^2 + \sigma_Y^2}$ determined from Monte Carlo simulated experiments of a single emitter repeatedly creating *N* photons drawn from a Poisson distribution with a different mean $\bar{N}$. Some of the *N* photons are "detected" and the emitter is located with MLE. The standard deviation in *X* and in *Y* of the repeated localizations, $\sigma_X$ and $\sigma_Y$, is determined. Each experiment used a different $\bar{N}$. The linear fit emphasizes that the relationship between $\bar{N}$ and the precision is what would be expected by the central limit theorem. For single QDs under the excitation conditions described in Chapter 2.4, $\bar{N}$ is ~20,000-30,000 photons/100 ms, allowing for a precision of ~3 nm per 100 ms time window.

The magnification of the microscope (which can stretch or shrink $w$) plays a role in $\sigma_X$ and $\sigma_Y$. One can imagine if the magnification is too small, then all the photons could land on a single pixel, or worse, all the photons could land on the cladding between the pixels. Both those scenarios would make it difficult to obtain much information about the emitter location. The precision deteriorates exponentially with small $w_{PSF}$ and it quickly becomes impossible to locate the emitter.

[21]The small discrepancy between the precision determined from simulated data and the precision determined from experimental data indicates that our simulation does not fully describe the experimental system. In other words, additional processes such as technical noise (vibrations) exist in the experiment that are unaccounted for when constructing the simulated data.

On the other hand, if the magnification is too large, the precision will not be optimized because the counts will not change as significantly as a function of the emitter location. (The relationship between precision and $w$ is not so sensitive for large $w$. For example, for a PSF size that is twice the optimal width, the precision only worsens by ~10%.) With our setup where each pixel is 100 um across and the cladding separates the pixels by 15 μm, the optimal width of the PSF is $w \approx 50$ μm, which we achieve with a 250× magnification. Figure 3.5a illustrates the likelihood distribution for X and Y for the simulated case of an emitter at the origin in which the magnification approaches the lower limit at which point it becomes impossible to locate the emitter. The effects of this are quite beautiful because the pixel geometry gets traced out by the likelihood distribution; the distribution is highest wherever there is cladding because the magnification is so low that there is a probability the emitter could be hiding between the pixels.

It is interesting to learn how $\sigma_X$ and $\sigma_Y$ fare when the camera has more pixels. We simulate a case in which we have 8 pixels arranged in a 3×3 square with one corner pixel missing. This may seem like an odd choice, but we had the option of using this arrangement in the lab rather than the 4-pixel detection scheme used throughout this thesis. Each pixel is again 100 μm across and 15 μm of fiber cladding separates each one. In terms of $\sigma_X$ and $\sigma_Y$, Fig. 3.6 shows that we have little to gain in precision by using more pixels. Comparing two simulated cases of an emitter at the origin, we can see there is <1 nm improvement. It is useful to note that the optimal precision for the for the 8-pixel case, which we are showing in Fig. 3.5, requires a ~2× higher magnification than the 4-pixel case. The 250× magnification that we use for the 4-pixel case will actually put us in the regime in which the PSF is too small for the 8-pixel case and then it is not possible to precisely locate the emitter. Fig. 3.5b shows how the likelihood distribution behaves under these

circumstances. There is a high probability for the emitter to be somewhere in the central 100 ×100 μm pixel, and low probability of it being anywhere else.

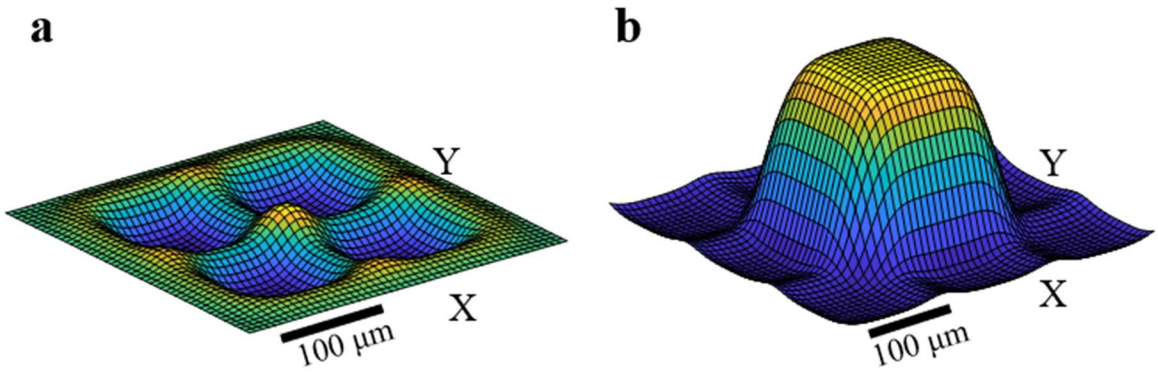


**Figure 3.5 Log-Likelihood distributions for the X and Y position of the emission centroid for small magnification (small PSF widths).** (a) A likelihood distribution generated from simulated data of an emitter located at the origin. The PSF widths of the simulated emitter are similar to the width of the optical cladding, so few counts are collected by the pixels. The likelihood distribution then "knows" the emitter is probably anywhere *except* above the pixels, and this is why there are indentations in the distribution where each of the pixels are located. (b) A likelihood distribution generated from simulated data of an emitter located at the origin where photons are collected by an 8-pixel camera. Because the PSF is far smaller than the width of the optical fibers, the distribution shows there is equal probability for the emitter to be anywhere within the area of the center pixel.

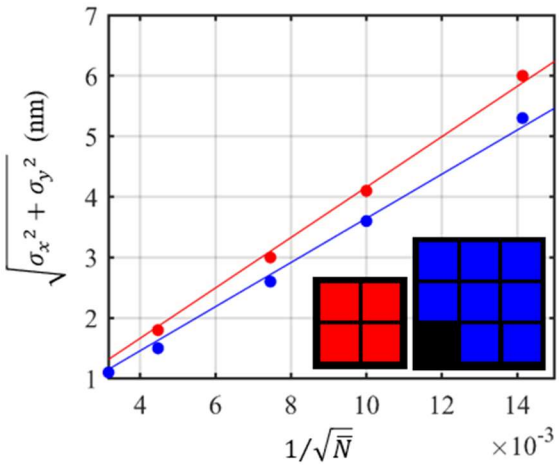


**Figure 3.6 Comparing the precision of four and eight-pixels detection schemes.** Simulation results are presented for both the four-pixel detection scheme (red) and eight-pixel detection scheme (blue). There is a nominal improvement in the precision with a larger number of pixels. A

total signal of 18 kcounts per 0.1 ms bin, typical for a single QD, affords ~3 nm of precision with both detection schemes.

The precision also suffers if the magnification is too high (the PSF width is too large), but there is a great benefit to operating in this regime if you need a larger field of view over which to monitor the emitter. In simulated cases that mimic our experimental signal, background, and ~50 μm PSF width in the image plane (which we get with 250x magnification), we run into issues when the emitter is farther than 350 nm from the origin. At these distances, two or three of the pixels receive few counts, but we rely on their sparse signals to locate the emitter. Out here, the localization precision is poor, and the average centroid location that we identify is significantly inaccurate- the peak of the likelihood distribution is skewed farther from the origin than the true location, and the inaccuracy is proportional to the distance from the origin[22]. This inaccuracy is eliminated if we use a higher magnification, and it is also eliminated if we use more pixels in our detection scheme.

However, we should not forget that we do not have uniform excitation of our coverslip. If an emitter has drifted or moved 300 nm from the origin, it is also ~300 nm from the center of the probe region and has little probability of excitation. In light of this, the limiting cases we just discussed where the peak of the distribution no longer accurately pinpoints the true location are a little irrelevant. Fig. 3.7 displays (a) $\bar{N}$, (b) x position, and (c) y position determined for a single QD that we monitored for ~ 20 minutes. A linear fit to the positions shows a drift velocity of (0.2, 0.1) nm/s, and we can see the $\bar{N}$ is significantly lower when the emitter is >100 nm from the origin.

[22] One wonders if this effect would be ameliorated by analyzing data that uses the true Bessel function rather than a Gaussian surrogate for the PSF.

This is not the result of an inability to accurately get $\bar{N}$ from the MLE, but is caused by the emitter drifting out of the center of the probe region where the excitation power is highest[23].

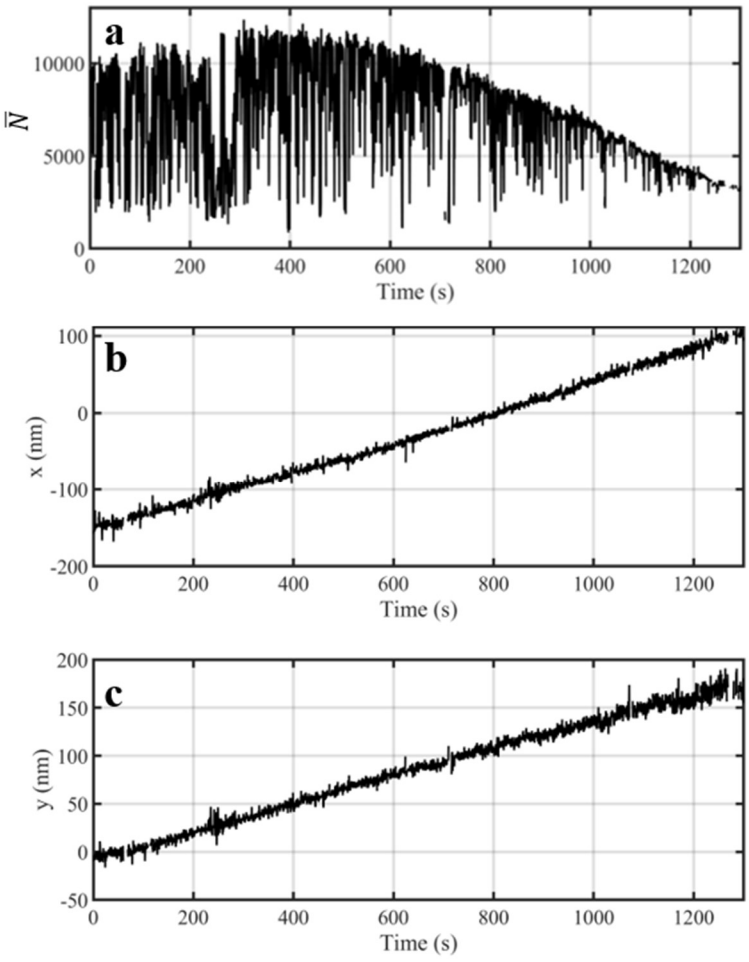


**Figure 3.7 Monitoring a single QD drifting out of the probe region**. (a) The $\bar{N}$ value, in counts per 0.5 s, rises slightly for the first 400 sec of data and then gradually falls. This is caused by drift of the QD in and out of the probe region. (b) The x location in nm is determined for every 0.5 s of

[23] If we assume that the level of emitted counts is directly related to the excitation power (for QDs under these excitation conditions, that is not necessarily true), we can use the drifting to estimate the size of the probe region. The maximum value of $\bar{N}$ is ~12,000, which occurs at t = ~400s for which the location is (25, 50) nm, and this is the location of the center of the probe region. The half max of the excitation profile would cause $\bar{N}$ to be ~6,000, and that occurs at t = ~1,050 s when the position is (50, 140) nm. The change in position corresponds to the half width at half max, which is 93 nm. For a Gaussian excitation profile, this corresponds to a width of ~80 μm. In comparison, sigma is ~74 nm for a diffraction limited spot with a wavelength of 485 nm!

data, and it has a velocity of 0.2 nm/s (c) The y location determined with every 0.5 s of data has a velocity of 0.1 nm/s)[24].

Aside from quantifying $\sigma_X$ and $\sigma_Y$ by examining the standard deviation of a collection of peak locations, we can also identify them by examining the curvature of the likelihood surface about its peak, which will dictate how well we can perform each localization. Fig. 3.8a shows two different likelihood distributions in yellow and purple which correspond two different sets of counts that we provided to the MLE. The yellow set of counts had a higher value of $\overline{N}$ and the purple set of counts had a lower value of $\overline{N}$. The curvature of the two distributions illustrates how there is greater uncertainty (larger curvature, worse precision) when the counts are lower. Fig. 3.8b shows how this plays out in the standard deviations of the centroid locations that are plotted for a single QD. One can see that the lower counts correspond to the purple-colored locations, and these have a larger standard deviation than the positions determined with higher counts that are colored yellow.

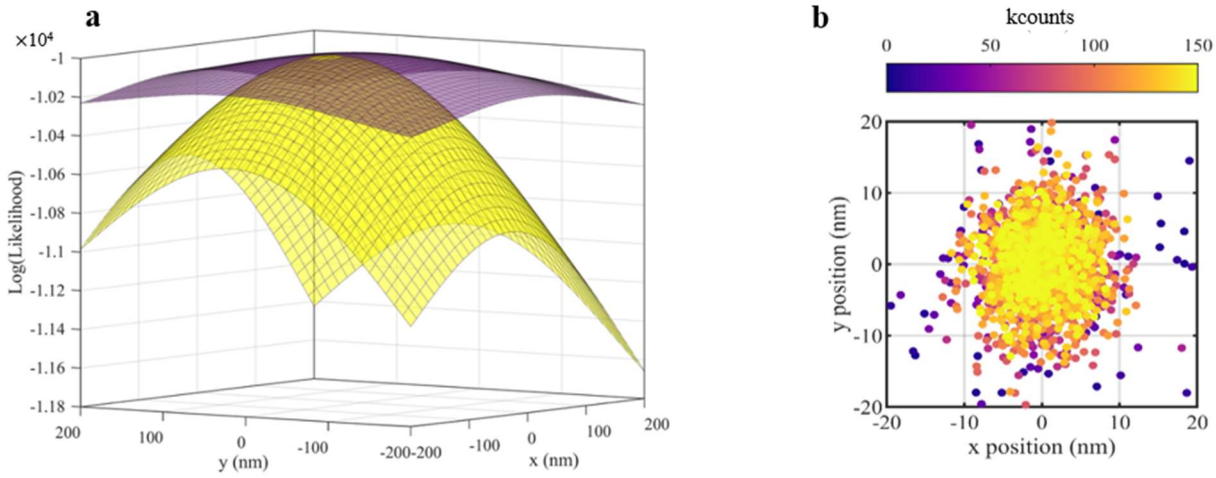


**Figure 3.8 Examining the curvature of the likelihood surfaces as a function of intensity.** (a) Log-likelihood distributions for locating an QD with high counts (yellow) and with low counts (purple) are shown. The width about the peak corresponds to the localization precision. When the

[24] The $\overline{N}$ values are lower for the data displayed in this figure compared to other singles shown in this section and that is because we examined this QD with a lower excitation power and on a different substrate (a SiN SEM window).

counts are lower, the width is higher, reflecting greater uncertainty in that localization. When the counts are higher, the width is narrower, reflecting less uncertainty in that localization. (b) This shows the centroid locations found for a single QD, color-scaled according to the number of detected counts. The lower counts are reflected in the locations that are colored purple, and we can see these have a wider distribution than the locations that are colored yellow for high counts.

The surfaces of the likelihood distributions are ellipsoidal[25], so we fit them with a multivariate Gaussian. We begin by making a series expansion about the peak of the likelihood distribution, $(X_{max}, Y_{max})$. Notice that the first derivative terms do not appear because they are equal to zero at the peak.

$$\mathcal{L}(\mathrm{X},\mathrm{Y}) = \mathrm{e}^{\ln \mathcal{L}(\mathrm{X},\mathrm{Y})} \sim \mathrm{e}^{\ln \mathcal{L}(X_{max},Y_{max}) + \frac{\partial^2}{\partial X^2} \ln (\mathcal{L}(X_{max},Y_{max})) \frac{(X-X_{max})^2}{2!}} \cdot \mathrm{e}^{\frac{\partial^2}{\partial Y^2} \ln (\mathcal{L}(X_{max},Y_{max})) \frac{(\mathrm{Y}-Y_{max})^2}{2!} + \frac{\partial^2}{\partial \mathrm{X}\,\partial \mathrm{Y}} \ln (\mathcal{L}(X_{max},Y_{max}))(\mathrm{X}-X_{max})(\mathrm{Y}-Y_{max})}. \tag{3.20}$$

Neglecting higher terms than the second derivative assumes that the likelihood distribution is so strongly peaked that those terms are insignificant. The exponent is concisely expressed in terms of the Hessian matrix, $[H]$, so

$$\mathcal{L}(X,\mathrm{Y}) = \mathcal{L}(X_{max}, Y_{max}) \cdot \mathrm{e}^{\frac{1}{2}(\Theta)^T [H] (\Theta)}, \tag{3.21}$$

where $[H] = \begin{bmatrix} \frac{\partial^2}{\partial X^2} \ln (\mathcal{L}(X_{max}, Y_{max})) & \frac{\partial^2}{\partial \mathrm{X}\,\partial \mathrm{Y}} \ln (\mathcal{L}(X_{max}, Y_{max})) \\ \frac{\partial^2}{\partial \mathrm{X}\,\partial \mathrm{Y}} \ln (\mathcal{L}(X_{max}, Y_{max})) & \frac{\partial^2}{\partial Y^2} \ln (\mathcal{L}(X_{max}, Y_{max})) \end{bmatrix}$

and $\Theta = \begin{pmatrix} \theta_1 \\ \theta_2 \end{pmatrix} = \begin{pmatrix} X - X_{max} \\ \mathrm{Y} - Y_{max} \end{pmatrix}$.

[25] Differences in the X and Y curvatures exist when $w_x \neq w_y$.

The second term in the likelihood expression is a decaying Gaussian in two dimensions; this is obvious if it is written in terms of the diagonal matrix of eigenvalues and the principal coordinates,

$$\frac{1}{2}(\Theta)^T[H](\Theta) \rightarrow \frac{1}{2}(\theta_p)^T \begin{bmatrix} \lambda_+ & 0 \\ 0 & \lambda_- \end{bmatrix} (\theta_{\mathrm{p}}) = \frac{1}{2}\lambda_+ {\theta_+}^2 + \frac{1}{2}\lambda_- {\theta_-}^2 \tag{3.22}$$

provided that the eigenvalues are negative. In Eq. 3.22, $\Theta_p = \begin{pmatrix} \theta_+ \\ \theta_- \end{pmatrix}$. The variances, $\sigma_+ = \sqrt{\frac{-1}{2\lambda_+}}$ and $\sigma_- = \sqrt{\frac{-1}{2\lambda_-}}$, are now expressed along the direction of the principal coordinates and the distribution at the peak is

$$\mathcal{L}(X_{max}, Y_{max}) \cdot \mathrm{e}^{-\frac{1}{2\sigma_+^2}{\theta_+}^2 - \frac{1}{2\sigma_-^2}{\theta_-}^2}. \tag{3.23}$$

## 3.3: Measuring the point spread function width

Up until this point, we have made little mention of the width of the PSF $w$, though it plays a crucial role in the centroid localization. As one would expect, the $w$ used in the MLE must agree with the true width of the PSF for the centroid to be accurately located. Some localization algorithms (cite thunderStorm) maximize the likelihood distribution over $X, Y$, and $w$, and they are able to identify a single maximum in the 3-dimensional distribution. However, we found that $w$ cannot be determined from MLE with the information provided by a four-pixel image. In other words, we cannot identify a single maximum of $\mathcal{L}(X, Y, w)$; there are an infinite number of combinations of $(X, Y)$ that are equally likely if $w$ is a free parameter.

To uncover this property, we ran Monte Carlo simulations in which we collected a set of counts $\{M_{\mathrm{k}}\}$ from background and an emitter located at (25, 25) nm with a Gaussian PSF. We then attempted to maximize $\mathcal{L}\,(X, Y, w; \{M_{\mathrm{k}}\})$, but found there was a flat ridgeline in the distribution

where a different value of $w$ would allow for a different but equally likely $(X, Y)$. Fig. 3.9 illustrates this flat ridgeline by showing cuts in $\mathcal{L}\,(X, Y, w)$ for different values of $w$. From left to right, it displays $\mathcal{L}(X, Y, w = 132\,nm)$, $\mathcal{L}(X, Y, w = 165\,nm)$, and $\mathcal{L}(X, Y, w = 198\,nm)$. When $w$ agrees with the true width of the simulated emission PSF, the maximum of the likelihood correctly locates the centroid, so the center surface has a peak located near (25, 25) nm. On the other hand, the surfaces on the right and left which we generated with a $w$ that does not agree with the width in the simulation, and they are peaked in the wrong location. This indicates that $w$ cannot be determined from the counts in four pixels when the location of the centroid is also unknown. Therefore, it is necessary to obtain $w$ in a separate measurement if the centroid is to be located for a four-pixel detection scheme[26]. It is interesting to note that the three distributions in Fig. 3.9 widen as a function of $w$, and we are able to visualize how the localization precision can change with different magnifications, as we discussed earlier.

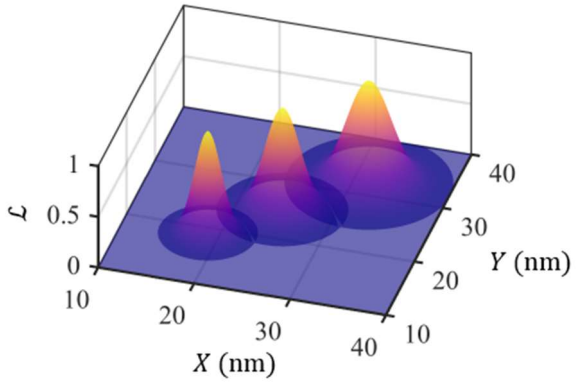


**Figure 3.9 Likelihood surfaces from a likelihood volume.** Three cuts in the (unormalized) likelihood distribution $\mathcal{L}\,(X, Y, w; \{M_k\})$ are displayed for different values of $w$. From left to right, the surfaces are $\mathcal{L}(X, Y, w = 132\,nm)$, $\mathcal{L}(X, Y, w = 165\,nm)$, and $\mathcal{L}(X, Y, w = 198\,nm)$. Color scaling indicates their heights, which are identical. The counts $\{M_k\}$ used as input for the surfaces are generated from a simulation of an emitter with a Gaussian PSF that has a width of 165 nm and is located at (25 nm, 25 nm). As expected, the location of the peak of $\mathcal{L}$ agrees with the actual

[26] One wonders if we could identify a single maximum in $\mathcal{L}\,(X, Y, w)$ if we had used the 8-pixel detection scheme that we discussed earlier. If that is the case, then the 8 pixel scheme has a significant advantage over the 4-pixel one.

location of the emitter when $w$ agrees with the true width of the PSF, which is the case for the surface in the center. We observe that the maxima of the likelihood distributions are identical for all three surfaces (and we find they are identical for any selection of $w$ if $X$, $Y$, and $\bar{N}$ are unknown).

We devised and implemented a simple method for determining the $w$ that required no additional microscope components or changes to the experimental setup. It relies on accurate movement of the piezoelectric stage in the $x$ and $y$ directions to measure $w_x$ and $w_y$, thereby accounting for ellipticity of the PSF. First, we follow the same procedure outlined above for locating and acquiring data from a single QD. After recording counts for a brief segment of time (~2-3 sec), $T$, we displace the stage (the QD) by $\overrightarrow{D_S} = D_S\,\hat{x} + 0\,\hat{y}$ and again record counts for $T$. We bin the registered counts over all of $T$ from each measurement to compile two sets of $\{M_\mathrm{k}\}$. From these we compute two locations with the MLE, using a dummy PSF size characterized by $w_x^{(guess)}$ and $w_y^{(guess)}$. We used these locations to define $\overrightarrow{D_{MLE}}$, the distance separating the two locations. $\overrightarrow{D_{MLE}}$ points the same direction as $\overrightarrow{D_S}$ [27], but the two vectors only agree in magnitude, as we have seen, if $w_x^{(guess)}$ and $w_y^{(guess)}$ are consistent with the true PSF widths.

The method by which we determine determine $w_x^{(guess)}$ and $w_y^{(guess)}$ that give agreement between the stage movement and the MLE-determined movement is illustrated in Fig. 3.10. The red surface in Fig. 3.10a is generated from two sets of $\{M_\mathrm{k}\}$ gathered in an experiment for which $D_S$ = 50 nm and $T$ = 3 sec. The selection of $w_x^{(guess)}$ and $w_y^{(guess)}$ determines $\left|\overrightarrow{D_{MLE}}\right|$. The blue plane at z = 50 nm illustrates $\left|\overrightarrow{D_S}\right|$. The intersection between the red surface and the blue plane gives a curve which shows the combinations of $w_x^{(guess)}$ and $w_y^{(guess)}$ for which $\overrightarrow{D_S} = \overrightarrow{D_{MLE}}$. One

[27] This is because the axes of the stage are parallel with the axes that define the detection plane, as shown in Fig. 3.11 and accomanying text.

can see that many combinations satisfy the condition. We return to the experiment, and this time we acquire counts before and after we move the QD by $\overrightarrow{D_S} = 0\hat{x} + D_S\,\hat{y}$. Again, we determine two locations from MLE and their separation depends on $w_x^{(guess)}$ and $w_y^{(guess)}$; that relationship is given by the black surface in Fig. 3.10a. The intersection between both red and black surfaces and the plane gives us a single point, $w_x = 150$ nm and $w_y = 160$ nm, which satisfies $\overrightarrow{D_S} = \overrightarrow{D_{MLE}}$.

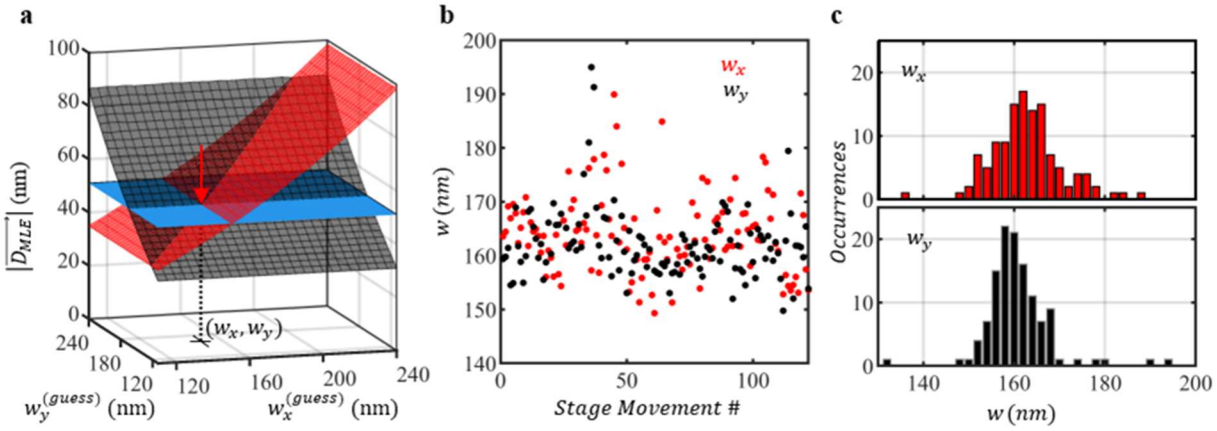


**Figure 3.10 Measuring the point spread function widths $w_x$ and $w_y$.** (a) The blue plane indicates the movement of the piezoelectric stage in either the x or y direction by 50 nm; the red and black surfaces show the distance that the emitter moved in $\hat{x}$ and in $\hat{y}$, respectively, which depends on the width parameters $w_x^{(guess)}$ and $w_y^{(guess)}$ used by in the MLE. The point of intersection between the three surfaces gives the widths $w_x$ and $w_y$ that allow for agreement between the calculated movement based on MLE, and the actual movement done with the stage. (b) Repeated movements of the stage and recordings of the pixel counts are done to acquire many measurements of $w_x$ and $w_y$. (c) Histogram of $w_x$ values for which $\overline{w}_x$ is 164±9 nm and of $w_y$ values for which $\overline{w}_y$ is 162±10 nm.

In practice, the stage movement and measurment of $w_x$ and $w_y$ are done many times (see Fig. 3.10b) for each coverslip that we examined. Their average values $\overline{w}_x$ and $\overline{w}_y$ are used in the MLE for data that is acquired from that coverslip. It is found for a given coverslip, that the measured $\overline{w}_x$ and $\overline{w}_y$ do not change significanty, even with manual stage movement in the $x$, $y$, and $z$ directions, as long as the z-locking mechanism described in Ch. 2 is providing feedback to

the piezoelectric objective mount. When a new coverslip is placed on the stage, the focus must be re-acquired, and the width must be measured again. Fig. 3.10c shows a histogram of the values of $w_x$ and $w_y$ plotted in 3.10b. From this, we calculate $\overline{w}_x$ and $\overline{w}_y$ and the standard deviations $\sigma_{w_x}$ and $\sigma_{w_y}$ of the widths. These not only reflect uncertainty of the widths, but also encompass the localization uncertainty which is limited by $\Delta t$ and the positioning uncertainty of the piezoelectric stage. Typically, $\Delta t = 3$ s is selected. This interval is short enough that the emitter has not moved significantly due to lateral drift, but long enough so that $\overline{N}$ will be fairly large, thus $\sigma_X$ and $\sigma_Y$ will be fairly small. The displacement that we chose to use, $D_S$= 50 nm, is much larger than the ~3 nm reported positioning uncertainty of the stage and the ~2 nm centroid localization uncertainty, but small enough that we do not move the emitter out of the probe region.

If the x and y axes of the fibers are not identical to x and y axes of the stage, this must be accounted for when measuring the PSF widths and for the correlated electron microscope imaging that is discussed in Chapter 5. We eliminate that step by ensuring that movements of the stage (for example, NSEW) correspond to identical movements of the emitter[28]. Fig. 3.11 illustrates the small mismatch (<3 degrees) between the stage and image axes that exists in our setup. A QD was moved 50 nm N, S, E, and W, and the black points label the locations found when assuming a symmetrical PSF with 250 nm widths. The red points label the locations found after recovering the correct displacement values was 220 nm in x and 250 nm in y. From both sets of locations, one can see

[28] Any 180-degree flips or 90-degree rotations necessary for aligning the stage and image axes can be done by swapping the defined locations of the pixels in the analysis software. We ensure that the respective kitty-corner pixels in the real detection scheme remain kitty-corner in the software-defined detection scheme, because some definitions for the pixel locations are impossible to achieve with flips and rotations of the detection scheme.

the slight counterclockwise rotation of the image which is caused by a slight rotation of the fiber bundle relative to the x and y axes of the stage that we disregard.

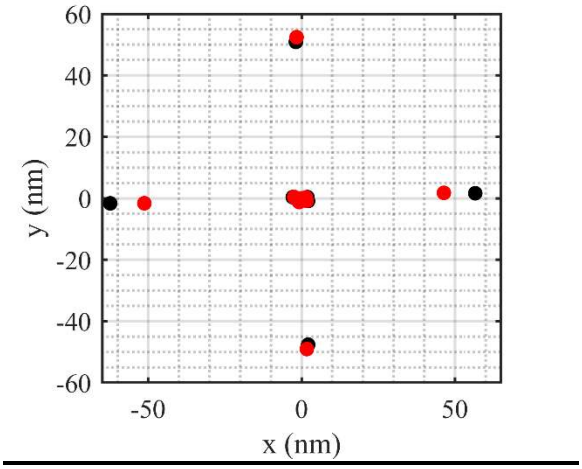


**Figure 3.11 Displacing a QD by 50 nm to recover the point spread funciton width.** A QD was moved 50 nm to the N, S, E, and W from the origin, and the black points label the centroid locations that were found assuming (incorrectly) a symmetrical PSF with a width of 250 nm. The red points label the centroid locations that were found using the measured PSF widths of 230 and 250 nm in x and y. The true 50 nm displacements are recovered when using the measured PSF. The slight counterclockwise rotation of the found locations relative to the x and y axes is because the xy axes of the detectors are rotated slightly relative to the xy axes of the stage.

On a side note, some readers might wonder how fluctuations in $w_x$ and $w_y$ impact the likelihood distriubiton and our localization precision. We can explore this by taking the PSF to be a Gaussian distribution centered at $\bar{w}_x$ and $\bar{w}_y$, and integrating $\mathcal{L}\left(X,Y;\ w_x,w_y,\{M_\mathrm{k}\},\{\beta_k\}\right)$, Eq. 3.18, over the distriubtion of $w_x$ and $w_y$ ,

$$\mathcal{L}_{red.}\ (X,Y;\{M_\mathrm{k}\},\{\beta_k\}) \tag{3.24}$$

$$= \frac{1}{2\pi\sigma_{w_x}\sigma_{w_y}}\iint dw_x dw_y\,\mathcal{L}(X,Y;w_x\ ,w_y,\dots)e^{-(w_x-\bar{w}_x)^2/2\sigma_{w_x}{}^2}e^{-(w_y-\bar{w}_y)^2/2\sigma_{w_y}{}^2}.$$

The integration broadens the likelihood distribution in $X$ and $Y$, reflecting our lack of knowledge in the value of the width. On the other hand, because the height of $\mathcal{L}\left(X,Y;\ w_x\ ,w_y\ ,\{M_{\mathrm{k}}\},\{\beta_k\}\right)$ is independent of $w_x$ and $w_y$ (as we saw earlier in this section), the most likely centroid location ($X_{max}, Y_{max}$) for the reduced distribution is the same as ($X_{max}, Y_{max}$) for the original distribution, $\mathcal{L}\left(X,Y;\ \overline{w}_x\ ,\overline{w}_y\ ,\{M_{\mathrm{k}}\},\{\beta_k\}\right)$.

While the MLE constructed in this manner accounts for astigmatism of the PSF, it unfortunately does not account for rotations that may exist. Through simulations of an emitter located within ~140 nm of the origin (or center of the fiber bundle in the image plane) with a rotated elliptical Gaussian PSF, we probed both the accuracy of finding the absolute location of an emitter, and the accuracy of finding the relative distance between closely spaced emitters when rotations were present and the MLE did not account for them. Provided that the emitter was not located at the origin, the rotation had a significant impact on the accuracy in finding the absolute location. We found that the localization inaccuracy was exacerbated by increasing the ellipticity, rotation angle, and absolute distance of the emitter from the origin. A 45° rotation caused the biggest discrepancy between the actual and found locations.

We were concerned about inaccuracies that our results would have because we were not accounting for possible rotations. To see how unaccounted rotations would impact our localization accuracy, we simulated an elliptical Gaussian with widths and absolute distance from the origin that were similar to the conditions found in experiments, and then we located the emitter with MLE assuming no rotation. The simulated PSF was 200 by 300 nm and rotated by 45 degrees. When analyzing the data, we did not assume the PSF was 200 by 300 nm, but instead we measured the PSF. For this, we simulated data for which the rotated PSF was repeatedly displaced by 50 nm from the origin in $x$ and $y$, and we solved for the widths $w_x$ and $w_y$ that would allow us to recover

the 50 nm displacements (the same way we did the measurement for experimental data described earlier in the section). For this measurement, we assumed the PSF was a 2-D Gaussian aligned along $x$ and $y$. We used the recovered $w_x$ and $w_y$ to test the accuracy of locating the centroid of the rotated PSF when it was placed different distances from the origin. There was up to a 10 nm discrepancy between the found and actual location when the PSF was placed 100 nm from the origin; the closer the emitter was to the origin, the less impact the rotation had on the accuracy. That suggests that the absolute locations of the centroids reported in this thesis may be misplaced by up to 10 nm depending on their departure from the origin. We also studied the effect of the rotations on the distance between closely spaced emitters. We found that the separation between emitters (8 nm was used as the simulated separation) was never significantly altered, regardless of rotation angle, ellipticity, or absolute distance of the emitters from the origin. That indicates we do not need to account for a rotated PSF in order to uncover the distances between closely spaced centroids, provided we are measuring the PSF widths in the manner described above.

Other groups with similar time-resolved detection schemes with few pixels have used an additional camera that has enough pixels to measure $w_x$ and $w_y$ by splitting the emission among the time-resolved detectors and the camera[57]. This is advantageous for systems in which there are changes in the focal position because that alters $w_x$ and $w_y$. With our method, we must re-measure $w_x$ and $w_y$ if the focal position changes. However, there is an advantage to using our method because it self-corrects for inconsistencies between the actual PSF, which is a Bessel function, and the surrogate Gaussian PSF, so that we recover correct absolute changes in distances and have an accurately scaled SR image. If we were to instead fit a Gaussian or Bessel function to an image of the PSF that has more pixels and use those fits to parameterize the Gaussian that we assume in the MLE, we would not necessarily achieve an accurately scaled image.

# CHAPTER 4. Examining quantum dot interactions part 2: Correlated Optical and Electron Microscope Imaging

As a reminder, in Chapter 2 we resolved multiple regions of emission within small QD clusters, and we found the lifetime and intensity of the emission differed among these regions for some of the clusters. Importantly, we identified regions that had lower intensity and significantly shorter lifetimes, often less than 20 ns, compared to the lifetimes of single QDs, which were all tightly distributed about ~40 ns. In a system where energy transfer is present, it can be shown that the emission from donor particles has a truncated lifetime and lower intensity. Given that, we hypothesized that energy transfer was responsible for the behavior we observed in clusters, and that the quenched lifetime and intensity were coming from regions of the clusters that were donating energy. We wanted to explain the behavior in the context of Förster transfer between donor and acceptor nanoparticles. However, the SR images only provided a picture of the average locations of the emission centroids, and a comparison to models for energy transfer would be more fruitful/concrete if we knew the number of QDs in the cluster and their true distances from one another.

To access that information, we developed a workflow for acquiring scanning electron microscope (SEM) images of the same clusters we examined with the time-resolved super-resolution microscope. Section 4.1 presents these "correlated" images and demonstrates our ability to carry out this measurement. In Section 4.2, we introduce four simple kinetic models- a single QD with a single radiative decay pathway, a single QD with both radiative and nonradiative decay pathways, a pair of non-interacting QDs, and lastly, a pair of interacting QDs. The first two models will be used in Section 4.3 to interpret the time-resolved data of single QDs, and the latter two

models will be used in Section 4.4 to interpret the data of pairs of QDs that we identified with the correlated SEM imaging.

To carry out the correlated measurements, which are described in further detail in Section 4.5, we spin-coated clustered QDs on SEM grids with 10-20 nm thick windows made of amorphous silicon nitride or amorphous silicon dioxide. Each grid was then inverted onto the surface of a glass coverslip before collecting optical images. The glass coverslip hindered our ability to collect emission, and we lost ~80-90% of the signal, but it ensured the immersion oil for the microscope objectives did not contaminate the sample prior to SEM imaging. A coordinate for each photoluminescent spot relative to the corner of the SEM window was measured, and this was used to find the identical cluster in the SEM so we could correlate the optical and electron images. Importantly, we found that the photoluminescence behavior of single QDs was significantly altered on the SEM grids compared to the behavior on glass coverslips presented in Section 2.2. This required us to re-characterize the behavior of single QDs because that informs our interpretation of the behavior of QD clusters.

## 4.1: Correlated optical and electron microscopy imaging

We start by presenting correlated time-resolved SR images and SEM images of QD clusters. The number of QDs in the clusters ranged from 2-10, and we have turned our attention to clusters containing only two QDs, for which the interpretation of the photoluminescence behavior in terms of simple kinetic models (as presented in the next section) will be more tractable. Fig. 4.1 displays data from six different pairs of QDs. They are organized from top to bottom according to their center-to-center separation distance measured from their SEM images, which are displayed in the left-hand column. The second and third columns display the SR images that are color-scaled

according to the average photon arrival time $\bar{t}$ and number of counts *N*, respectively[29]. (The positions in the images are identical, only the color-scaling changes.) Each point on a SR image corresponds to a centroid location that was found with 0.5 s of data, and each image is a composed of 300-500 s of data. The underlying structures from the SEM images agree with the SR images, and this is shown clearly in the fourth column, which overlays the SEM images and *N*-scaled SR images.

Centroid positions associated exclusively with the true locations of the QDs will only occur when one of the QDs has blinked completely off for the entire 0.5 sec interval and the other QD remains in an emissive state. Otherwise, the centroid location will be partway between the two QDs. Indeed, we identify many centroid locations partway between each pair because these QDs spend the majority of their time in the ON state.

[29] $\bar{t}$ is determined for each interval by taking the average of the arrival times of detected counts in the four pixels and then correcting for the arrival times of the background contribution by subtracting a weighted average of the background arrival time distribution. The counts *N* are the same as the counts that we defined as $\bar{N}$ in Chapter 3. We determine them by maximizing the likelihood distribution presented in Eqn. 3.19.

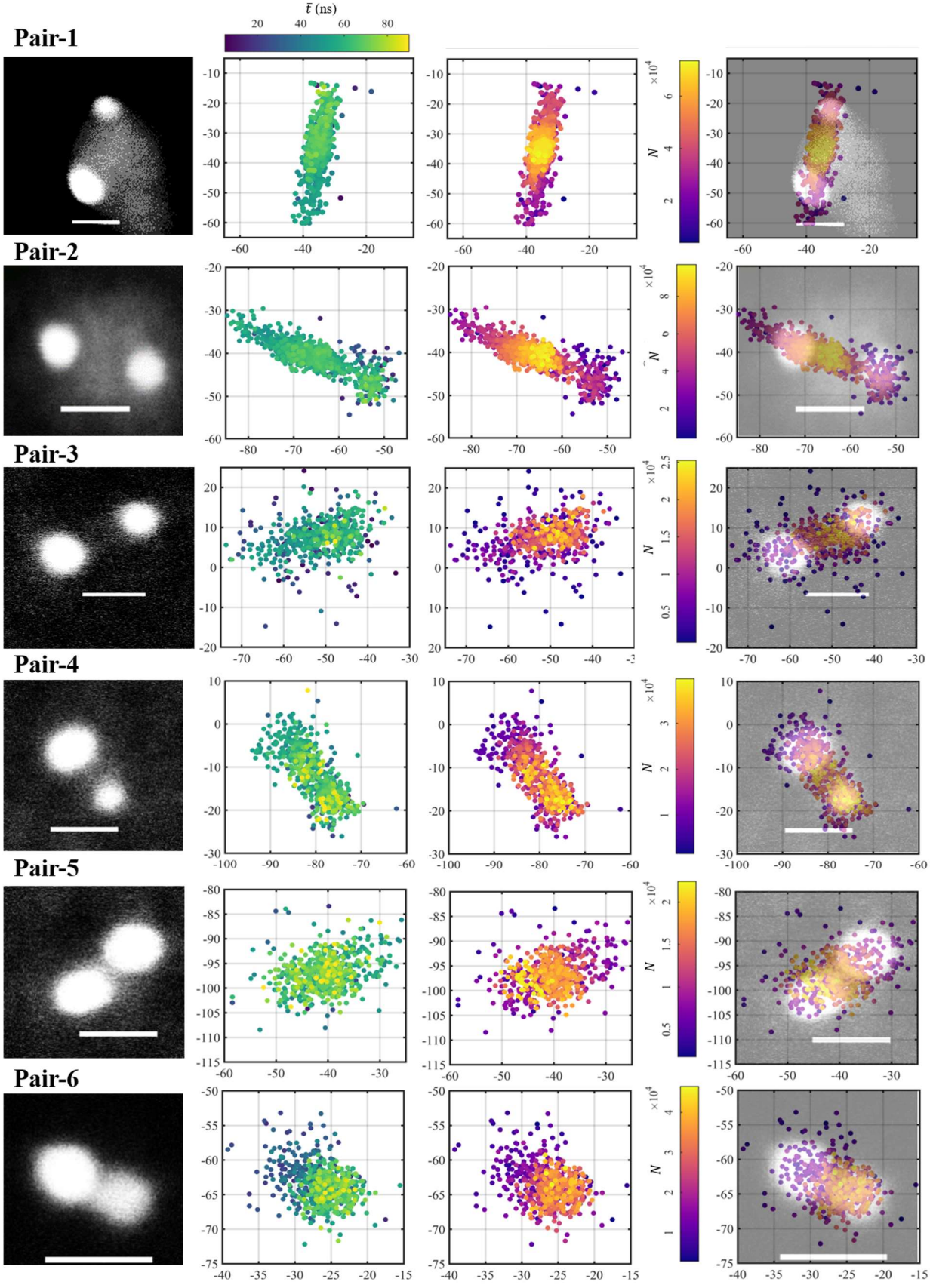
$\bar{t}$ (ns)
20
40
60
80
Pair-1
Pair-2
Pair-3
Pair-4
Pair-5
Pair-6
N
×10^4

**Figure 4.1 Electron and optical images of QD pairs.** Each row displays a different pair of QDs, organized from top to bottom with decreasing separation distances. The scale bars are 15 nm in every SEM image (first column). The second and third columns display SR images of each QD pair, where *x* and *y* axes correspond to the centroid position in nm that was determined every 0.5 s for 300-500 seconds per sample. The positions in columns two and three are identical. The images in column two are color-scaled according to $\bar{t}$, and that color scale is identical for all images; the images in column three are color scaled according to the counts *N*. Scales are identical across each row. Column 4 shows a superposition of the SEM (column 1) and SR (column 3) images.

The behavior of the first pair of QDs from Fig. 4.1, Pair-1, is highlighted in Fig. 4.2. The values of $\bar{t}$, *N*, x position, and y position as a function of time are plotted in 4.2(a-d), and their respective histograms are displayed in 4.2(e-h). The pair was rotated 10 degrees counterclockwise so that the separation vector between the two QDs in the SEM image was parallel with the y axis. This is convenient for observing position changes in the SR data caused by blinking, which will be seen exclusively in the *y* position. From the histogram of *y* positions (h), one can see that the majority of localizations are centered about y = -40 nm. By imposing intensity thresholding, we can eliminate segments of the data for which the *N* is high so both of the emitters are likely contributing to the emission. We recover the positions associated with lower *N*, which usually correspond to times when only a single QD is ON. Fig. 4.2i and j display histograms of *x* and *y* positions that remain after applying a threshold of *N* =39,000. This was found to be an optimal intensity threshold for recovering the precise locations of the individual QDs[30]. We can see the distribution of y positions is bimodal with peaks separated by 27 nm. Quite beautifully (though to be expected), this separation is nearly identical to the 28 nm center-to-center distance that we measure from the SEM image, highlighting our ability to resolve blinking emitters.

[30] The choice of thresholds is sensitive single we are working in the tail of the distribution. To peaks emerge as *N* is lowered below ~40,000. But as *N* is lowered below 39,000 there are few datapoints considerable loss of precision.

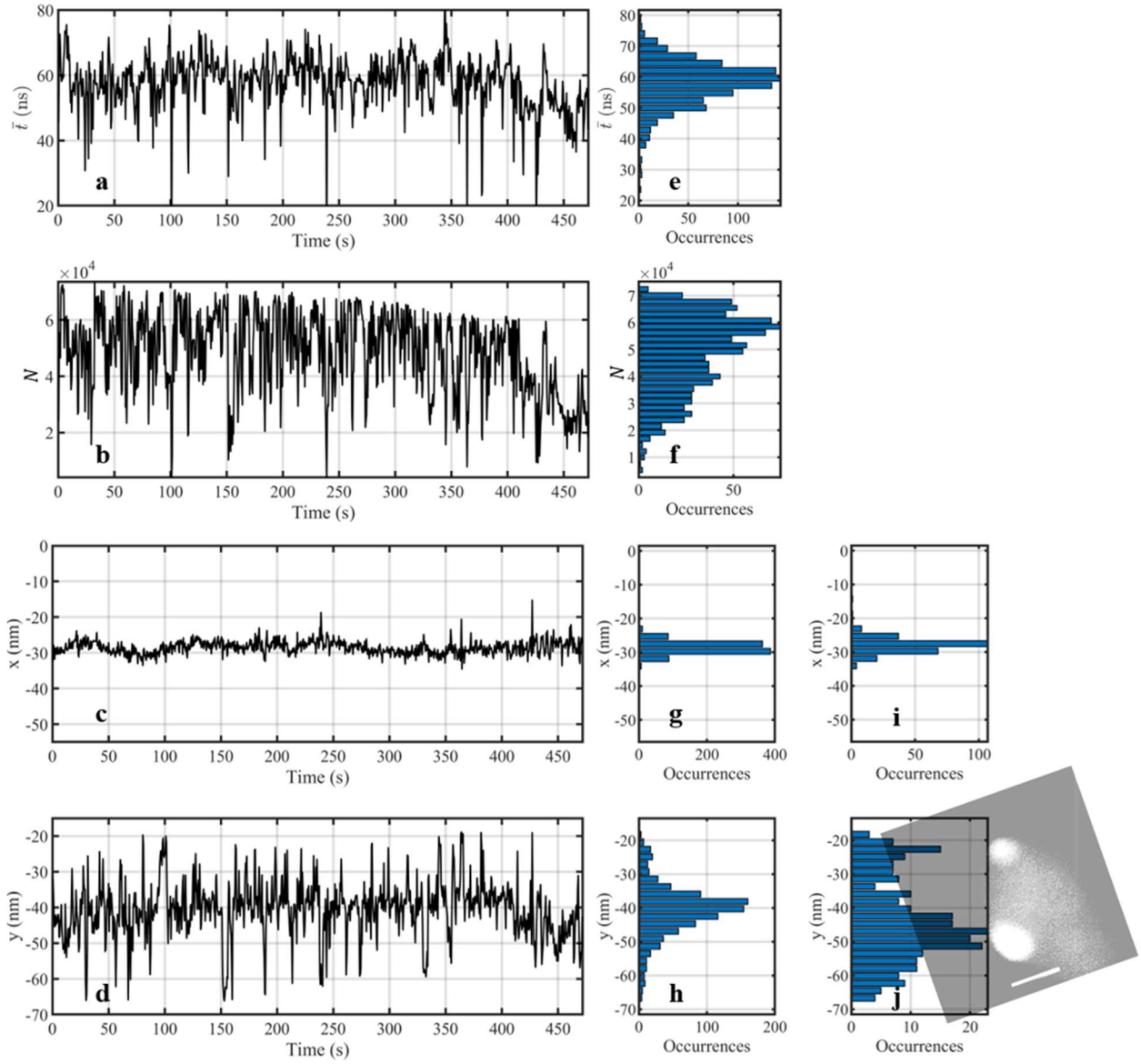


**Figure 4.2 Time-resolved super-resolution data from Pair-1.** The pair was monitored for 475 seconds, and the photons were binned every 0.5 sec to determine the (a) average arrival time $\bar{t}$, (b) counts *N*, (c) x position, and (d) y position. The cluster was rotated so that the separation vector between the QDs was parallel to the y axis. Histograms of the values for each observable are plotted in (e) through (h). With thresholding, we removed data for which there were greater than *N*=39,000, which allowed us to remove data for which both the QDs were likely in the on state. (i) and (j) show histograms of *x* and *y* positions, respectively, after thresholding. The bi-modal distribution of y positions has means that are separated by the same distance as the two QDs in the SEM image (superimposed).

While we sought to create clusters of QDs, we ended up forming and collecting correlated images of single QDs. Fig. 4.3a and b shows a SR images of a single QD for which we achieve 2 nm precision in x and y. Fig. 4.3a is color-scaled according to $N$ and (b) is color-scaled according to $\bar{t}$. The emission centroid is distributed about a single mean. The same QD was imaged with electron microscopy after the optical measurements, and that image is displayed in Fig. 4.3c. The QD is ~11 nm across. In this thesis, we will not try to glean anything else from the correlated single -dot images. However, we note recent work with correlated imaging has been devoted to the structural basis for optical behavior at the single particle level[85–87] and we could choose to examine how the PL blinking, lifetime, and intensity are related to the particle diameter and shape in the future. It is interesting note that we are getting 2 nm localization precision for finding the emission centroid of an object that is 11 nm across. One wonders if we should expect to spatially resolve multiple features on a QD and observe dynamics in the SR image for a single QD. If indeed there are spatially localized trap states associated with different radiative pathways, we are not observing them here, either because our localization precision is too low, or because we are averaging over many radiative decays with our 0.5 s bin times.

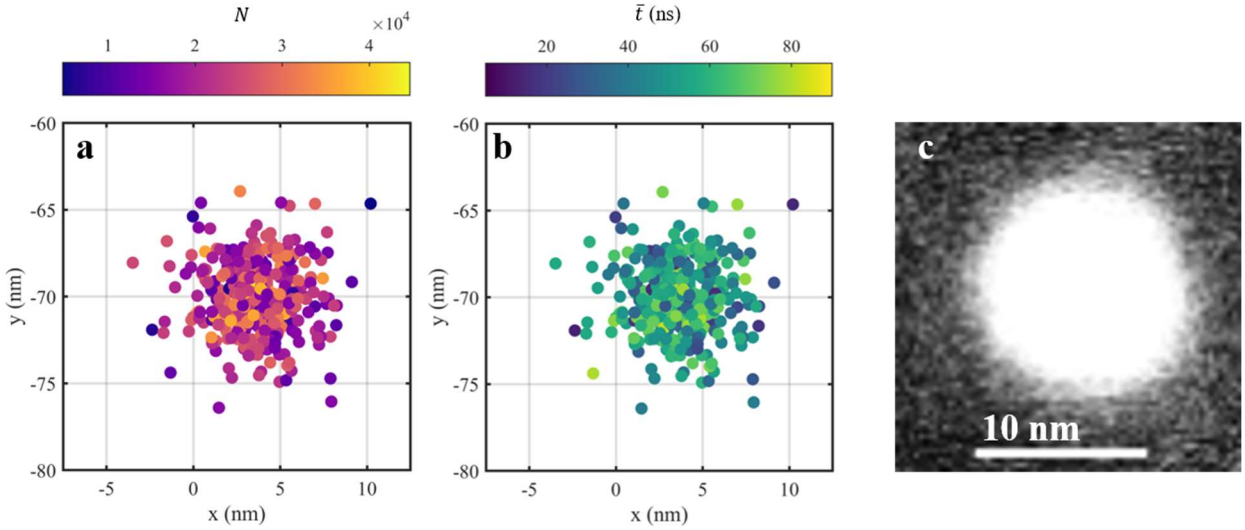


**Figure 4.3 Optical and electron microscopy images of a single QD.** The centroid position associated with a single QD is found every 0.5 s for 170 s. The positions are drift-corrected and

plotted with the color scale indicating counts $N$ (a) and average arrival time $\bar{t}$ in ns (b). The localization precision is 2 nm in x and y. The scanning electron micrograph image in (c) is collected from the same QD, which is revealed to have a diameter of ~ 11 nm. All three images have the same scale.

## 4.2: Simple models for independent and interacting emitters

Now we take the reader through calculations of the quantum yield, the arrival time distribution, and the average arrival times for models of increasing complexity. In the next section, we will interpret QD singles and pairs through the lens of these rate models.

***Case I: A single QD***

Let us first consider the case of a single QD that relaxes via a radiative decay pathway with a rate $R$. The probability $P(t)$ to be in the excited state at a time $t$ is governed by the rate equation,

$$\frac{dP(t)}{dt} = -RP(t), \tag{4.1a}$$

for which the solution

$$P(t) = P(0)e^{-Rt} \tag{4.1b}$$

is an exponential decay from the initial probability $P(0)$[31], the same as the one we are accustomed to seeing for the case of radioactive decay[88]. Since $RP(t)$ is the number of photons emitter per unit time, it follows that the quantum yield,

$$\Phi = \int_0^\infty RP(t)dt = P(0) \tag{4.1c}$$

is equal to the probability $P(0)$ that the QD was excited at a time zero. The arrival time distribution,

[31] Here is one way to understand that $\psi(t) = RP(t)$ is the probability distribution for emitting a photon at time $t$. Consider that $Rdt$ is equal to the number of times the system can relax during a time window $dt$ if the system is excited, and $P(t)$ is equal to the probability that the system is in the excited state at a time t. So the product $RP(t)dt$ is equal to the number of photons emitted by the system during $dt$.

$$\psi(t) = \frac{RP(t)}{\Phi} = Re^{-Rt} \tag{4.1d}$$

for a photon emitted by the QD is normalized by dividing the emission flux $RP(t)$ by $\Phi$. The first moment of the arrival time distribution is the average arrival time,

$$\bar{t} = \int_0^\infty \psi(t) t dt = \frac{1}{R}, \tag{4.1e}$$

which in this case is simply the lifetime $1/R$. When examining experimental data, it is easier to compute $\bar{t}$ than it is to compute $\psi(t)$—we get $\bar{t}$ by taking the average of the photon arrival times that we record, whereas to find $\psi(t)$ we must fit a multi-exponential decay to the histogram of recorded photon arrival times.

***Case II: A single blinking QD***

While we would like to keep our model as simple as possible, we must also account for blinking of the QDs, where blinking refers to a behavior in which the QD switches from an "ON" state described by equations 4.1(a-d), and stochastically and reversibly occupies a "OFF" state in which it emits less light. Blinking is discussed in further detail in Ch. 1. The arrival time distribution of photons that are emitted in the OFF state (if there are any at all) is typically narrower than the distribution of photons emitted in the ON state. Blinking occurs on a range of time scales in CdSe/CdS QDs from several milliseconds up to several minutes. One way to incorporate blinking within the model is to introduce a nonradiative decay pathway with a rate *D* that competes with *R*. When D is much larger than R, the QD effectively switches OFF. For this system, the probability for the system to be in the excited state at a time *t* is governed by the rate equation,

$$\frac{dP(t)}{dt} = -(R + D)P(t), \tag{4.2a}$$

and the excited state probability has a faster exponential decay than the previous case,

$$P(t) = P(0)\, e^{-(R+D)t}. \tag{4.2b}$$

Consequently, the quantum yield

$$\Phi = \int_0^\infty RP(0)\, e^{-(R+D)t} dt = \frac{R}{R+D} P(0)\ , \tag{4.2c}$$

is reduced by the factor $\frac{R}{R+D}$, the arrival time distribution

$$\psi(t) = \frac{RP(t)}{\Phi} = (R+D)e^{-(R+D)t} \tag{4.2d}$$

is narrower because it is governed by the sum $R + D$, from which it follows the average arrival time

$$\bar{t} = \int_0^\infty \psi(t) t dt = \frac{1}{R+D} \tag{4.2e}$$

is smaller. Notice that both the lifetime and the quantum yield decrease as D increases, which agrees with experimental findings of correlated lower intensity and shorter lifetime emission during blinking events[52,89].

***Case III: Two non-interacting QDs***

Now consider a system that consists of a cluster of two non-interacting QDs. The excited state probability $P_1(t)$ for the first QD, "QD1", is governed by

$$\frac{dP_1(t)}{dt} = -(R_1 + D_1)P_1(t), \tag{4.3a}$$

and the excited state probability $P_2(t)$ for the second QD, "QD2", is governed by

$$\frac{dP_2(t)}{dt} = -(R_2 + D_2)P_2(t) \tag{4.3b}$$

These are two independent versions of case II, so the results just add. The quantum yield is the sum

$$\Phi = \Phi_1 + \Phi_2 = \frac{R_1}{R_1 + D_1} P_1(0) + \frac{R_2}{R_2 + D_2} P_2(0) \tag{4.3c}$$

of the quantum yields of both QDs. The normalized photon arrival distribution

$$\psi(t) = \frac{1}{\Phi}\big(R_1 P_1(t) + R_2 P_2(t)\big) = w_1(R_1 + D_1)e^{-(R_1+D_1)t} + w_2(R_2 + D_2)e^{-(R_2+D_2)t} \tag{4.3d}$$

is a weighted sum of the arrival time distributions for QD1 and QD2, with weights given by

$$w_1 = \frac{\frac{P_1(0)R_1}{D_1+R_1}}{\frac{P_1(0)R_1}{D_1+R_1}+\frac{P_2(0)R_2}{D_2+R_2}}, \tag{4.3e}$$

and

$$w_2 = 1 - w_1 = \frac{\frac{P_2(0)R_2}{D_2+R_2}}{\frac{P_1(0)R_1}{D_1+R_1}+\frac{P_2(0)R_2}{D_2+R_2}}. \tag{4.3f}$$

Thus, we see that a bi-exponential arrival time distribution (which we will observe later in this chapter) can be interpreted in the context of a model of two independent emitters. Lastly, the average arrival time is a weighted sum

$$\bar{t} = \int_0^\infty \psi(t) t dt = \frac{w_1}{(R_1 + D_1)} + \frac{w_2}{(R_2 + D_2)} \tag{4.3g}$$

of the lifetimes of the individual QDs.

***Case IV: Two interacting QDs***

The last case we will examine is that of two quantum dots that are interacting through Förster transfer. Here, the two rate equations from case III are coupled. We will assume that the band gap of QD2 is much smaller than QD1, so the Förster transfer is predominantly from QD1 to QD2, and reverse energy transfer from QD2 back to QD1 is negligible. The coupled equations are,

$$\frac{dP_1(t)}{dt} = -(R_1 + D_1 + F)P_1(t), \tag{4.4a}$$

and

$$\frac{dP_2(t)}{dt} = -(R_2 + D_2)P_2(t) + FP_1(t), \tag{4.4b}$$

with solutions given by[90]

$$P_1(t) = P_1(0)e^{-(R_1+D_1+F)t}, \tag{4.4c}$$

and

$$P_2(t) = P_2(0)e^{-(R_2+D_2)t} + \frac{FP_1(0)}{(F+R_1+D_1-R_2-D_2)}\left(e^{-(R_2+D_2)t} - e^{-(R_1+D_1+F)t}\right). \tag{4.4d}$$

The normalized distribution of arrival times is

$$\psi(t) = \frac{R_1P_1(t)+R_2P_2(t)}{\Phi}, \tag{4.4e}$$

where the quantum yield

$$\Phi = \int_0^\infty \left(R_1P_1(t) + R_2P_2(t)\right)dt \tag{4.4f}$$

acts as normalization constant. Substituting 4.4c and 4.4d into 4.4e and 4.4f, we find

$$\psi(t) = \left[\left(R_1P_1(0) - \frac{R_2FP_1(0)}{(F+R_1+D_1-R_2-D_2)}\right)e^{-(R_1+D_1+F)t} + \left(R_2P_2(0) + \frac{R_2FP_1(0)}{(F+R_1+D_1-R_2-D_2)}\right)e^{-(R_2+D_2)t}\right]\frac{1}{\Phi}, \tag{4.4g}$$

where

$$\Phi = \frac{R_1P_1(0)}{(R_1+D_1+F)} + \frac{R_2P_2(0)}{(R_2+D_2)} + \frac{R_2FP_1(0)}{(F+R_1+D_1-R_2-D_2)(R_2+D_2)} - \frac{R_2FP_1(0)}{(F+R_1+D_1-R_2-D_2)(R_1+D_1+F)}, \tag{4.4h}$$

Lastly, the average arrival time can be written,

$$\bar{t} = \int_0^\infty \psi(t)tdt = \frac{1}{\Phi}\left(\frac{R_1P_1(0)}{(R_1+D_1+F)^2} + \frac{R_2P_2(0)}{(R_2+D_2)^2} + \frac{R_2FP_1(0)}{(F+R_1+D_1-R_2-D_2)(R_2+D_2)^2} - \frac{R_2FP_1(0)}{(F+R_1+D_1-R_2-D_2)(R_1+D_1+F)^2}\right). \tag{4.4i}$$

Eqn. 4.4g shows that the arrival time distribution is a bi-exponential. This begs the question of whether or not this interacting system can be distinguished from the non-interacting system of case

III, for which the distribution was also a bi-exponential. Notably, when the radiative and nonradiative decays are equal (so $R_1 = R_2$ and $D_1 = D_2$), $\Phi$, $\varphi(t)$, and $\bar{t}$ will all be equivalent to the case of two non-interacting emitters (equations 4.3 c, d, and g).

We now consider how blinking would impact this interacting system (Eqn. 4.4g) by taking the limits as the nonradiative decay rates go to infinity. For the case where the acceptor turns OFF ($D_2 \to \infty$) but F remains the same, we see that only the first term of $\psi(t)$ survives,

$$\psi(t) = \frac{1}{(R_1+D_1+F)} e^{-(R_1+D_1+F)t}, \tag{4.5}$$

and the decay will be a mono-exponential with a lifetime $\bar{t} = 1/(R_1 + D_1 + F)$. It follows that $\Phi$ decreases to $\Phi = \frac{R_1 P_1(0)}{(R_1+D_1+F)}$. This explains the energy transfer signature of shorter lifetime and lower emission that we referred to in Chapter 2, and which is often used to diagnose energy transfer in the literature. On the other hand, for the case where the donor turns off ($D_1 \to \infty$) the system behaves like an isolated QD described by Eqns. 4.2c-d. There will be no indication that energy transfer is taking place.

## 4.3: Interpreting single quantum dot behavior

Let us now turn our attention to the quantum yields, arrival time distribution, and average arrival time observed in single QDs, which we will use to interpret more QD cluster behavior in Section 4.4. The average arrival time $\bar{t}$ of photons and the number of counts *N* for a single QD[32] and are plotted in Fig. 4.4. We should/can interpret *N* as a scaled version of the quantum yield. $\bar{t}$ is determined for every 0.5 sec interval for 170 s and is plotted versus time in Fig. 4.4a. A histogram of the $\bar{t}$ values in Fig. 4.4b shows a distribution that is centered about 57 ns. *N* is also determined for every 0.5 sec interval, and it is plotted versus time in Fig. 4.4c. A histogram of *N* in Fig. 4.4d

[32] This is the same QD that was examined in Fig. 4.3.

shows a distribution that is centered about 25,000 counts. We attribute fluctuations in $\bar{t}$ and $N$ to charges that are temporarily trapped on the QD, providing non-radiative pathways for the system to relax[15,91]. In the context of the model described by Eq. 4.2(a-c), the nonradiative rate D would fluctuate due to charging and this would cause $\bar{t}$ and Φ to change accordingly. Additionally, the trapped charges may change the transition dipole which, in turn, would change both the probability of excitation $P(0)$ and the radiative rate $R$ [92].

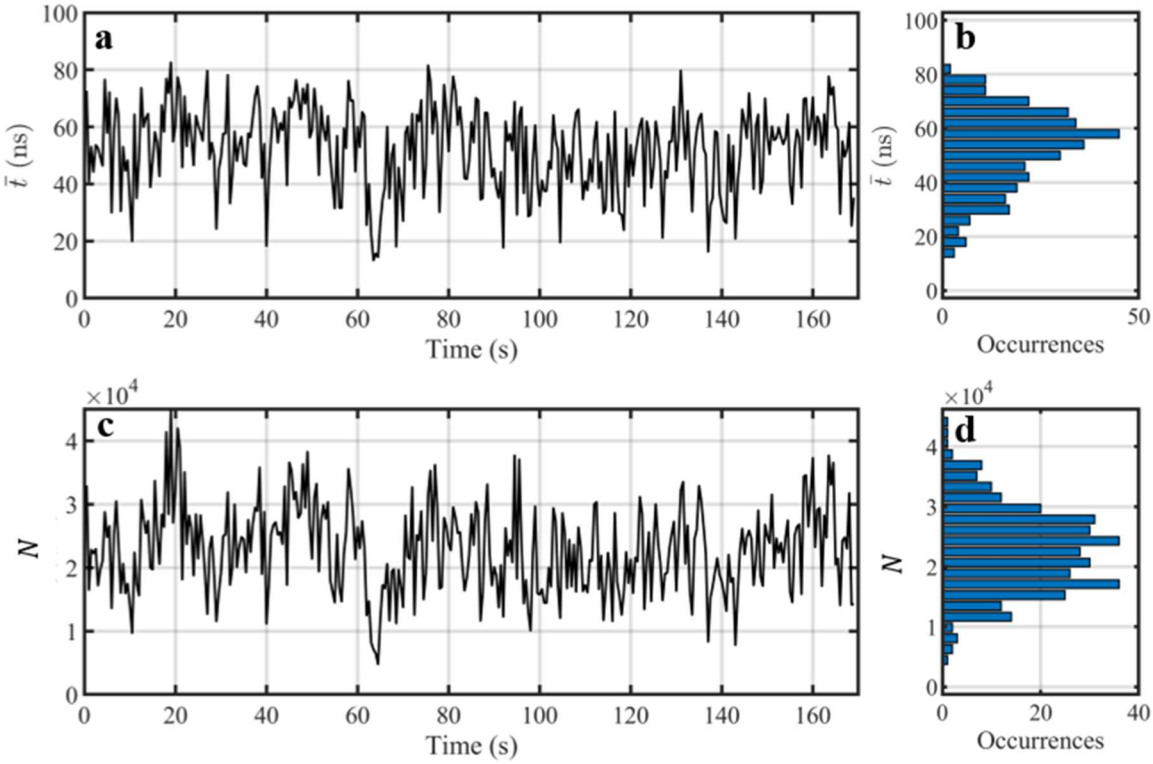


**Figure 4.4 Representative time-resolved microscope data from an isolated QD**. (a) The average arrival time $\bar{t}$ for photons emitted by the QD is determined every 0.5 sec for 170 seconds of data and a histogram (b) of $\bar{t}$. (c) The number of counts $N$ is determined for every 0.5 s with MLE[1] and (d) a histogram $N$.

A compilation of the normalized histograms of the $\bar{t}$ and $N$ for 44 single QDs that were attained with 0.5 sec bins are displayed in Fig. 4.5, illustrating the large variation in behavior among different single QDs. Each sample was studied under the same excitation conditions for durations between 60 and 1200 seconds (the median experiment duration was 300 s). The samples

are organized according to the mean value of $\bar{t}$ from smallest to largest, which ranges from 10-90 ns. Fig. 4.5a displays the distributions of $\bar{t}$, which are ~10 ns wide for each sample. Fig. 4.5b shows the same distributions as a contour plot. Fig. 4.5c displays the distributions of *N* in each sample, and Fig. 4.5d displays the same distributions as a contour plot.

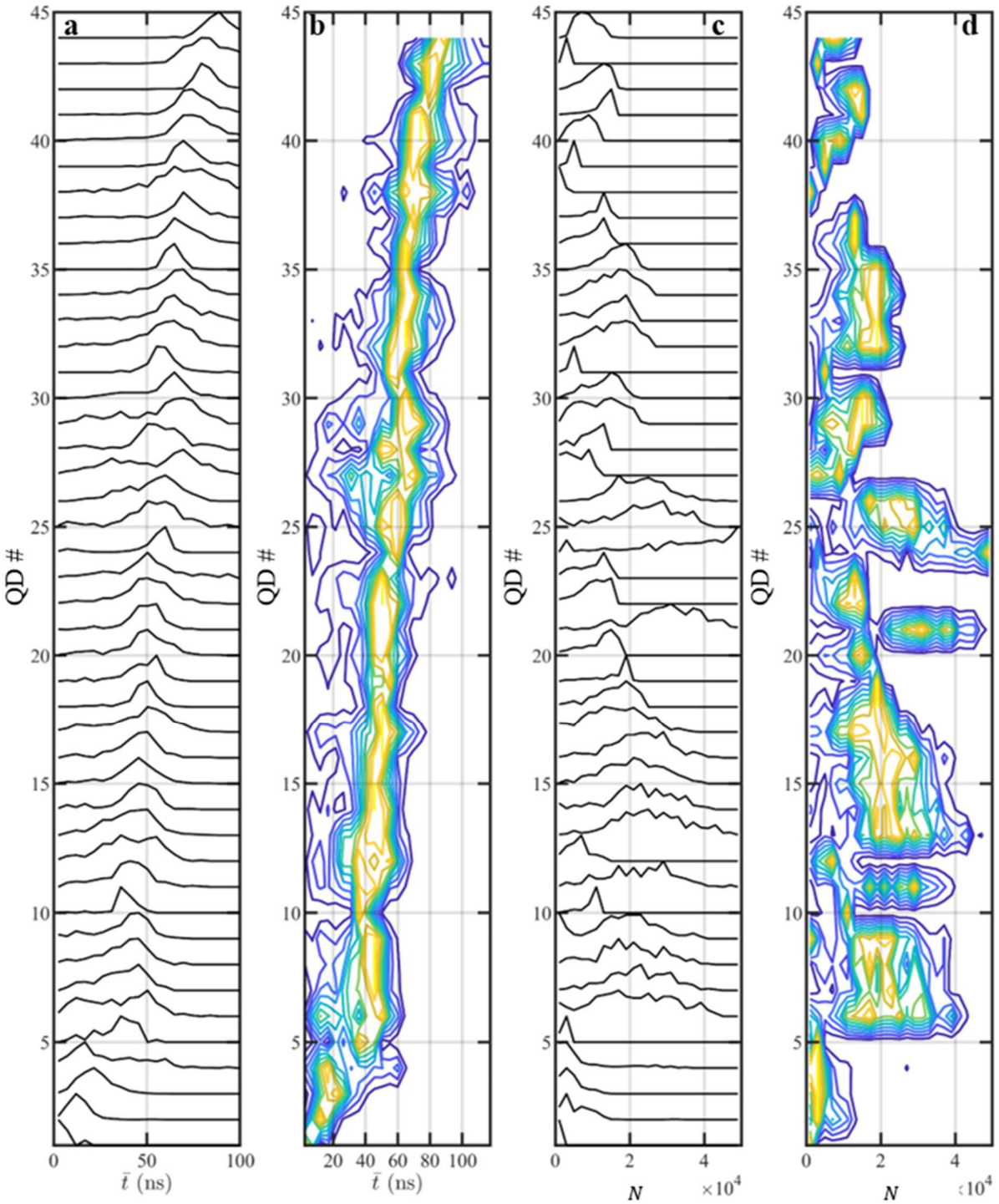


**Figure 4.5 Compilation of average arrival time and counts for single QDs** (a-b) normalized histograms of the $\bar{t}$ values in ns for 44 different QDs, (c-d) normalized histograms of the counts $N$ for each single QD. The values for $\bar{t}$ and $N$ were determined for every 0.5 sec interval, and each QD was studied for between 60 and 1200 sec.

The relationship between $N$ and $\bar{t}$ is illustrated in Fig. 4.6a for a single QD[33]. This type of plot is commonly referred to as a fluorescence lifetime intensity distribution (FLID). It is useful to realize that $N$ is directly proportional to the quantum yield $\Phi$, so the FLID should be interpreted as a plot of a scaled $\Phi$ versus $\bar{t}$. Let us therefore attempt to interpret the FLID in terms of the kinetic model for the single QD with blinking that we introduced in the previous section. Because we are interested in learning about the blinking behavior, we must focus on the portions of the FLID where $N$ changes, and this is in the tail of the distribution. This happens less frequently, but we will focus our attention on this data. In the previous section, we saw that $\Phi = \frac{P(0)R}{R+D}$ and $\bar{t} = \frac{1}{R+D}$ for this model ("case 2"), so the FLID is a plot of $\Phi = P(0)R\bar{t}$. If $P(0)R$ were independent of $\bar{t}$, a plot of $\Phi$ versus $\bar{t}$ should be a straight line with a slope $P(0)R$. If $P(0)R$ was dependent on $\bar{t}$, then $\Phi$ would *not* be linearly related to $\bar{t}$. In trying to understand whether or not a relationship exists between $P(0)R$ and $\bar{t}$, it is then useful to consider the plot of the log($\Phi$) versus the log($\bar{t}$); the slope of that will be equal to one if $P(0)R$ is constant, whereas the slope will be greater or less than one if $P(0)R$ changes with $\bar{t}$. In Fig. 4.6a, we show a log-log plot of $N$ (which is a scaled $\Phi$) versus $\bar{t}$. The logarithmic slope is nearly one, which supports the hypothesis that $P(0)R$ is independent of $\bar{t}$. We should then consider that $\bar{t} = \frac{1}{R+D}$ and understand that $R$ is likely constant (unless $P(0)$ and $R$ are *both* changing and cancelling one another out). This means that changes in $D$ are likely responsible for the blinking.

[33] This happens to be the same QD that was examined in Figs. 4.3 and 4.4.

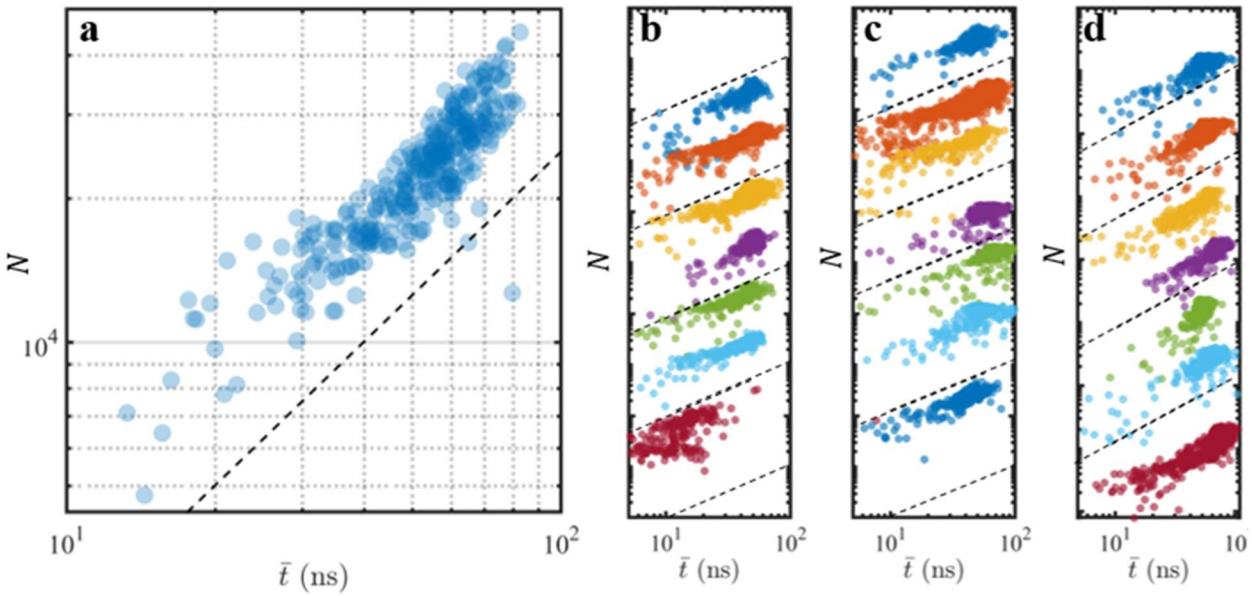


**Figure 4.6 Fluorescence lifetime intensity distributions (FLIDs).** (a) The counts $N$ versus average arrival time $\bar{t}$ in ns for data from the representative QD highlighted in the text and Figs. 4.3 and 4.4. Panels (b-d) plot $N$ versus $\bar{t}$ for 21 other QDs. The y-axes are scaled for visualization. The logarithmic slope is around one for all the FLIDs, and the dashed line with a slope of one has been added as a guide to the eye.

As long as we are only interested in the logarithmic slope, a log-log plot is also useful for comparing the scaled $\Phi$ versus $\bar{t}$ relations for many different QDs on a single graph. Fig. 4.6b-d shows examples of many FLIDs, which have been artificially shifted up and down relative to one another. We observe that the logarithmic slope is equal to one for nearly all the QDs that we examine. Outliers exist with a non-unity slope, and these might be examples of QDs for which there *is* a relationship between $P(0)R$ and $\bar{t}$.

A simpler model to explain the tails of the FLIDs would be to consider "case 1" that we introduced in the previous section, which we can get from case 2 by setting $D$ equal to zero. For this possible scenario, the FLID would simply be a plot of $\Phi = P(0)$ versus $\bar{t} = \frac{1}{R}$. Changes in $P(0)$ and $R$ and would (of course) cause changes in $\Phi$ and $\bar{t}$, but would they cause the relationship that we observe? We know that $P(0)$ is proportional to the absorption rate, and we know that both

the absorption rate and radiative rate $R$ are governed by the same physical mechanisms (the transition dipole moment)[92]. Given that, we might expect that as $R$ increases, $P(0)$ also increases, so that $\Phi$ decreases with increasing $\bar{t}$. Obviously, we see the opposite of this trend in the FLIDs of single QDs (Fig. 4.6), which supports the assumption that $D$ must be included in our model. On the other hand, we see a hint of a relationship between $R$ and $P(0)$ by turning our attention away from the tail behavior and plotting the *average* values of $\bar{t}$, $\langle \bar{t} \rangle$ and the *average* values of $N$, $\langle N \rangle$ from each FLID for many single QDs, as shown in Fig. 4.7. A dashed line with a slope of negative one fits well through the data. A slope of negative one implies that $P(0)$ is directly proportional to $R$, and suggests that the transition dipole is different for each QD.

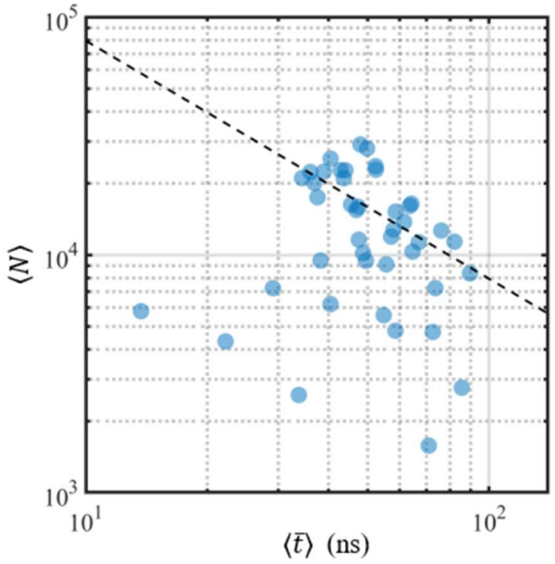


**Figure 4.7 Average fluorescence lifetime intensity distribution. The** mean of the counts $\langle N \rangle$ and mean of the arrival times $\langle \bar{t} \rangle$ were determined from the FLIDs for 44 isolated single QDs and plotted here (these are the same samples highlighted in Fig. 4.5). This average FLID bears little resemblance to the FLIDs of individual QDs shown in Fig. 4.6, and it does not show that the counts and $\bar{t}$ are proportional. Instead, it may show the opposite trend- that the counts and $\bar{t}$ are inversely proportional, and the dashed line is meant to highlight that relationship. For a typical system, we expect the probability of excitation and the rate of emission to be directly proportional, and the behavior of this FLID may indicate that.

For the sake of completeness, we have also characterized $\psi(t)$ by fitting the fluorescence decays. A bi-exponential performed best without over-parameterizing the fit. The biexponential

$\psi(t) = \frac{w_1}{\tau_1} e^{-t/\tau_1} + \frac{w_2}{\tau_2} e^{-t/\tau_2}$ was characterized by two lifetimes $\tau_1$ and $\tau_2$, and two weights such that $w_1 + w_2 = 1$. For this analysis, we did not de-convolve the data from the instrument response function (IRF), which is discussed in Section 2.4, though we did consider the IRF when choosing where to begin the fit. To avoid characterizing time-scales where the IRF would impact the data the most, we chose to begin our fit at 6 ns beyond the peak of the IRF. An example of a bi-exponential fit for a 0.5 ns time window is plotted in Fig. 4.8a[34]. To ensure that the fit performed well through multiple decades of the decay, we fit the data on semi-log axes. We found this procedure gave robust fits for single QDs, even as their lifetimes and counts fluctuated dramatically. Fig. 4.8b and c show the distributions in the lifetimes $\tau_1$ and $\tau_2$ extracted from the fit for 43 different QDs. (These sample numbers correspond to the same ones that were shown in Fig. 4.5.) Not all of the fits were reliable – especially time segments in which only a single exponential was necessary to get a good fit - the second exponential and its weight tended to run amok in those cases. We culled the data before making the lifetime histograms by tossing out fits in which we were less than 70% confident in the values of the parameters. Fits for which one lifetime and its corresponding weight were determined with high precision while the other lifetime and its weight were determined with low precision were indicative of a case where a mono-exponential fit was adequate. In those cases, we ignored the lifetime and weight that had low precision.

[34] Each bin in the arrival time histogram is 0.96 ns. Does this seem like an odd selection? It should. The temporal resolution of the Hydraharp is 16 ps. If we do not bin the arrival time data in multiples of 16 ps, the histograms will alternate between having fewer and more counts because it will be impossible to fit an integer number of 16 ps into 1 ns or other natural choices. This will give the histogram a comb-like appearance.

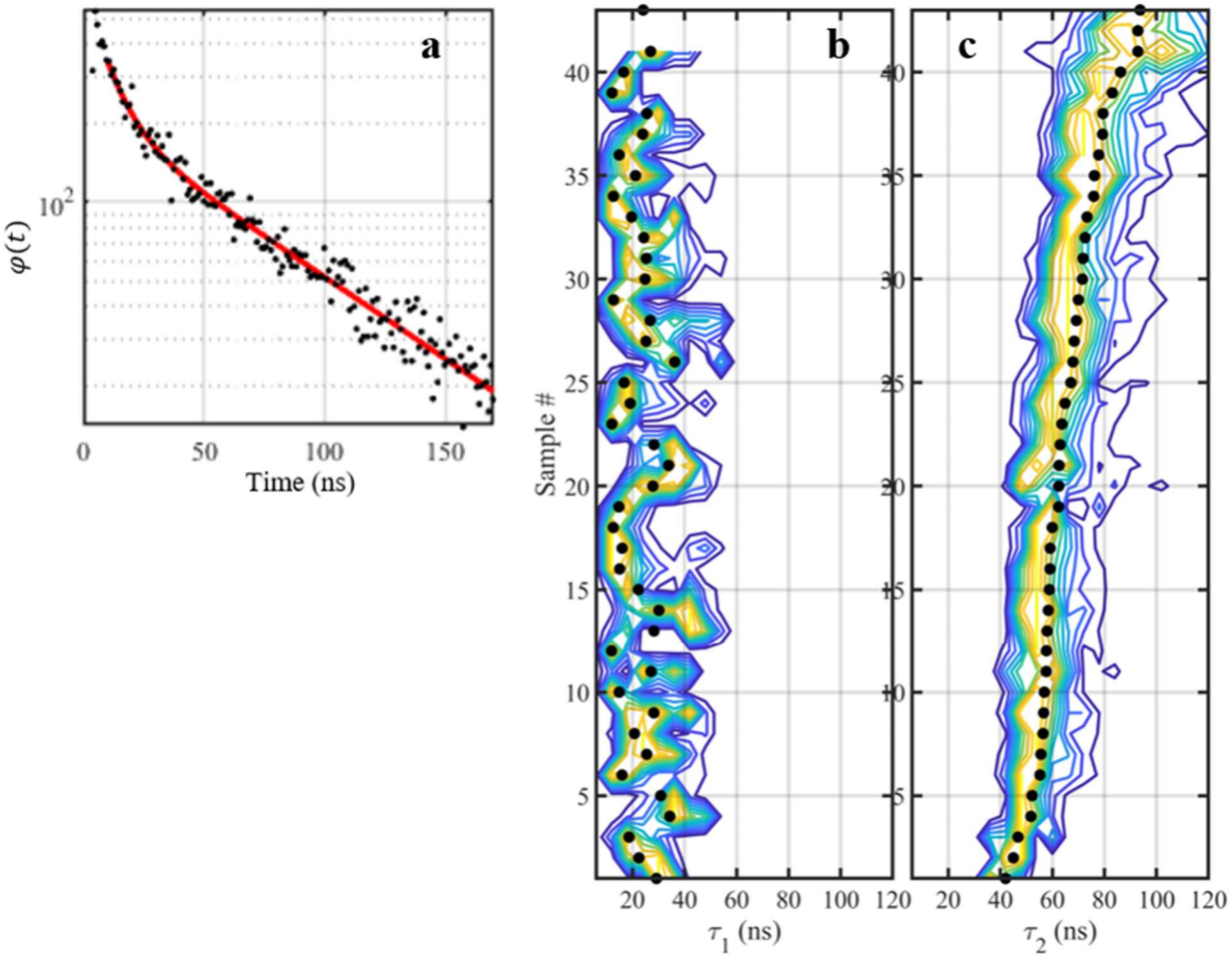


**Figure 4.8 Bi-exponential fits for characterizing the arrival time distributions of single QDs.** (a) A bi-exponential tail fit (red) to the histogram of photon arrival times acquired during a 0.5 s bin. Histograms of the short tau1 and long tau2 lifetime parameters were made for 43 different single QDs and plotted in (b) and (c), respectively. The black points label the mean of each distribution. Each QD was examined for 60-1200 seconds, and samples 1-43 correspond to sample #1-43 of the data shown in Fig. 4.5. Fit parameters with <70% confidence were not included in the histograms.

## 4.4: Interpreting quantum dot pair behavior

Let us now turn our attention back to the pairs of QDs introduced in Section 4.1. Recall the model of two interacting emitters from Eqns. 4.4a-i. One of the more obvious signatures of energy transfer will be a combined decrease in both $\Phi$ and $\bar{t}$, which will occur if the acceptor QD turns off ($D_2 \gg R_2$) but continues to accept energy. We notice that Pair-6, separated by 8.7 nm, may

have this signature; from the SR images displayed in Fig. 4.1 we notice that the emission centroids on the left are associated with a lower *N* and shorter $\bar{t}$ relative to the centroids on the right. We would like to try to explain the behavior with the simplest possible models in mind. Fig. 4.9 displays more data from this pair that we can examine to aid our discussion. The $\bar{t}$, *N*, x position, and y position are determined every 0.5 s and plotted versus time for 300 s of data. Their respective histograms are plotted to the right. Once again, the pair has been rotated so that their separation vector is parallel to the y axis. In this case, $\bar{t}$, *N*, and y position simultaneously change (as opposed to the previous example where we saw simultaneous changes in only the position and *N*). We can use either $\bar{t}$ or *N* to threshold the data as we did in the previous case. Using $\bar{t}$=40 ns as a threshold, we can identify *N*, x, and y associated with segments above (plotted in red) and below (plotted in blue) the threshold. We can see that the shorter $\bar{t}$ values correspond to lower intensities and a distribution of y positions with a mean of -6.2 nm (standard error of the mean is 0.3 nm). Longer $\bar{t}$ values correspond to higher intensities and a distribution of y positions centered about y = -10.2 nm (standard error of the mean is 0.1 nm). On average, the y positions of the two distributions are separated by 4.0 +-0.3 nm. We found that we could achieve the same separation by thresholding *N* at a value of ~15,000. We could not achieve a separation distance of greater than 4 nm by lowering or raising the thresholds on either *N* or $\bar{t}$. One would expect to observe a distance in the SR image that approaches their actual separation distance of 8.7 nm if we have examined the pair for enough time to capture the QDs in various ON and OFF states. Perhaps our measurement was merely not long enough to do this. However, a more interesting explanation for the 4 nm separation is that while the centers are separated by 8.7 nm, the interaction between the two QDs may cause the most probable locations for exciton recombination and emission from each of the QDs may only be separated by 4 nm.

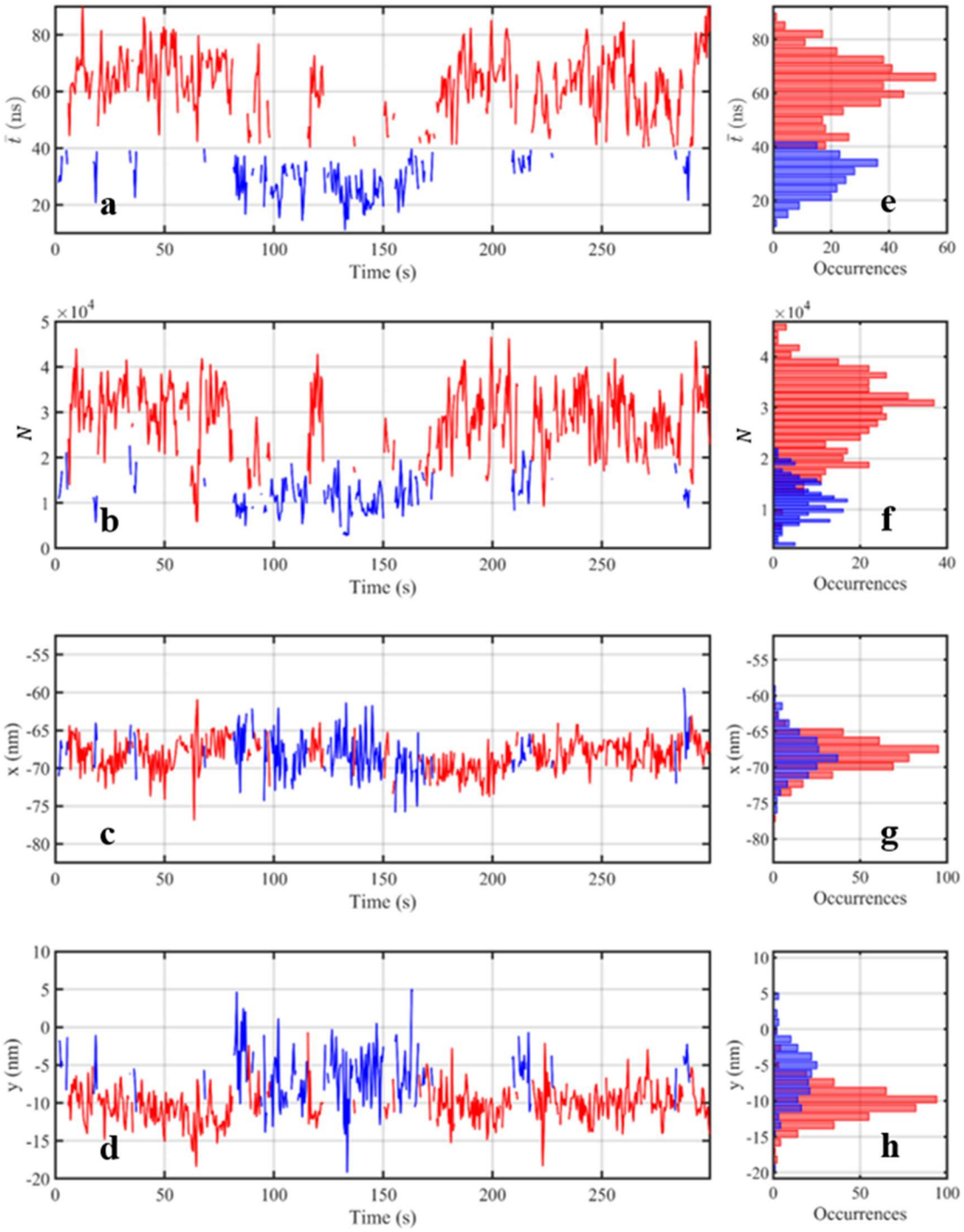


**Figure 4.9 Time-resolved super-resolution data from Pair-6.** Pair-6 from Fig. 4.1 was monitored for 300 seconds, and the photons were binned every 0.5 sec to determine the (a) the average arrival time $\bar{t}$ (b) counts $N$, (c) x position, and (d) y position. The pair was rotated so that the separation vector between the QDs was parallel to the y axis. The data is color coded according to the value of $\bar{t}$ in each bin; red indicates $\bar{t}$>40 ns and blue indicated $\bar{t}$<40 ns. Histograms of the

values for each observable are plotted in (e) through (h); the data for $\bar{t}$>40 ns and $\bar{t}$<40 ns are histogrammed separately and colored accordingly.

Rather than focus on $\bar{t}$, this time we will consider the distribution of arrival times $\varphi(t)$, determined by histogramming the photon arrivals. Like the arrival time distributions for single QDs, the distributions for pairs of QDs also fit well to a biexponential $\varphi(t) = w_1\left(\frac{1}{\tau_1}e^{-\frac{t}{\tau_1}}\right)+$ $w_2\left(\frac{1}{\tau_2}e^{-\frac{t}{\tau_2}}\right)$, with weights $w_1$and $w_2$ and lifetimes $\tau_1$ and $\tau_2$, respectively. Fig. 4.10a-d show the fit parameters determined every 0.5 s for Pair-6. For the majority of the 300 sec, we found that $\tau_1$ fluctuated about 20 ns with a weight $w_1$ of ~0.2, while $\tau_2$ fluctuated about 70 ns with a weight $w_2$ of ~0.8. Fits were tossed out for which we were not >70% confident in their parameters. It was rare that the system was completely non-emissive so that neither parameter could be determined with confidence. Though there were many time bins for which the decay was mono-exponential, and for these instances, $\tau_1$ and $w_1$ could be determined with confidence but $\tau_2$ and $w_2$ could not be determined, or visa versa. In those cases, we would assign the confident lifetime 100% of the weight. For ~70% of the data, we confidently determined all four parameters, and we found that the longer lifetime dominated the decay, $w_2$ contributed ~80% of the weight. However, for time bins where the decay was mono-exponential, we could usually only determine the shorter lifetime contribution with confidence and the longer lifetime contribution went away. This is most obvious for the segment between ~100 and 200 sec where $\tau_2$ is not plotted because we are not confident in its fit, $w_2$ is set to zero, and $w_1$ is set to one.

Let us entertain the possibility that $\tau_1$ and $w_1$ correspond to the contribution of one QD, and $\tau_2$ and $w_2$ correspond to the contribution of the other QD. If this is the case, we should expect the positions associated with these two contributions to be separated by ~8.7 nm. We then sort the position data based on which contribution has the larger weight. The final two panels of Fig. 4.10

plot the centroid position versus time, and are color coded to indicate the positions for which $w_1$ is greater than $w_2$ (blue), or $w_1$is less than $w_2$ (red). With this thresholding, we find that the two centroids are separated by 3.3 +-0.3 nm. They are closer in proximity than what we found by thresholding *N* and $\bar{t}$. We suspect this is because the fits to the bins containing few counts had to be tossed out because they were not within the confidence bounds that we required, but these bins with few counts were also more likely to correspond to emission from a single QD. These same bins help to identify the location of the QD with the low counts and short lifetime, and we were able to keep them when we did the simple counts and $\bar{t}$ thresholding.

The simplest model that can describe the behavior of Pair-6 is that of two non-interacting emitters (albeit that is a bit anticlimactic). Based on the broad distribution in $\bar{t}$, *N,* and $\varphi(t)$ that was observed among different single QDs (shown in Fig. 4.5 and 4.8), it is possible that the QD with the shorter lifetime merely has a higher nonradiative decay rate than the other one, and that is the end of the story.

If energy transfer is indeed occurring in these systems, we wonder if we can interpret the biexponential in the context of equation 4.4g in order to determine the energy transfer rate $F$. We simplify our analysis by considering the case of $D_1 = D_2 = 0$. In this limit,

$$\varphi(t) = w_1\left(\frac{1}{\tau_1}e^{-\frac{t}{\tau_1}}\right) + w_2\left(\frac{1}{\tau_2}e^{-\frac{t}{\tau_2}}\right) = w_1(R_1 + F)e^{-(R_1+F)t} + w_2R_2e^{-R_2t}$$

with weights of

$$w_1 = \frac{P_1(0)}{(P_1(0)+P_2(0))}\frac{1}{F+R_1}\left(R_1 + \frac{R_2F}{F+R_1-R_2}\right).$$

and

$w_2 = \frac{P_2(0)}{(P_1(0)+P_2(0))} + \frac{P_1(0)}{(P_1(0)+P_2(0))}\frac{F}{F+R_1-R_2}$.

The short lifetime displayed in the first panel of Fig. 4.10 fluctuates about a mean value of 19 ns, and it can be interpreted as the $\tau_1 = \frac{1}{(R_1+F)}$. The long lifetime in the third panel fluctuates about a mean value of 69 ns, and it can be interpreted as $\tau_2 = \frac{1}{R_2}$. The values of $\tau_1$ and $\tau_2$ alone do not give us information about $F$.

One wonders if our combined knowledge of the parameters from the bi-exponential fit can help us measure $F$. If we know the value of $R_1$, we will be able to solve for $F$ using only $\tau_1$. On the other hand, if we know the value of only $P_1(0)$, then we can solve for $P_2(0)$, $R_2$, $R_1$, and $F$ in terms of $w_1$, $w_2$, $\tau_1$, and $\tau_2$. Unfortunately, we do not know the values of $P_1(0)$ or $R_1$ in our experiment, they vary from QD to QD, so it will not be possible for us to extract $F$. The fluctuating $D_1$ and $D_2$ add even more complication to this problem. In an ideal world, we could systematically measure changes in $\tau_1$ as a function of the separation between the QDs, while maintaining all the other parameters ($R_1, P_1(0), D_1, R_2, P_2(0)$, and $D_2$), then a change in $\tau_1$ would indicate a change in $F$.

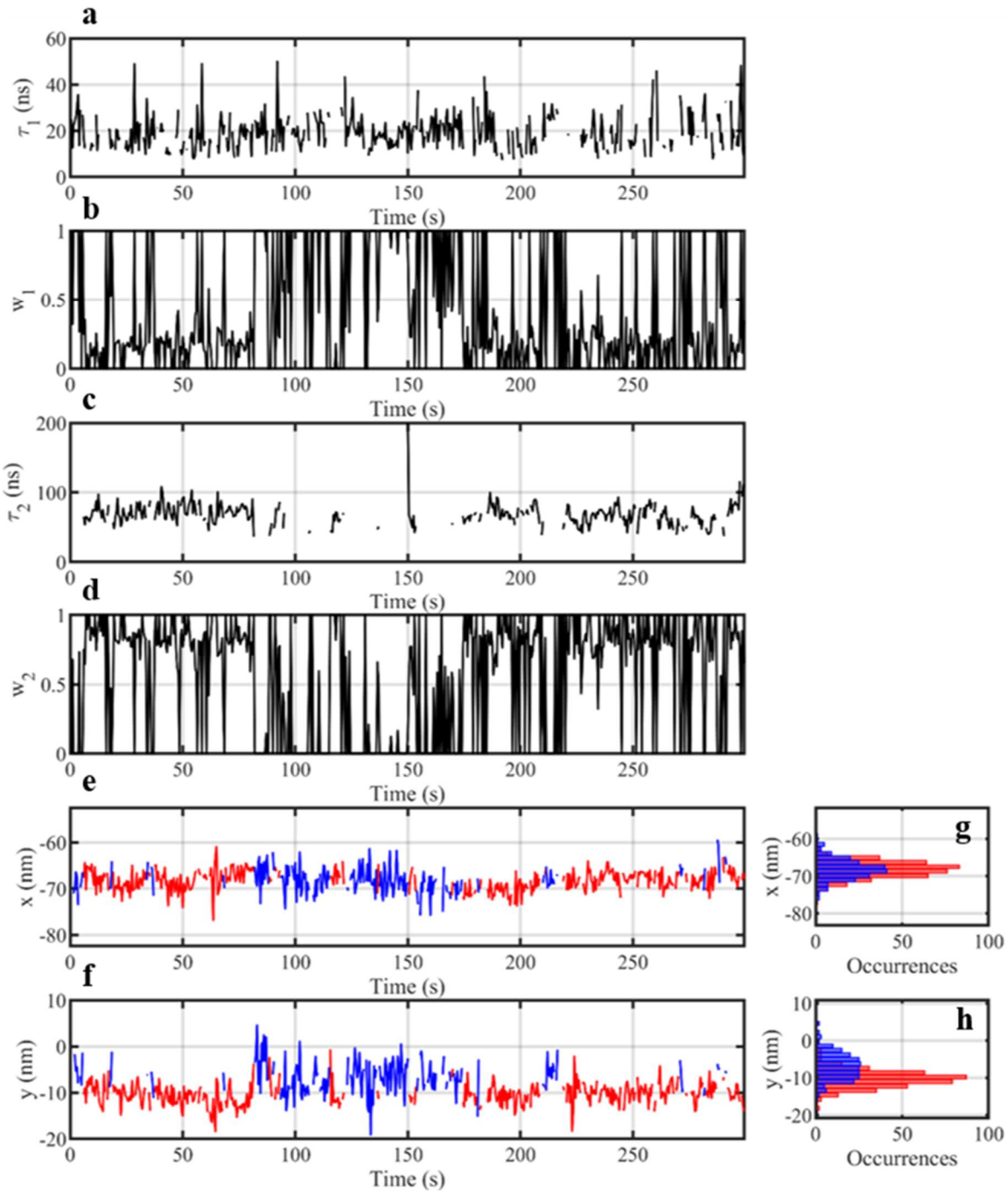


**Figure 4.10 Time-resolved super-resolution data from QD Pair-6.** Bi-exponential fits were performed for every 0.5 sec interval of 300 seconds of data for Pair-6 of the QDs shown in Fig. 4.1 to extract $\tau_1$, $w_1$, $\tau_2$, and $w_2$, which are plotted in a-d, respectively. The $x$ and $y$ positions of the emission centroid are plotted in (e) and (f). The pair was rotated so that the separation vector between the QDs was parallel to the y axis. The positions are color-coded blue for segments during which the weight of the short lifetime component was larger than the weight of the long lifetime component ($w_1 > w_2$), and visa-versa for the red-colored positions. Histograms of the $x$ and $y$

positions are plotted in g and h, respectively. The blue histograms were built from positions for which $w_1 > w_2$, and the red positions were built from positions for which $w_2 > w_1$.

## 4.5: Correlated Experiment Details

Different sample preparation and an additional wide-field imaging step was required for collecting correlated SR and SEM images. For the data presented in this chapter, the QDs were deposited on SEM grids that had 20 nm thick SiN windows. The SEM grids were silanized with (3-Aminopropyl) triethoxysilane (919-30-2) via vapor deposition prior to spin coating nanomolar concentrations of QDs and clustered QDs onto them. Each grid was placed face-down onto a glass coverslip as shown in Fig. 4.11a so that the immersion oil from the objectives used in optical imaging would not contaminate the sample. Next, it was imaged with a wide-field microscope previously described[49] (Fig. 4.11b) so the locations of the photoluminescent spots could be accurately referenced to a corner of the SEM window. The sample was then transferred to the time-resolved (TR) microscope where the photoluminescent spots were imaged one at a time. An image of the total counts recorded in the four detectors during an 80x80 um raster scan (as shown in Fig. 4.11c). One can see that the samples in the wide-field and TR setups were easily correlated, so we could assign accurate coordinates to the samples studied with the TR setup and then correlate those with SEM images[35]. Next, electron microscope images were collected on a FEI Magellan 400 SEM. An insertable STEM detector was used and the SEM was operated in STEM mode at 30 kV and 200 pA[36].

[35] We found the locations of the photoluminescent spots from the time-resolved images relative to the SEM window corners could be determined accurately, so one could, in principle, skip the wide-field imaging. However, both drift of the sample during the time it takes to raster scan the stage with the time-resolved setup and blinking of the QDs complicate this procedure, and it is convenient and reliable to acquire the wide field images for measuring the sample coordinates.

[36] SEM images were collected by Chris Sheehan at the Center for Integrated Nanotechnologies at Los Alamos National Laboratory

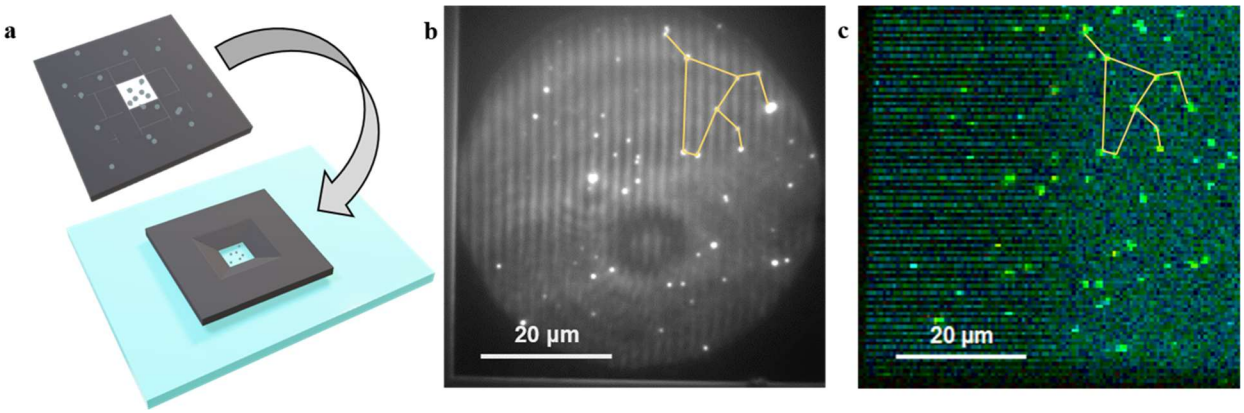


**Figure 4.11 Correlated SR and SEM imaging workflow**. (a) QDs were spin coated onto a SEM grid with 20 nm thick SiN windows which was placed face-down on glass coverslip. This prevented immersion oil from the objectives used in optical imaging from contaminating the sample. (b) The grid was imaged with a wide field microscope so the locations of the photoluminescent spots could be referenced to a corner of the window. In this image, the corner is faintly visible in the lower left. (c) A raster scan of the same window recorded with the TR setup, illustrating agreement between the two images.

Two rotations were important to note for accurately correlating the TR and SEM images: a 180 degree flip about the *y* axis (or *x* axis depending on how the coordinates of the grid are defined) because the grid had been inverted face-down onto the coverslip for TR imaging, and also the rotation of the grid relative to the axes of the TR image. As discussed in Section 3.3, the axes of the microscope stage are the same, apart from a small angle mismatch, as the axes defined for the image. However, we needed to account for the rotation of the SEM grid relative to the stage. To measure that, we captured an image as we raster scanned over a portion of the sample near the corner of the grid with an overhead lamp on. The contrast between light transmitting through the SEM window and being blocked by the frame of the grid allowed us to measure the rotation.

Though we examined QDs from the same synthesis batch as Chapter 2[37], we washed new solutions from QDs that were stored under nitrogen. The washing procedure and length of

[37] Pair-1 and Pair-2 were formed in a mixture of two different sizes of CdSe/CdS QDs. One was the same QDs that were studied in Chapter 2 (synthesis batch "SM152N2" that had a peak

exposure to air differed for these QDs compared to the ones in Chapter 2, so the ligand coverage and oxidation of the samples in this chapter differs from the previous one. Lastly, the clustering procedure differed slightly- we added non-solvent in lower quantities (10x lower) to a more concentrated (10x higher) solution of QDs. These changes may have impacted the behavior of singles and clusters, and they may be what caused the heterogeneity in lifetimes and intensities that was not present in Chapter 2, rather than the change in substrate. Additionally, we lowered the laser repetition rate from 5 to 2.5 MHz, and we lowered the average excitation power from 200 to 100 nW in this chapter compared to Chapter 2. The reason for this was that we eventually realized that the 5 MHz did not provide substantial time for the QDs to relax given that some QDs had contributions to their arrival time distributions with lifetimes approaching 100 ns. The decrease in excitation power allowed us to maintain the same energy per pulse with the slower frequency.

It is important to note (and we have mentioned this previously in the thesis) that the choice of the bin time can significantly alter the information that you glean from a dataset. When the time bin is too long, you risk averaging over important features in the data; when the time bin is too short, you lose precision, so important features in the data can become smeared together. We have found that any bin width greater than ~20 ms errs on the side of being too long (for these QDs under these excitation conditions), and we average over some features in the arrival time and counts[38]. However, a 0.5 s bin time is necessary for the data we collect on silicon membranes

emission wavelength of ~630 nm). The other had four monolayers of CdS shell deposited on a CdSe core that was about half the size (synthesis batch "SM1BN3" that had a peak emission wavelength of ~597 nm). Pairs 3-6 were clusters formed solely from SM152N2; all of the single QD measurements were done on SM152N2.

[38] One finds that with shorter bin times, the blinking behavior of the lifetime and intensity are more binary. The appearance of a continuum of intensity levels and lifetimes is partly an artifact of

because it allows for localization precision on the spatial scale of the QDs, which is important for capturing position dynamics in the QD clusters. With a shorter bin time, we would have too poor of localization precision to detect significant changes in the position on the necessary spatial scale.

averaging between these two difference states. We plan to return to this data and explore the information that we get by using shorter bin times.

# CHAPTER 5. Formulating a time-resolved likelihood distribution for superior localization capabilities

In Chapter 3 we constructed a likelihood distribution $\mathcal{L}_{CW}(X,Y;m_1,m_2,m_3,m_4)$ for the location (X,Y) of an emitter undergoing continuous wavelength (CW) excitation given the counts $m_1, m_1, m_3$, and $m_4$ detected in our four pixels after some interval of time (usually around 100 ms). Though some assumptions that underlie $\mathcal{L}_{CW}$ are obviously invalid for images collected with our TR microscope in which emitters undergo pulsed excitation, we used it to analyze our images for expediency because no distribution that assumed pulsed excitation was present in the literature. Our first published paper used $\mathcal{L}_{CW}$ to locate the emission centroids of single QDs and small clusters of QDs, though any affects of using a technically incorrect distribution to analyze our data were not clear at the time. Several groups like ourselves have reported on locating emitters undergoing pulsed excitation, but they have either used least squares fitting to the PSF[57] or maximized $\mathcal{L}_{CW}$[51,93,94] – presumably because they also lacked a suitable alternative.

During the spring of 2020, we returned to and solved the problem of constructing a likelihood distribution appropriate for systems undergoing pulsed excitation. This chapter presents our formulation of the correctly likelihood distribution, which we will refer to as called $\mathcal{L}_{Pulsed}(X,Y;m_1,m_2,m_3,m_4)$, for finding the location of an emitter undergoing pulsed excitation. To our knowledge, this is the first formulation of a pulsed likelihood distribution for the location and the first *correct* application of MLE for locating emitters undergoing pulsed excitation[39].

[39] Spoiler alert: we find the accuracy and precision for locating emitters from the TR microscope appears ambivalent to the choice of $\mathcal{L}_{CW}$ versus $\mathcal{L}_{pulsed}$, despite the inconsistency of applying $\mathcal{L}_{CW}$

Soon after formulating $\mathcal{L}_{Pulsed}$, we realized that it could be extended to incorporate information about photon arrival times that are collected with our detection scheme. Including the arrival time information gives what we call the "time-resolved likelihood distribution" $\mathcal{L}_T(X, Y; m_1(t), m_2(t), m_3(t), m_4(t))$ for the emitter location, which depends on the arrival times *t* of the counts registered in each pixel relative to the pulsed excitation. We will first show how $\mathcal{L}_T$ is constructed, and then we will examine data that we have analyzed with $\mathcal{L}_T$. We will see that the photon arrival time information allows us to achieve superior localization precision.

We should point out that we are not the first group to exploit the arrival time information to improve localization capabilities. Some groups have used the arrival time information to process the data *after* locating the emitters. For example, higher resolution images have been produced by comparing the fluorescence decays recorded in pixel of an image to a model of the fluorescence decay, and then they remove data that disagrees with the model[94]. Others use the arrival time information to process the images before attempting to locate the emitters. This has been done primarily using photon arrival time pair correlations that can be computed from the single photon arrival times. They have been used to reconstruct images with reduced PSF sizes prior to locating emitters, which can provide better localization precision.[62,95–97]. The pair correlations have also been used to verify that only a single isolated emitter is present prior to locating it[65], and to identify segments of the photon stream where it is probable that more than one emitter is contributing to the signal; that data is removed prior to locating the single emitter[57]. Additionally, photon arrival times have been used to resolve emitters with disparate lifetimes[18,19,21,22,25]. Prior to locating the emission centroids in an image containing multiple

to pulsed data. We suspect that the two distributions become equivalent in the limit of a large number of detected counts, though this remains to be shown.

fluorophores, images can be split into multiple images based on the probability of contributions to the fluorescence decay from each emitter. Each image is analyzed separately so that the location found in each one corresponds to a different type of fluorophore[98,99]. The lifetime information can also be applied to filter data after the PSF locations have been retrieved in order to resolve emission centers with disparate lifetimes[51,70]. All these methods benefit from using the arrival time information to process the data either before or after the emitters have been located. Our method for locating emitters with $\mathcal{L}_T$ is distinct from these other approaches because it allows us to insert the arrival time information directly into the localization algorithm, circumventing any need for pre- or post-processing of the images.

The first two sections of this chapter deal with deriving the likelihood distributions; $\mathcal{L}_{Pulsed}$ is constructed in 5.1, and it is extended in 5.2 to generate $\mathcal{L}_T$. Readers interested in the bottom line may skip ahead to Section 5.3, where we use $\mathcal{L}_T$ to localize single emitters in simulated and experimental data. Here we show how inclusion of temporal information can provide better localization results for certain conditions. Section 5.4, is a repository for the information that is necessary to implement these pulsed likelihood distributions, including the particularly tricky business of how each of the parameters in the distributions are calculated. In Section 5.5, we describe our method for calculating and sorting the probabilities of different outcomes in the model that is used to make $\mathcal{L}_{Pulsed}$ and $\mathcal{L}_{CW}$. This is a lengthy but crucial calculation that must be carried out numerically to generate both $\mathcal{L}_{Pulsed}$ and $\mathcal{L}_{CW}$.

## 5.1: Formulating $\mathcal{L}_{pulsed}$: A probability distribution for emitters undergoing pulsed excitation

To formulate the time-resolved likelihood distribution $\mathcal{L}_{pulsed}(X, Y; N)$ for the location *(X,Y)* of a QD given a set of counts $m1, m2, m3, m4$ by four pixels after *N* pulses have arrived[40], we start by building a model that contains the probability of every possible set of outcomes for the system after a single laser pulse arrives. Contributions to the counts include photons emitted by the QD, detector dark counts, and background counts (which are treated separately from the dark counts for reasons that will become clear soon). Let us begin the formulation by considering contributions to the counts from the QD in the absence of background. First, we define the probability $\varepsilon$ that the QD emits a single photon after the arrival of a laser pulse. The probability that no photon is emitted is $1 - \varepsilon$, assuming there is zero probability that more than one photon is emitted by the QD after a single laser pulse excites it. (Implicit in here is another assumption that the system relaxes completely before the arrival of each subsequent pulse. Next, we introduce a probability $C_k(X, Y, x_k, y_k, \dots)$ that pixel k collects the emission[41]. This depends on the QD location and PSF, and the pixel's location $(x_k, y_k)$, dimensions, and collection efficiency of the detector. The probability that pixel k does not collect a photon is $1 - C_k$. For now, consider just one pixel. The emission and collection probabilities are independent, so each of the four terms generated by the expansion of their product,

$$\big(\varepsilon + (1 - \varepsilon)\big)\big(C_k + (1 - C_k)\big) = \varepsilon C_k + \varepsilon(1 - C_k) + (1 - \varepsilon)C_k + (1 - \varepsilon)(1 - C_k) \quad (5.1)$$

[40] This N has a different meaning than the one from Chapter 3. Here it is the number of pulses that have arrived during a designated time window whereas back then it referred to the number of photons striking the detection plane.

[41] $C_k$ equivalent to the area ratio $\frac{A_k}{A}$ that we defined and used in Section 3.1.

corresponds to the probability of a particular set of outcomes. In (1), the first term $\varepsilon C_k$ is the probability that a photon is emitted and detected in pixel k. The other three probability terms in (1) correspond to sets of outcomes where nothing was detected in pixel k. Their sum, $\varepsilon(1 - C_k) + (1 - \varepsilon)C_k + (1 - \varepsilon)(1 - C_k) = (1 - \varepsilon C_k)$, gives the total probability that no photon is detected in pixel k, either because nothing was emitted or because the emitted photon missed pixel k.

To consider a system with four pixels, we extend the argument by including the collection probabilities $C_1$, $C_2$, $C_3$, $C_4$ of each of the pixels, so the ten terms generated by the expansion of the product,

$$\big(\varepsilon + (1 - \varepsilon)\big)\big(C_1 + \cdots + C_4 + (1 - C_1 - \cdots - C_4)\big), \tag{5.2}$$

are the probabilities of every possible set of outcomes. The probability tree in Fig. 5.1 enumerates this 4-pixel system. Each outcome is described at a vertex of the tree, and the bold-face labels on each branch are the probability of each outcome that a particular branch leads to. A set of outcomes can be determined by following a single path through the tree, and the probability of a set of outcomes is the product of the probabilities that label the branches traveled on that path. For example, the probability that a QD photon is emitted and lands in pixel 4 is equal to $\varepsilon C_4$.

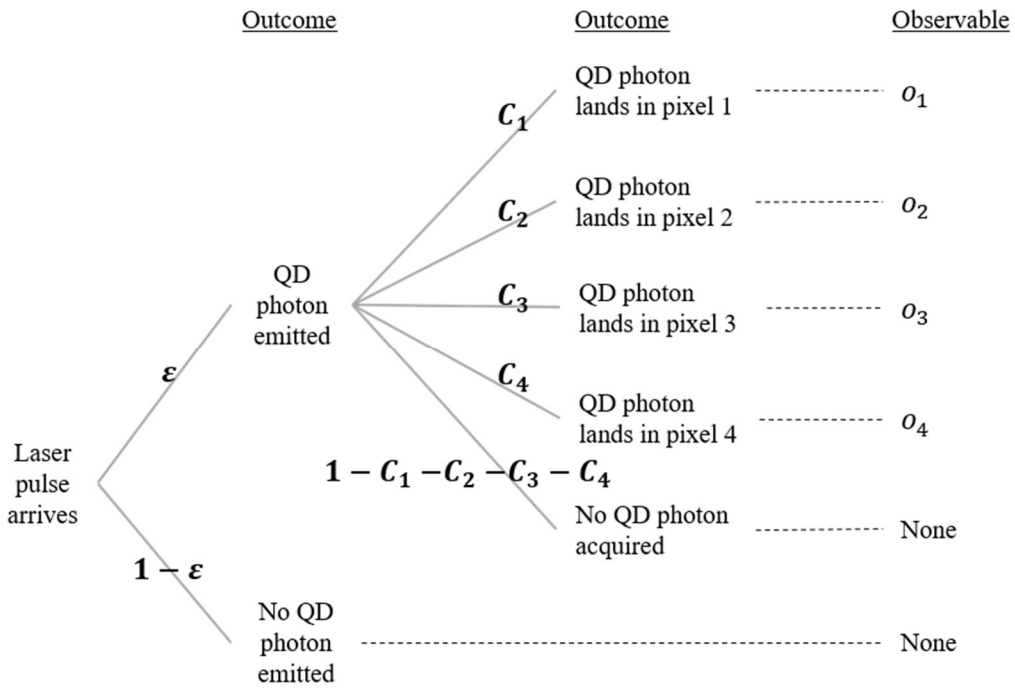


**Figure 5.1 Probability tree for collecting photons from a single emitter in four pixels.** This tree depicts all possible outcomes(vertices) for collecting photons from a single QD with four detectors. The probability of each outcome labels the branch that leads to it. Each outcome is described at a vertex, and the probability to arrive at each outcome is written on the branch that leads to it. A set of outcomes can be determined by following a single path through the tree, and the probability of that set of outcomes is equal to the product of the probabilities on each of the branches that are traveled on that path. We cannot distinguish between the different outcomes within our data, so we define observables $o_i$ that we can measure. For this system, there are four types of observables, $o_1, o_2, o_3$, and $o_4$ which are written in the column to the right of the tree.

Let's pause here and pretend that all outcomes of our system are described by the expansion of Eq. 5.2 Then, we are ready to write the likelihood distribution for the emitter location. We have some background that must be included later. To write the distribution for the emitter location, consider the probabilities of each set of events after N pulses have arrived, which is Eq. 5.2 raised to the Nth power. That can be written as a multinomial expansion. Each term in the multinomial is the probability of detecting a set of counts, $m_1, m_1, m_3$, and $m_4$, after N pulses have arrived,

$$P(m_1, m_2, m_3, m_4; N) = \varepsilon {C_2}^{m_2} \varepsilon {C_3}^{m_3} \varepsilon {C_4}^{m_4} \cdot (1 - \varepsilon C_1 - \varepsilon C_2 - \varepsilon C_3 - \varepsilon C_4)^{N - m_1 - m_2 - m_3 - m_4} \binom{N}{m_1, m_2, m_3, m_4} \tag{5.3}$$

If we keep track of how $P$ changes as we vary the values of X and Y that we expect for the emitter location (recall that X and Y enter the expression via the collection probabilities $C_k(X, Y)$ of the four pixels), we obtain a likelihood distribution for the emitter location given the set of detected counts after N pulses have arrived,

$$\mathcal{L}(X, Y; m_1, m_2, m_3, m_4, N) = \varepsilon {C_2}^{m_2} \varepsilon {C_3}^{m_3} \varepsilon {C_4}^{m_4} \cdot (1 - \varepsilon C_1 - \varepsilon C_2 - \varepsilon C_3 - \varepsilon C_4)^{N - m_1 - m_2 - m_3 - m_4} \cdot \binom{N}{m_1, m_2, m_3, m_4}. \tag{5.4}$$

The peak of $\mathcal{L}$ corresponds to the most likely location of the emitter. We could finish our discussion here if we decided to neglect the contributions of background[42], and this distribution would be the pulsed likelihood distribution $\mathcal{L}_{Pulsed}$ that we discussed in the introduction. Before introducing the background contributions, we need to do a little organizing, or else things are going to get very messy.

[42] Readers may be wondering what happens if we use the simple distribution in Eq. 5.4 to locate the emitter, and neglect to account for background in the system. We have explored this with simulations and the results are not devastating. The major harm arises in the accuracy of your localization if the emitter is not located at the origin. Without expecting background in a system that indeed has background, the emitter location is stretched away from the origin and its actual location. (Similarly, if one expects more background than what is actually present, an emitter will be pushed away from its actual location and toward the origin.) These shifts can be as small as 1% from the true location, or we have seen them as large as 40% (the shifts away from the correct location are proportional to how badly you have mis-estimated the background and also proportional to how far the emitter is from the origin).

As observers, we can only monitor arrivals (and nonarrivals) in the pixels, not the specific sets of outcomes, so it is important to sort the various sets of outcomes into observables that we are capable of recording in the experiment. For example, the tree in Fig. 5.1 distinguishes between the set of outcomes in which no QD photon is emitted and the set of outcomes in which a QD photon is emitted but not detected. However, both of those share the same null observable (nothing detected). For instances like these, which will be very common once the background is included, we need to a way of grouping multiple sets of outcomes that share the same observable. To do this, we define four observables: $\sigma_1$ indicates a count was detected in pixel 1, $\sigma_2$ indicates a count was detected in pixel 2 and so on for pixels 3 and 4. The observables corresponding to each set of outcomes are written in the column to the right of the tree in Fig. 5.1.

In addition to grouping the sets of outcomes into observables, we also group the probabilities of the sets of outcomes into "observable probabilities". For the system in Fig. 5.1, the probability of $\sigma_1$ is $\mathcal{P}_1$ and it is equal to $\varepsilon C_1$; the probability of $\sigma_2$ is $\mathcal{P}_2$ and it is equal to $\varepsilon C_2$; and so on for pixels 3 and 4. Now, the sum of the probabilities of all possible sets of outcomes (generated by expanding Eq. 5.2) can be written,

$$\mathcal{P}_1 + \mathcal{P}_2 + \mathcal{P}_3 + \mathcal{P}_4 + (1 - \mathcal{P}_1 - \mathcal{P}_2 - \mathcal{P}_3 - \mathcal{P}_4). \tag{5.5}$$

We can rewrite the likelihood distribution from Eq. 5.4 in terms of the observable probabilities,

$$\mathcal{L}(X, Y; m_1, m_2, m_3, m_4, N) = {\mathcal{P}_1}^{m_1}\,{\mathcal{P}_2}^{m_2}{\mathcal{P}_3}^{m_3}{\mathcal{P}_4}^{m_4}(1 - \mathcal{P}_1 - \mathcal{P}_2 - \mathcal{P}_3 - \mathcal{P}_4)^{N-m_1-m_2-m_3-m_4}\binom{N}{m_1, m_2, m_3, m_4}. \tag{5.6}$$

Reframing our system in terms of observables and observable probabilities like we did with this one will make our work more tractable for more complicated systems.

Other contributions to the counts aside from the QD emission include scattered laser excitation, fluorescence of the coverslip, and detector dark counts. The dark counts do not depend on the excitation, but arrive uniformly and randomly/uncorrelated in time, so we treat these separately from the excitation-dependent sources. We define the probability $\phi_{Dk}$ to register (and $1-\phi_{Dk}$ *not* to register) a dark count in pixel k. The other sources for background counts are caused by the arrival of the laser pulse, so we group them together and define the probability $B_k$ that pixel k receives (and $1-B_k$ that pixel k does not receive) a count from either the scattered excitation or coverslip fluorescence. We consider a system that contains QD emission, dark counts, and background counts by taking the product of these independent outcomes

$$\begin{aligned}&\big(\varepsilon+(1-\varepsilon)\big)\big(C_1+\cdots+C_4\\&+(1-C_1-\cdots-C_4)\big)\prod_{k=1}^{4}\big(B_k+(1-B_k)\big)\prod_{k=1}^{4}(\phi_{Dk}\\&+(1-\phi_{Dk})).\end{aligned}\tag{5.7}$$

The terms generated by the expansion of 5.7 correspond to the probabilities of every possible set of outcomes for our system.

The probability tree in Fig. 5.2 enumerates all possible sets of outcomes for the more complicated system described by Eq. 5.7. For simplicity, we exclude pixels 3 and 4 and the dark count contributions from the tree. Once again, a set of outcomes can be determined by following a single path through the tree, and the probability of a set of outcomes is the product of the probabilities that label the branches traveled on that path. For example, the probability to emit a photon, detect it with pixel 1, and receive no background counts in pixels 1 or 2 is equal to $\varepsilon C_1(1-B_1)(1-B_2)$. The observable corresponding to each set of outcomes is written in the column to the right of the tree. Because sources of counts can arrive from the QD, background, or

dark counts, it is possible to detect multiple counts in one or more pixels after a single laser pulse arrives, so we defined a new observable $m_>$ to keep track of sets of outcomes where there was more than one arrival. The definition of $\sigma_>$ is a bit nuanced[43]. In Fig. 5.2, there are 16 sets of outcomes that are sorted into three observables: $\sigma_1$, $\sigma_2$, and $\sigma_>$. The probabilities of those observables, respectively, are the observable probabilities $\mathcal{P}_1, \mathcal{P}_2$, and $\mathcal{P}_>$[44]. To compute them, we take the sum of the probabilities that result in the same observable. For example, four paths lead to $\sigma_1$, and the sum of their probabilities is $\mathcal{P}_1 = \varepsilon C_1 B_1 (1 - B_2) + \varepsilon C_1 (1 - B_1)(1 - B_2) + \varepsilon (1 - C_1) B_1 (1 - B_2) + (1 - \varepsilon) B_1 (1 - B_2)$.

For the full system that contains four pixels, the five observable probabilities, $\mathcal{P}_1, \mathcal{P}_2, \mathcal{P}_3, \mathcal{P}_4$, and $\mathcal{P}_>$ come from organizing and summing all 2,560 terms generated by the expansion of 5.7, so we can rewrite it as,

$$\mathcal{P}_1 + \mathcal{P}_2 + \mathcal{P}_3 + \mathcal{P}_4 + \mathcal{P}_> + (1 - \mathcal{P}_1 - \mathcal{P}_2 - \mathcal{P}_3 - \mathcal{P}_4 - \mathcal{P}_>). \tag{5.8}$$

Unlike the expansion and organization that could be done by hand for the system described by Eq 5.2, the expansion and organization of Eq. 5.7 into observable probabilities requires a more automated approach. Section 5.5 details this procedure, which involves generating a column matrix containing the probabilities of all possible outcome sets; each element is equal to the probability of a particular set of outcomes. In addition, a projection matrix made up of zeros and ones is

[43] Specifically, when two or more counts are registered in at least two different pixels, the set of outcomes is assigned the observable $\sigma_>$. When two or more counts are registered in a single pixel k, the set of outcomes is *not* assigned $\sigma_>$, but is instead assigned $\sigma_k$. This has to do with accommodating electronic effects called "lock-out" in our detectors, and we'll discuss it in more detail later in the chapter.

[44] The observable probability of a single observable is equal to the sum of the probabilities of all possible sets of outcomes that result in that observable.

generated for each observable type. The product of the transpose of the probability matrix and a specific projection matrix gives its corresponding observable probability.

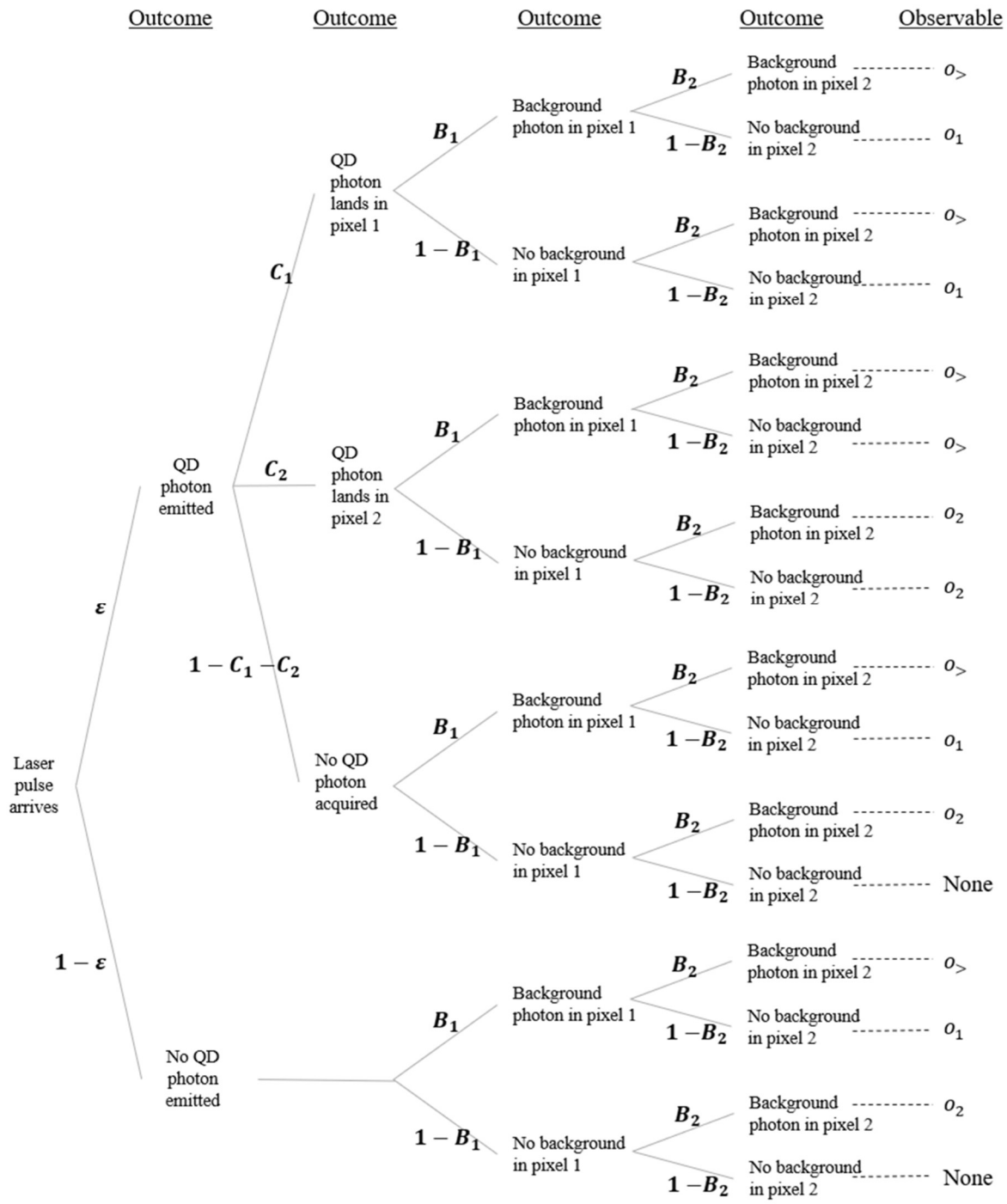


**Figure 5.2 Probability tree for collecting photons from a single emitter and background counts in two pixels.** This tree illustrates all possible outcomes when collecting photons from a single QD and background in two detectors. Each outcome is described at a vertex, and the

probability to arrive at each outcome is written on the branch that leads to it. A set of outcomes can be determined by following a single path through the tree, and the probability of that set of outcomes is equal to the product of the probabilities on each of the branches that are traveled on that path. For this system, there are three types of observables, $o_1$, $o_2$, and $o_>$ to which the outcomes can be assigned, and these are written in the column to the right of the tree.

Now that we have finished defining a probability model that incorporates all the major sources for counts in our experiment, we are ready to construct $\mathcal{L}_{pulsed}$. Like previous likelihood distribution constructions, we first consider the probabilities of all possible observables for the system after N pulses have arrived by raising the sum of the observable probabilities (Eq. 5.8) to the Nth power, and then we express this as a multinomial expansion. A single term in the multinomial is equal to the probability to collect a set of counts, $\{m_i\}$=$(m_1, m_2, m_2, m_4, m_>)$ after N pulses have arrived. The likelihood distribution for the emitter location can then be written as

$$\mathcal{L}_{pulsed}(X, Y; \{m_i\}, N) = {\mathcal{P}_1}^{m_1}\,{\mathcal{P}_2}^{m_2}\mathcal{P}_3{}^{m_3}{\mathcal{P}_4}^{m_4}{\mathcal{P}_>}^{m_>} \cdot (1 - \mathcal{P}_1 - \mathcal{P}_2 - \mathcal{P}_3 - \mathcal{P}_4 - \mathcal{P}_>)^{N-m_1-m_2-m_3-m_4-m_>} \binom{N}{m_1, m_2,\ m_3, m_4, m_>}. \tag{5.9}$$

The maximum of $\mathcal{L}_{pulsed}$ corresponds to the most likely location for an emitter excited by the pulsed excitation in the presence of fluorescent background and detector dark counts. While we could finish our discussion here and use Eq. 5.9 to analyze our data, we will instead push ahead to get the likelihood distribution $\mathcal{L}_T$ that incorporates the photon arrival time information. We will see that $\mathcal{L}_T$ will allow us to get better localization precision than $\mathcal{L}_{pulsed}$ for certain conditions. If for some reason we do not want to use (or we cannot/do not collect) the temporal information, we can still use $\mathcal{L}_T$ to locate the emitter, and there is a parameter that we can easily toggle to remove the time-dependence of the distribution.

## 5.2: Formulating $\mathcal{L}_T$: A probability distribution that accounts for photon arrival time distributions

With time-correlated single photon counting data, we record not only the arrival times of each count relative to the start of the experiment (which allows to compute $m_1, m_2, m_2$, $m_4$, $m_>$ for each set of N pulses that excites the system), but we also collect the time it takes for each count to arrive relative to the most recent laser pulse. The most expedient way to include that information in our model is to distinguish between photons that arrived before or after one designated time $t_c$ between the time t=0 when each laser pulse arrives, and the time t=*T* when a subsequent laser pulse arrives. One can utilize the temporal information more fully by segregating the arrivals more than two time windows - there are some advantages to that which we will speculate about later - but we have not done that yet and only work with two time windows. To distinguish between counts arriving in the time window "a", between 0 and $t_c$, and the time window "b", between $t_c$ and T, we define more observables. The observables $\sigma_{1a}$, $\sigma_{2a}$, $\sigma_{3a}$, and $\sigma_{4a}$ denote arrivals that occur in time window *a* for each of the pixels; the observables $\sigma_{1b}$, $\sigma_{2b}$, $\sigma_{3b}$, and $\sigma_{4b}$ denote arrivals that occur in time window b for each of the pixels.

Now we must determine the probability of those observables given the distributions of arrival times from the emitted photons, background counts, and detector dark counts. To that end, we introduce a probability $\phi_\varepsilon$ that a photon from the QD is emitted during the time window *a*, which is between t = 0 and t= $t_c$. The lifetime of the emitters that we study (~30-80 ns) are much shorter than T, so the probability that a photon is emitted in a time window *b* between $t_c$ and *T,* is approximately $1 - \phi_\varepsilon$. In theory, $\phi_\varepsilon$ can be obtained by integrating the normalized decay function for the emitter from zero to $t_c$. However, it is more convenient (and accurate) to obtain $\phi_\varepsilon$ by

integrating directly over the measured (or simulated) photon arrival distribution so that we can accommodate for a fluorescence lifetime that often fluctuates over the duration of the experiment for QDs, and to accommodate for effects of the instrument response function. Details of this measurement are provided in Section 5.4. Fig. 5.3a displays the photon arrival distribution for a single QD, and the shaded blue area is equal to $\phi_\varepsilon$.

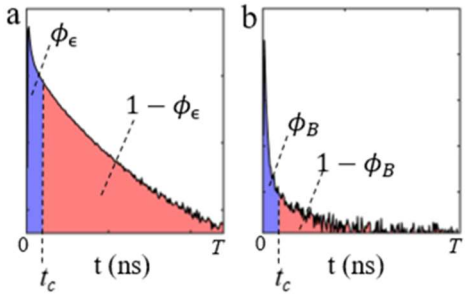


**Figure 5.3 Determining the probabilities of emitter and background photon arrival times.** (a) A normalized histogram of the arrival times from photons emitted by the QD is created from data of a single QD after subtracting the contribution from background fluorescence and detector dark counts. The histogram is split into two periods based on whether photons arrive before (blue) or after (red) $t_c$. The probability that a single photon is emitted between time zero when the pulse arrives and time $t_c$ is $\phi_\varepsilon$ and the probability a photon is emitted between $t_c$ and $T$ is 1-$\phi_\varepsilon$. (b) A normalized histogram of the arrival times of background photons is also spit in two segments. The probability that a single background photon is emitted between zero and $t_c$ is $\phi_B$ and the probability that a single background photon is emitted between $t_c$ and $T$ is 1-$\phi_B$.

In tandem, we introduce the probability $\phi_B$ of a background photon being emitted in time window *a.* This is equal the area underneath the normalized photoluminescence decay from recorded background emission between 0 and $t_c$. Fig. 5.3b displays the normalized distribution of background fluorescence recorded experimentally and $\phi_B$ which is the shaded blue area. Once again, the lifetime of the background fluorescence (~2 ns for our experiments) is much shorter than $T$, so the probability of a background photon arriving in time window $b$ is $1-\phi_B$, which is equal to the shaded red area in Fig. 5.3b. Lastly, we consider the arrival times of the dark counts. Recall that we previously defined $\phi_{Dk}$ as the probability to detect a dark count in pixel k between 0 and $T$. Now we rewrite that $\phi_{Dk}$ as the sum $\phi_{Dka}+\phi_{Dkb}$ of the probability to detect a dark count

in pixel k during time window *a,* and the probability to detect a dark count in pixel k during time window *b*. It follows that the probability of detecting no dark count during *T* is $(1-\phi_{Dka}-\phi_{Dkb})$. More details on how to compute $\phi_\varepsilon, \phi_B, \{\phi_{Dka}\}$, and $\{\phi_{Dkb}\}$ are provided in Section 5.4.

Incorporating the various arrival time probabilities for the QD, background, and dark counts into the model, we can write the probabilities of all possible sets of outcomes for the system after a single laser pulse arrives, which are equal to the 51,840 terms generated in the expansion of the product,

$$\begin{aligned}\big(\varepsilon+(1-\varepsilon)\big)\big(C_1+\cdots+C_4+(1-C_1-\cdots-C_4)\big)\big(\phi_\varepsilon+(1-\phi_\varepsilon)\big)\big(\phi_B \\ +(1-\phi_B)\big)\prod_{k=1}^{4}\big(B_k+(1-B_k)\big)\prod_{k=1}^{4}(\phi_{Dka}+\phi_{Dkb} \\ +(1-\phi_{Dka}-\phi_{Dkb})\big).\end{aligned} \tag{5.10}$$

Each term corresponds to the probability of achieving a particular observable $\sigma_i$, where *i = 1a, 2a, 3a, 4a, 1b, 2b, 3b, 4b, >,* and we sort the 51,840 terms into nine corresponding observable probabilities $\mathcal{P}_i(\varepsilon,\{C_k\},\{B_k\},\phi_\varepsilon,\phi_B,\{\phi_{Dka}\},\{\phi_{Dkb}\})$, where *i = 1a,2a,3a,4a,1b,2b,3b,4b,>* for this system. That procedure is detailed in 3.8. Now we can express (3.1.7a) as a sum of the nine observable probabilities,

$$\mathcal{P}_{1a}+\mathcal{P}_{2a}+\mathcal{P}_{3a}+\mathcal{P}_{4a}+\mathcal{P}_{1b}+\mathcal{P}_{2b}+\mathcal{P}_{3b}+\mathcal{P}_{4b}+\mathcal{P}_{>}+(1-\mathcal{P}_{1a}-\cdots). \tag{5.11}$$

Notice that we do not keep track of the photon arrival time distributions for the multi-arrival events. These constitute <1% of our data, so there is little information to gain by sorting of the arrival times of each count in the multi-arrival event (plus it makes our work much harder by adding additional observables!!).

To consider the system after *N* pulses have arrived, we raise Eq. 5.11 to the $N^{th}$ power and write it as a multinomial expansion. The probability $P(\{m_i\}; N, \{\mathcal{P}_i\})$ to observe a set of counts $\{m_i\}$ after *N* pulses is a coefficient of the multinomial expansion. Recall that the information about the emitter location *(X,Y)* is contained in the collection probabilities $\{C_k\}$ which make up the observable probabilities $\{\mathcal{P}_i\}$ . At this point, it is simply a matter of reversing the independent and dependent variables of $P(\{m_i\}; N, \{\mathcal{P}_i\})$ to define the time-resolved likelihood distribution,

$$\mathcal{L}_T(X, Y; \{m_i\}, N, \{\mathcal{P}_i\}) \tag{5.12}$$

$$= \left(\prod_i {\mathcal{P}_i}^{m_i}\right)\left(1 - \sum_i \mathcal{P}_i\right)^{N-\sum_i m_i} \binom{N}{m_>, m_{1a}, m_{1b}, m_{2a}, m_{2b}, \ldots}.$$

For every set of N pulses (typically 2.5e5 pulses), we use the downhill simplex method[83] to identify the maximum of the $\ln(\mathcal{L}_T)$ in two dimensions. The values of $(X, Y)$ that maximize $\ln(\mathcal{L}_T)$ correspond to the most likely location $(X_{max}, Y_{max})$ of the emitter during the time those N pulses arrived[45].

We are quite excited to be using Eq. 5.12 for the centroid estimation, because it feels as if we are truly conducting time-resolved super-resolution microscopy for the first time. Finding the locations based only on the counts $m_1, m_2, m_2$, $m_4$, $m_>$, and then associated a lifetime with that centroid after the fact (which is essentially what we did in Chapter 3) does not make full use of the time information. While MLE with $\mathcal{L}_T$ performs well for single emitters, as will be shown in the next two sections, the fantastic thing about it is that we can use it to identify the locations of two

[45] If for some reason you don't want to use the arrival time information (or perhaps you have pulsed excitation, but did not collect the arrival times relative to each laser pulse), you can let $t_c$ =0. In that limit, $\mathcal{L}_T$=$\mathcal{L}_{pulsed}$.

emission centroids (ergo resolve two nonblinking emitters!) provided they have disparate lifetimes. That is the subject of Chapter 6.

## 5.3: Localizing single emitters in simulated and experimental data with $\mathcal{L}_T$

In order to test out our algorithm, we simulated data of a point emitter in the presence of background and detector dark counts. The data was constructed similar to probability model described in Section 5.2, so a simulated system was excited with some number of pulses N, and for each pulse we determined if a photon arrived, in which pixel it arrived, and when it arrived. After N pulses, the simulated counts were binned into $\{m_i\}$, where *i = 1a, 2a, 3a, 4a, 1b, 2b, 3b, 4b,* and >, and ln ($\mathcal{L}_T$) was maximized to determine the most likely emitter location. To generate data, we input values for the following probabilities that were defined earlier: $\varepsilon, \{B_k\}, \phi_\varepsilon, \phi_B$, and $\{\phi_{Dka}\}$. Systematically varying these input probabilities gave us a chance to explore the accuracy and precision of our localization method (i.e., MLE with $\mathcal{L}_T$ ) for different conditions. The localization precision $\sigma = \sqrt{\sigma_X{}^2 + \sigma_Y{}^2}$ was determined by repeating each simulation 100 times and computing the standard deviation of the X and Y locations found for the simulations.

The extent to which the arrival time information is exploited depends on the selection of $t_c$ so we analyzed simulated data with various values of $t_c$ to explore how its value impacted the localization precision. Fig. 5.4a displays $\sigma$ versus $t_c$. Each point on the figure is measured from the standard deviation of 100 locations found for an emitter with a lifetime of 30 ns in the presence of a 2 ns lifetime background and detector dark count levels that mimicked experimental values. Because the temporal distributions of the background and emitter are different, we expect $\mathcal{L}_T$ will allow us to localize the emitter with superior precision, provided that we have a reasonable

selection of $t_c$. For these simulations, the precision is at its worst, $\sigma \approx 12$ nm for $t_c = 0$, because the time information is not being utilized in the analysis; for $t_c = 0$ the probability of an emitter arrival $\phi_\varepsilon$ and background arrival $\phi_B$ are equivalent (both are equal to zero)[46]. The same is true when $t_c = T$. Both of these limiting cases are equivalent to analyzing the data with MLE using $\mathcal{L}_{pulsed}$. The optimal selection of $t_c$ was ~10 ns for which $\sigma$ was minimized at $\sigma \approx 4$ nm. For this selection of $t_c$, the values of $\phi_\varepsilon$ and $\phi_B$ were most disparate, and $\mathcal{L}_T$ took advantage of that information.

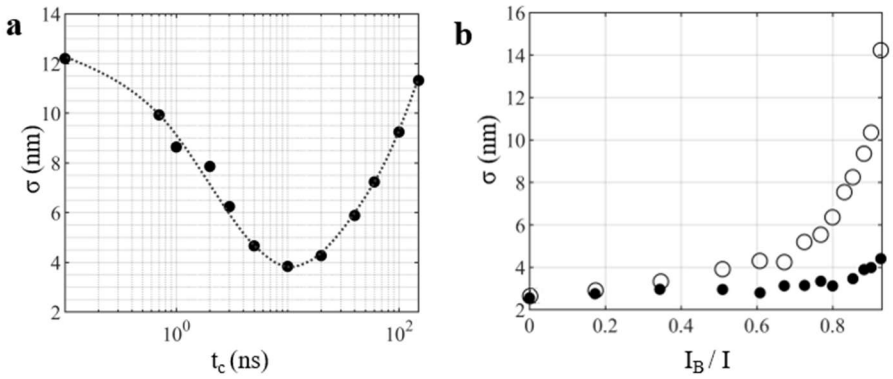


**Figure 5.4 The localization precision σ is improved with time-resolved imaging.** (a) The selection of $t_c$ impacts σ of the emitter. Each point on the plot is the standard deviation $\sigma = \sqrt{{\sigma_X}^2+{\sigma_Y}^2}$ of 100 locations determined from 100 sets of counts generated by a simulated system that contains a single emitter in the presence of fluorescence background and detector dark counts. Without time filtering ($t_w \approx 0$), σ is ~12 nm, whereas with time filtering and selecting the optimal value of 10 ns for $t_w$, σ is ~4 nm. (b) σ depends exponentially on the ratio of $I_B$ / $I$ of background counts to total counts; it is computed from analyzing simulated data for various levels of background signal while maintaining the same emitter and dark count behavior that was described in (a) for each simulation. The precision rises slower with time-resolved imaging ($t_c$ = 10 ns),

[46] Caveat: the improvement in precision with the arrival time information was only achieved for levels of background counts that far exceed the levels recorded in experiments of single QDs on a glass coverslip. In typical experiments where $T$ = 200 ns and $N$ = 5e5 pulses, ~50 counts/$N$ of background was recorded in each pixel. The results in Fig. 5.4a were achieved with an artificially enhanced background in which ~2,400 counts/N of background was recorded in each pixel.

plotted filled circles, than without time-resolved imaging ($t_c \approx 0$ ns), hollow circles, which shows that the time-resolved imaging improves the localization capabilities in high background systems.

To explore the impact of background counts on the localization precision, we simulated data with the probability of background counts in each pixel $\{B_k\}$ ranging between zero to 50 times the experimentally measured values for $\{B_k\}$. The lifetime of the background and emitter were 2 ns and 30 ns, respectively, the same as the previous simulation. Each simulation was repeated 100 times and the locations were determined twice: once with MLE using $\mathcal{L}_T$ and a selection $t_c$ =0 ns, and once with MLE using $\mathcal{L}_T$ and a selection $t_c$ = 10 ns. The localization precision was determined from the standard deviation of the 100 locations for each level of background for both the $t_c$ =0 and $t_c$ =10 locations. These are plotted in Fig. 5.4b as a function of the ratio $I_B/I$ of background counts to total signal. For the 10 ns selection (filled markers), the precision worsens slightly as $I_B/I$ increased. In contrast, the precision rapidly deteriorates as $I_B/I$ increases if the temporal information is not included in the analysis. The empty markers in Fig. 5.4b display $\sigma$ for repeated simulations with a selection for $t_c$ of 0 ns, for which $\phi_\varepsilon$ and $\phi_B$ are equivalent so no temporal information is included in $\mathcal{L}_T$. For lower levels of background where $I_B/I$ < ~0.4, there is no significant difference between the precision achieved with or without the temporal information (filled versus empty markers). For higher levels of background where $I_B/I$ >0.4, there were 2- to 3-fold improvements in the localization precision because the disparity in the lifetimes of the background and emitter prevented the background from dominating our information about the emitter location in $\mathcal{L}_T$[47].

[47]Some readers might incorrectly equate MLE using $\mathcal{L}_T$ with MLE using $\mathcal{L}_{\text{pulsed}}$ on data that has been filtered with something called "time-gating"[65,107–111] because both methods take advantage of disparate lifetimes between the emission of interest and the background. For time-gating, photon arrivals within a certain time window between 0 and T are discarded whereas they

While we simulated a system of high background counts with a shorter lifetime than the emitter because that agreed with our experimental data, we also explored cases where the background has a longer lifetime that approaches the emitter lifetime, or cases where the probability of detector dark counts approach the probability of emitted photons. In any of these scenarios (provided the temporal distributions of the emitter versus the background and dark counts are different and that we choose a reasonable value for $t_c$), we observe improvements by doing MLE with $\mathcal{L}_T$.

From experimental data, the location of the QD was repeatedly determined every 0.1 sec for 60 sec of data by maximizing $\ln(\mathcal{L}_T)$. The X and Y values that gave the maximum for each 0.1 s are plotted in Fig. 5.5 and the localization precision was determined from their spread. In this case, the precision is ±3 nm in x and y, for which the total counts per 0.1s, $\sum m_i$, was ~15,000. The precision follows the central limit theorem and improves with longer time bins at the expense of capturing shorter timescale dynamics that may occur in the system. We selected 0.1 seconds as a balance between these competing interests. These locations were determined for $t_c$ = 10 ns, because that selection gave the optimal precision for simulated data of an emitter and background with lifetimes similar to this data (Fig. 5.4a). However, the selection of $t_c$ for analyzing this data is arbitrary because the background contribution is relatively low. We would like to point out that this is the first time a single emitter undergoing pulsed excitation has been located using a likelihood distribution that accounts for the pulsed excitation.

---

are not discarded for MLE using $\mathcal{L}_T$. However, the improvements in precision for the high background simulation using $\mathcal{L}_T$ may be identical if $\mathcal{L}_{\text{pulsed}}$ was used on time-gated data. This will not be the case for data in which the background and emitter lifetimes are similar. In cases like these, the time-gated method will be of no use (and may worsen the precision) whereas MLE with $\mathcal{L}_T$ will either maintain the optimal precision or yield improvements.

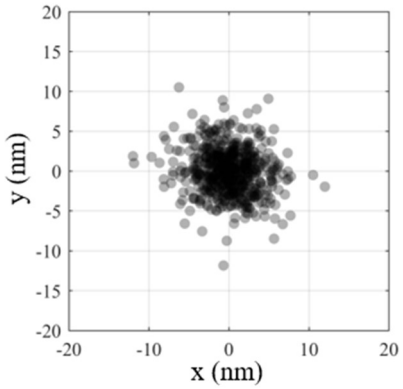


**Figure 5.5 Single QD localized with the time-resolved likelihood distribution $\mathcal{L}_\mathrm{T}$.** A graph of the x and y locations for a single QD determined every 0.1 sec for 60 sec total. These are determined by maximizing ln ($\mathcal{L}_\mathrm{T}$) (Eqn. 5.12). Drift of the emitter in x and y is significant during this interval, and it is corrected with a linear fit before the locations are plotted.

While the application of $\mathcal{L}_T$ may give the same precision and accuracy as the application of $\mathcal{L}_{CW}$ to experimental data acquired with pulsed excitation, it is still useful for the single molecule localization community to know that an analysis method exists to correctly accommodate pulsed excitation. Moreover, the next chapter extends the formulation so that we can take advantage of the temporal information and locate multiple nonblinking emitters, provided they have disparate lifetimes. This achievement is only made possible by the work done in this chapter.

## 5.4: Measuring parameters for $\mathcal{L}_T$

The signal is made up of arrival times from the QD, scattered excitation, coverslip fluorescence, and detector dark counts. $\mathcal{L}_T$ depends on parameters pertaining to each of those that we must determine from a few independent measurements aside from the four-pixel image of the QD emission. First, consider the parameters that we need related to the detector dark counts, which are uniformly distributed in time and arrive with a rate $R_{Dk}$ that is different for each of the four pixels, k = 1,2,3,4. $R_{Dk}$ is ~500 counts/sec in each pixel. For the MLE, we must know the probability $\phi_{Dka} = \int_0^{t_c} R_{Dk} e^{-R_{Dk}t} = R_{Dk} t_c$ to detect a dark count between time 0 and $\mathrm{t_c}$ in pixel

k, and the probability $\phi_{Dkb} = \int_{t_c}^{T} R_{Dk} e^{-R_{Dk}t} = R_{Dk}(T - t_c)$ to detect a dark count between time $t_c$ and $T$ (the laser pulse period and time at which the clock resets to zero) in pixel k. To measure $R_{Dk}$ in each pixel, we take the average of detected counts in each pixel for 60 s of data while the laser is blocked. We have found it is constant throughout a day's experiments if the detectors are left on, and we measure it each time we turn on the detectors.

Next, consider background contributions from scattered excitation and coverslip fluorescence. We must quantify the probabilities $B_1$, $B_2$, $B_3$, and $B_4$ to detect a background count in each of the pixels and the probability $\phi_B$ to detect a background photon between 0 and $t_c$. We distinguish these background contributions from the dark counts because they have a different distribution in time - they usually have a lifetime of ~ 3 ns, and their levels depend on the excitation power. They contribute between zero and 2,000 counts/second/detector depending on the substrate and excitation power. Their levels do not change with time, but they depend on the z position of the objective relative to the substrate. We measure them once for each substrate by collecting counts $\{m_k\}$ from the surface for ~60 seconds without a QD in the field of view. We measure them after determining the optimal z position for collecting signal from QDs on the surface of the coverslip. If the z position is altered, it is (usually) necessary to re-measure the background. For glass coverslips, we found the background is constant across the surface of the coverslip, and nearly identical from coverslip to coverslip. We assume in our analysis that the probability $\phi_B$ to detect a photon between 0 and $t_c$ is identical for the four detectors (Actually, this probability can vary slightly <1% among the four detectors because they are mis-aligned in time, or because they each have different IRFs.) To determine $\phi_B$, we subtract a scaled[48] histogram of the dark count

[48] The histogram must be scaled if the acquisition time of the background measurement and dark count measurement are not equal. To scale them, we divide each histogram by the total acquisition

arrival times from a scaled histogram of the total background . The sum of the bins from zero to $t_c$ is equal to $\phi_B$. The likelihood distribution also requires knowledge of the probability to detect a background count between $t_c$ and T, and we assume it is equal to $1-\phi_B$ because the lifetime of the background is much shorter than T. To determine $B_1$, $B_2$, $B_3$, and $B_4$, we maximize a likelihood distribution $\mathcal{L}(\{B_k\};N,\{m_i\}) = (\prod_i \mathcal{P}_i{}^{m_i})(1-\sum_i \mathcal{P}_i)^{N-\sum_i m_i}\binom{N}{m_>, m_1, m_2, \ldots}$ that depends on the observable probabilities $\mathcal{P}_i(\{B_k\},\{R_{Dk}\})$, where *i=1,2,3,4,* and >. To get the observable probabilities, we must organize the terms generated by the expansion of $\sum_{k=1}^{4}\big(B_k+(1-B_k)\big)\big(\phi_{Dk}+(1-\phi_{Dk})\big)$. This can be done using the matrix algebra procedure described in Section 5.5.

The probability $\phi_\varepsilon$ that a QD emits a photon between 0 and $t_c$ must also be determined in order to localize an emitter. It fluctuates over the course of a measurement, and we must determine it for each time over which we bin the photons to get a location. To measure it, we subtract a scaled[49] histogram of the background and dark counts arrivals from a scaled histogram of the total arrivals that occur during a particular time bin, and then normalize that histogram. The sum of the bins from zero to $t_c$ is equal to $\phi_\varepsilon$. This conveniently requires no fitting of the arrival time distributions, so the method does not require us to assign a particular model to the data based on our fitting parameters.

time for their respective measurements. This way, both the histograms become the histograms of arrivals per second and can then be subtracted.

[49] Once again, the histogram must be scaled if the bin time for the QD emission and the background measurement time are not equal. To scale them, we divide the QD histogram by the bin time, and we divide the background histogram by the total acquisition time for its measurement. This way, both the histograms become the histograms of arrivals per second and can then be subtracted.

There are temporal discrepancies among the four channels that are caused by differences in cable length and other electronics, which means that t=0 is not identical for all four pixels. We use delays in the software to synchronize the signals, but it is impossible to align them perfectly in time. To account for these discrepancies, we could introduce probabilities of photon arrival times that are unique for each detector $\{\phi_{\varepsilon k}\}$ and probabilities of background arrival times that are unique for each detector $\{\phi_{Bk}\}$. However, we have adjusted the delays of the channels relative to one another for simulated data, and found that higher temporal discrepancies (>1 ns) than what we have (<0.1 ns) would be necessary to significantly impact the localization outcomes.

Detector dead time refers to an effect in which we cannot register multiple events on a single detector within ~50 ns of one another. After the dead time has passed, we can register another event on that detector. This means that there is a small but finite probability of detecting two events on a single detector within a single laser pulse period of our experiments, which have either 200 or 400 ns periods. However, in our formulation of the likelihood, we stipulated that there was zero probability of detecting more than one event on a single pixel during a single period. To make the model agree with the data, we find it simpler in this case to manipulate the data rather than the model. We do this by discarding all secondary, tertiary, etc. arrivals that occur in one pixel during a single laser pulse period from our data. In this way, the model more accurately describes the data. A perfect accommodation for the dead time would go one step further and account for dead time that carries over into the next laser pulse period. For example, if a photon arrives at t = 390 ns, and the clock resets to zero at t = 400 ns, it will be impossible to detect another event in that pixel until 50 ns later when t>40 ns. We neglected to account for this. However, it is not a major concern because we know that set of outcomes does not occur frequently for our system in which the lifetimes of the background and emitter are much shorter than *T*.

The PSF widths, $w_x$ and $w_y$, are measured once per coverslip after the z position is optimized and locked. To extract them, we move a QD by known distances (±50 nm in x and y) with the piezoelectric stage and then solve for the $w_x$ and $w_y$ of an assumed 2D Gaussian PSF that accurately recover the changes in distance in both x and y. We typically measured $w_x \approx w_y \approx$ 150 nm for a QD in focus. We find that the PSF size does not change significantly when we repeatedly measure it with QDs located in different places on the coverslip, regardless of manual adjustments to stage position, provided the z position is locked. Here we have a 250x magnification of the PSF image which results in a PSF that is ~80 um FWHM that is collected by the 100 um optical fiber apertures. The measurement procedure is described in more detail in Chapter 3.

To determine the probability $C_k$ to collect a photon from the QD in pixel k, we take the integral of the PSF over the cross-sectional area of the optical fiber aperture, and we multiply that by the relative detector efficiency $\eta_k$ for each pixel. See Eqns. 3.12-3.14 for details.

In the initial versions of our analysis, we let the emission probability $\varepsilon$ be a floating parameter that was determined along with the location. $\varepsilon$ varies with the changing emissivity of the QD during the duration (~1-10 min) of an experiment (presumably due to processes such as temporarily trapped charges that change the relaxation pathways). For every set of *N* pulses (typically 2.5e5 pulses), we identified the maximum of the ln $(\mathcal{L}_T)$ in three dimensions. The values of $(X, Y, \varepsilon)$ that maximize ln $(\mathcal{L}_T)$ correspond to the most likely location $(X_{max}, Y_{max})$ of the emitter and the most likely emission probability $\varepsilon_{max}$ during the time those *N* pulses arrived[50]. We later found a faster alternative by solving for $\varepsilon$ in terms of the counts received from the emitter and

[50] If for some reason you don't want to use the arrival time information (or perhaps you have a pulsed system, but you did not collect the arrival times relative to each laser pulse), you can let $t_c$ =0. In that limit, $\mathcal{L}_T$=$\mathcal{L}_{pulsed}$.

the probability to receive those counts. To solve for $\varepsilon$, consider the sum of photons from the QD that have arrived in every pixel before $\mathrm{t_c}$ divided by the number of pulses *N* that have arrived,

$$A_a = \frac{\mathfrak{m}_{1a} + \mathfrak{m}_{2a} + \mathfrak{m}_{3a} + \mathfrak{m}_{4a}}{N} = \varepsilon\phi_\varepsilon \sum_{k=1}^{4} C_k, \tag{5.13}$$

which is equal to the probabilities to detect a count in one of the pixels during time window a after one pulse has arrived. Here, $\mathfrak{m}_{1a} + \mathfrak{m}_{2a} + \mathfrak{m}_{3a} + \mathfrak{m}_{4a}$ are the sum of the counts from only the QD. We determine them by subtracting the background and detector dark counts (that are measured in dependently of the emitter as we discussed earlier) from the total signal. Knowing $\phi_\varepsilon$, we can solve for $\varepsilon$. The collection probabilities $C_k(X, Y)$ depend on the emitter location, so the value of $\varepsilon$ will change as we sample the likelihood distribution.

Similarly, the sum of the counts from the QD that have arrived in every pixel between $\mathrm{t_c}$ and T divided by N,

$$A_b = \frac{\mathfrak{m}_{1b} + \mathfrak{m}_{2b} + \mathfrak{m}_{3b} + \mathfrak{m}_{4b}}{N} = \varepsilon(1 - \phi_\varepsilon) \sum_{k=1}^{4} C_k \tag{5.14}$$

is equal to the sum of the probabilities to detect a photon from the QD in one of the pixels during time window b after one pulse has arrived. Eqns. 5.13 and 5.14 can be used as an alternative way to find *both* $\varepsilon$ and $\phi_\varepsilon$[51]. It would be useful if we could identify the emitter location for the case of a fluctuating rather than constant background, so the values of $B_1$, $B_2$, $B_3$, and $B_4$ are different for each time bin that we determine the location. As we showed earlier, we independently measure the background probabilities and assume they are constant for a given substrate at a given focal

[51] Whereas earlier in this section we showed how to get $\phi_\varepsilon$ from the arrival time histogram of the data.

position. While this is a fine assumption for the substrates that we examine, it is not always the case, and improperly accounting for the background causes localization inaccuracies. Neither MLE using $\mathcal{L}_{CW}$ nor MLE using $\mathcal{L}_{pulsed}$ allow us to locate the emitters without knowing the background probabilities, but it may be possible to extract the background probabilities *and* the emitter location if we implement MLE with $\mathcal{L}_T$. This is still under investigation, though we suspect we may be successful if both $\phi_\varepsilon$ and $\phi_B$ are known quantities.

## 5.5: Determining the observable probabilities $\mathcal{P}_i$

The likelihood distributions presented in this chapter are a function of observable probabilities $\mathcal{P}_i$, which are the probabilities to see a particular observable $o_i$ after a single laser pulse arrives. For our four-pixel system, we define a set of nine different observables $\{o_i\}$ where *i* = 1a, 2a, 3a, 4a, 1b, 2b, 3b, 4b, and >, and each $o_i$ has a corresponding $\mathcal{P}_i$ that we must determine. For the likelihood distribution $\mathcal{L}_T$, the $\mathcal{P}_i$ values can be determined by expanding Eq. 5.10 and then summing the terms that correspond to each observable $o_i$. For example, one of the terms generated by expanding Eq. 5.10 is $\varepsilon C_1 \phi_\varepsilon (1-\phi_B) \prod_{k=1}^{4}(1-B_k) \prod_{k=1}^{4}(1-\phi_{Dka}-\phi_{Dkb})$, and if we inspect that set of outcomes, we see it corresponds to a single photon from the QD count being detected in pixel 1 during time window a, so we will observe $o_{1a}$. The probability of that set of outcomes will contribute to the corresponding observable probability for $o_{1a}$, so $\mathcal{P}_{1a} = \varepsilon C_1 \phi_\varepsilon (1-\phi_B) \prod_{k=1}^{4}(1-B_k) \prod_{k=1}^{4}(1-\phi_{Dka}-\phi_{Dkb}) + \cdots$. Individual inspection and sorting of the sets of outcomes (51,840 for our system) is impossible, so we created a numerical method for doing this without inspection. This involves constructing a column vector [P] that has 51,840 elements corresponding to each of the terms generated from the expansion of Eq. 5.10, and it involves constructing "observable matrices" $[\mathcal{O}_i]$ (each of them also have 51,840 elements) that give the observable probability when they are multiplied by [P], so $\mathcal{P}_i = [P]^T\,[\mathcal{O}_i]$. In this section,

we will provide an example of how to construct [P] and its corresponding $[\mathcal{O}_i]$ matrices for a system in which photons from a single QD are collected by two pixels, and we will provide another example for a system in which photons from background and a single QD are collected by two pixels (which is the system illustrated in Fig. 5.2)[52]. Constructing the matrices for the full system of four pixels collecting dark counts, background counts, and QD photons in two different time windows is too long for a formal writeup, but we believe we have left the reader with all the necessary tools to construct the $\mathcal{P}_i$ for more complicated systems.

For the first example, [P] is a vector whose elements correspond to the terms generated by multiplying the emission outcomes $1 = \varepsilon + (1-\varepsilon)$ and the detection outcomes $1 = C_1 + C_2 + (1 - C_1 - C_2)$. We express the emission outcomes as a 2×1 column matrix,

$$\begin{bmatrix} \varepsilon \\ (1-\varepsilon) \end{bmatrix}, \tag{5.15a}$$

and we express the detection outcomes as a 1×3 row matrix,

$$[C_1 \quad C_2 \quad (1 - C_1 - C_2)]. \tag{5.15b}$$

Multiplication of the two matrices (5.15a) and (5.15b),

$$\begin{bmatrix} \varepsilon \\ (1-\varepsilon) \end{bmatrix} [C_1 \quad C_2 \quad (1 - C_1 - C_2)] = \tag{5.15c}$$

$$\begin{bmatrix} \varepsilon C_1 & \varepsilon C_2 & \varepsilon(1 - C_1 - C_2) \\ (1-\varepsilon)C_1 & (1-\varepsilon)C_2 & (1-\varepsilon)(1 - C_1 - C_2) \end{bmatrix},$$

gives a $2 \times 3$ matrix. If we transpose and vectorize it, we find that

[52] Note that there may be a more concise way solve this problem, this was just the one that we came up with to get the job done.

$$[P] = vec([2 \times 3]^T) = \begin{bmatrix} \varepsilon C_1 \\ \varepsilon C_2 \\ \varepsilon(1 - C_1 - C_2) \\ (1 - \varepsilon)C_1 \\ (1 - \varepsilon)C_2 \\ (1 - \varepsilon)(1 - C_1 - C_2) \end{bmatrix}. \quad (5.15d)$$

It is simple to interpret each of the elements in [P] symbolically and sort them into observables probabilities: the first element is the probability to detect a photon in pixel 1 and it is equal to the observable probability $\mathcal{P}_1 = \varepsilon C_1$; the second element is the probability to detect a photon in pixel 2 and it is equal and it is equal to the observable probability $\mathcal{P}_2 = \varepsilon C_2$. The observable probability to detect nothing is the sum of elements 3 through 6. For a more complicated system than this one, it is not efficient to sort the elements of [P] into observable probabilities by hand, so we generate two 6×1 observable matrices by modifying and then multiplying the vectors that were originally used to make [P]. First, we focus on the outcome where a photon is emitted, so $\varepsilon = 1$. The column matrix (5.15a) becomes

$$\begin{bmatrix} 1 \\ 0 \end{bmatrix}, \quad (5.16a)$$

Next, we focus on the outcome in which the photon lands in pixel 1, so $C_1 = 1$ and $C_2 = 0$. The row matrix (5.15b) becomes,

$$[1 \quad 0 \quad 0]. \quad (5.16b)$$

The product of (5.16a) and (5.16b) generates a 2x3 matrix, and rewriting its transpose as a column vector gives the 6x1 observable matrix,

$$vec\left(\left(\begin{bmatrix}1\\0\end{bmatrix} * [1 \quad 0 \quad 0]\right)^T\right) = \begin{bmatrix}1\\0\\0\\0\\0\\0\end{bmatrix} \equiv [\varepsilon_1] \tag{5.16c}$$

We call this observable matrix $[\varepsilon_1]$. Notice that the first element in $[\varepsilon_1]$ is a one, and the first element in [P] corresponds to the probability that an emitted photon was detected in pixel 1. All the other elements in $[\varepsilon_1]$ are zero, and all the other elements in [P] correspond to probabilities where nothing is collected in pixel 1. For this system, there are no contributions to the counts in pixel 1 apart from the emitter, so $[\varepsilon_1] = [\mathcal{O}_1]$. (The next example will require more finesse to get the observable matrices).

The observable probability $\mathcal{P}_1$ to detect a count from the emitter in pixel 1 can be extracted by multiplying $[P]^T$ and $[\mathcal{O}_1]$, which conveniently gives back the term in the first row of [P].

$$\mathcal{P}_1 = [P]^T[\mathcal{O}_1] = \begin{bmatrix}\varepsilon C_1\\ \varepsilon C_2\\ \varepsilon(1-C_1-C_2)\\ (1-\varepsilon)C_1\\ (1-\varepsilon)C_2\\ (1-\varepsilon)(1-C_1-C_2)\end{bmatrix}^T \begin{bmatrix}1\\0\\0\\0\\0\\0\end{bmatrix} = \varepsilon C_1. \tag{5.17}$$

Similarly, we can extract the observable probability $\mathcal{P}_2$ to detect a count from the emitter in pixel 2 using the observable matrix $[\mathcal{O}_2]$. To generate it, we set $\varepsilon$=1 in (5.15a), we set $C_1 = 0$ and $C_2 = 1$ in (5.15b), and we multiply them.

$$vec\left(\left(\begin{bmatrix}1\\0\end{bmatrix} * \begin{bmatrix}0 & 1 & 0\end{bmatrix}\right)^T\right) = \begin{bmatrix}0\\1\\0\\0\\0\\0\end{bmatrix} \equiv [\varepsilon_2]. \tag{5.18}$$

Once again, the only nonzero term in $[\varepsilon_2]$ is in the same row as the term in [P] that corresponds to the probability that an emitted photon was detected in pixel 2. For this system, there are no contributions to the counts in pixel 2 apart from the emitter, so $[\varepsilon_2] = [\mathcal{O}_2]$. Just as we calculated $\mathcal{P}_1$, the observable probability $\mathcal{P}_2$ to detect a count in pixel 2 is the product,

$$\mathcal{P}_2 = [P]^T[\mathcal{O}_2]. = \begin{bmatrix} \varepsilon C_1 \\ \varepsilon C_2 \\ \varepsilon(1 - C_1 - C_2) \\ (1-\varepsilon)C_1 \\ (1-\varepsilon)C_2 \\ (1-\varepsilon)(1 - C_1 - C_2) \end{bmatrix}^T \begin{bmatrix}0\\1\\0\\0\\0\\0\end{bmatrix} = \varepsilon C_2. \tag{5.19}$$

We have just completed the process for generating [P] and its corresponding observable matrices $[\mathcal{O}_1]$ and $[\mathcal{O}_2]$ for the case of two pixels receiving counts from a single QD, so the observable probabilities that are used in the likelihood distribution can be extracted from [P] without inspection.

Let us now extract the observable probabilities for the system described by the probability tree in Fig. 5.2. First, we account for the probability of background counts arriving in pixel 1 by taking the product of [P] in Eq. 5.15d and a $1 \times 2$ matrix that contains the probabilities of background counts arriving in pixel 1 which gives a $6 \times 2$ matrix. If we transpose and vectorize it, we generate a new $12 \times 1$ probability matrix,

$$[P'] = vec(([P] * [B_1 \quad 1 - B_1])^T) = \begin{bmatrix} \varepsilon C_1 B_1 \\ \varepsilon C_1 (1 - B_1) \\ \varepsilon C_2 B_1 \\ \varepsilon C_2 (1 - B_1) \\ \varepsilon (1 - C_1 - C_2) B_1 \\ \varepsilon (1 - C_1 - C_2)(1 - B_1) \\ \vdots \end{bmatrix}. \tag{5.20}$$

The 6x1 matrices $[\varepsilon_1]$ and $[\varepsilon_2]$ must be extended so their unity terms remain in the same rows as the terms in [P'] that indicate a QD photon arrived in pixel 1 and pixel 2, respectively. To do that, we multiply both matrices by a $1 \times 2$ vector of ones which gives two matrices that can are transformed and vectorized to give two $12 \times 1$ matrices,

$$[\varepsilon_1{}'] = vec(([\varepsilon_1][1 \quad 1])^T) = \begin{bmatrix} 1 \\ 1 \\ 0 \\ 0 \\ 0 \\ \vdots \end{bmatrix} \text{ and } [\varepsilon_2{}'] = vec(([\varepsilon_2][1 \quad 1])^T) = \begin{bmatrix} 0 \\ 0 \\ 1 \\ 1 \\ 0 \\ \vdots \end{bmatrix}. \tag{5.21a,b}$$

Notice that the unity terms in $[\varepsilon_1{}']$and $[\varepsilon_2{}']$ correspond to the rows of [P] that contain the probability receiving a QD count in detectors 1 and 2, respectively:

$$[P'] \qquad [\varepsilon_1{}'] \qquad [\varepsilon_2{}']$$

$$\begin{bmatrix} \varepsilon C_1 B_1 \\ \varepsilon C_1 (1 - B_1) \\ \varepsilon C_2 B_1 \\ \varepsilon C_2 (1 - B_1) \\ \varepsilon (1 - C_1 - C_2) B_1 \\ \varepsilon (1 - C_1 - C_2)(1 - B_1) \\ \vdots \end{bmatrix} \quad \begin{bmatrix} 1 \\ 1 \\ 0 \\ 0 \\ 0 \\ 0 \\ \vdots \end{bmatrix} \quad \begin{bmatrix} 0 \\ 1 \\ 1 \\ 1 \\ 0 \\ 0 \\ \vdots \end{bmatrix}$$

This must be the case so the product $[P']^T[\varepsilon_1']$ pulls out all the probability terms where a QD photon was detected in pixel 1, and the product $[P']^T[\varepsilon_2']$ pulls out all the probability terms where a QD photon was detected in pixel 2.

We must also define a $12 \times 1$ matrix $[B_1]$ that has unity terms in the same rows as the terms in [P'] that indicate a background photon arrived in pixel 1. For this, we require a $12 \times 1$ matrix that has alternating zeros and ones, which we can get from the product,

$$[B_1] = vec\left(\left(\begin{bmatrix}1\\1\\1\\1\\1\\1\end{bmatrix} * \begin{bmatrix}1 & 0\end{bmatrix}\right)^T\right) = \begin{bmatrix}1\\0\\1\\0\\1\\\vdots\end{bmatrix}. \tag{5.22}$$

Notice that the unity terms in $[B_1]$ correspond to the rows of $[P']$ that contain the probability of receiving a background count in detector 1:

$$\begin{matrix}[\boldsymbol{P'}]\end{matrix} \qquad \begin{matrix}[\boldsymbol{B_1}]\end{matrix}$$

$$\begin{bmatrix}\boldsymbol{\varepsilon C_1 B_1}\\ \varepsilon C_1(1-B_1)\\ \boldsymbol{\varepsilon C_2 B_1}\\ \varepsilon C_2(1-B_1)\\ \boldsymbol{\varepsilon(1-C_1-C_2)B_1}\\ \varepsilon(1-C_1-C_2)(1-B_1)\\ \vdots\end{bmatrix} \qquad \begin{bmatrix}1\\0\\1\\0\\1\\0\\\vdots\end{bmatrix}$$

We knew we wanted that alternating one-zero form so that the product $[P']^T[B_1]$ pulls out all the probability terms containing the probability a background photon is detected in pixel 1.

Next, we incorporate the probability of background counts from detector 2 by multiplying $[P']$ by the detector 2 background probabilities which gives a $24 \times 1$ matrix,

$$[P''] = vec(([P'] * [B_2 \quad 1 - B_2])^T) = \begin{bmatrix} \varepsilon \frac{A_1}{A} B_1 B_2 \\ \varepsilon \frac{A_1}{A} B_1 (1 - B_2) \\ \varepsilon \frac{A_1}{A} (1 - B_1) B_2 \\ \varepsilon \frac{A_1}{A} (1 - B_1)(1 - B_2) \\ \varepsilon \frac{A_2}{A} B_1 B_2 \\ \vdots \end{bmatrix}. \tag{5.23}$$

The matrices $[\varepsilon_1']$, $[\varepsilon_2']$, and $[B_1]$ must also be extended to give $24 \times 1$ matrices with unity terms that are in the same rows as the corresponding probabilities in [P''']. Once again, we extend these by multiplying them by $1 \times 2$ unity vectors which gives

$$[\varepsilon_1''] = vec(([\varepsilon_1'] * [1 \quad 1])^T) = \begin{bmatrix} 1 \\ 1 \\ 1 \\ 1 \\ 0 \\ \vdots \end{bmatrix}, \tag{5.24}$$

$$[\varepsilon_2''] = vec(([\varepsilon_2'] * [1 \quad 1])^T) = \begin{bmatrix} 0 \\ 0 \\ 0 \\ 0 \\ 1 \\ \vdots \end{bmatrix}, \text{ and} \tag{5.25}$$

$$[B_1'] = vec(([B_1] * [1 \quad 1])^T) = \begin{bmatrix} 1 \\ 1 \\ 0 \\ 0 \\ 1 \\ \vdots \end{bmatrix}. \tag{5.26}$$

In addition, we define a matrix $[B_2]$ that keeps track of terms in [P'''] for which a background photon arrives in pixel 2. For this, we require a $24 \times 1$ matrix that has alternating zeros and ones which we get from the product,

$$[B_2] = vec\left(\left(\begin{bmatrix}1\\1\\1\\1\\1\\\vdots\end{bmatrix} * \begin{bmatrix}1 & 0\end{bmatrix}\right)^T\right) = \begin{bmatrix}1\\0\\1\\0\\1\\\vdots\end{bmatrix}. \tag{5.27}$$

There are only three observable probabilities $\mathcal{P}_1$, $\mathcal{P}_2$, and $\mathcal{P}_>$ that can be extracted from $[P'']$ (Eq. 5.23) using three observable probability matrices $[\mathcal{O}_1]$, $[\mathcal{O}_2]$, and $[\mathcal{O}_>]$, so we need to parse $[{\varepsilon_1}'']$, $[{\varepsilon_2}'']$, $[{B_1}']$, and $[B_2]$ to get the observable matrices. To do this, the computer compares the values of $[{\varepsilon_1}'']$, $[{\varepsilon_2}'']$, $[{B_1}']$, and $[B_2]$ for each row, and places either a zero or one in the same row of each of the observable matrices. Here are the observable matrices side-by-side with the original ones, so you can interpret different rows and confirm how the elements in the observable matrices are assigned:

$$[{\varepsilon_1}''] = \begin{bmatrix}1\\1\\1\\1\\0\\0\\0\\0\\0\\0\\0\\0\\0\\0\\\vdots\end{bmatrix};\quad [{\varepsilon_2}'] = \begin{bmatrix}0\\0\\0\\0\\1\\1\\1\\1\\0\\0\\0\\0\\0\\0\\\vdots\end{bmatrix};\quad [{B_1}'] = \begin{bmatrix}1\\1\\0\\0\\1\\1\\0\\0\\1\\1\\0\\0\\1\\1\\\vdots\end{bmatrix};\quad [B_2] = \begin{bmatrix}1\\0\\1\\0\\1\\0\\1\\0\\1\\0\\1\\0\\1\\0\\\vdots\end{bmatrix} \quad\Rightarrow\quad [\mathcal{O}_1] = \begin{bmatrix}0\\1\\0\\1\\0\\0\\0\\0\\0\\0\\0\\0\\1\\0\\\vdots\end{bmatrix};\ [\mathcal{O}_2] = \begin{bmatrix}0\\0\\0\\0\\0\\0\\1\\1\\0\\1\\1\\0\\0\\1\\\vdots\end{bmatrix};\quad [\mathcal{O}_>] = \begin{bmatrix}1\\0\\1\\0\\1\\1\\0\\0\\1\\0\\0\\0\\1\\0\\\vdots\end{bmatrix}.$$

Let us manually parse the first four rows of $[{\varepsilon_1}'']$, $[{\varepsilon_2}'']$, $[{B_1}']$, and $[B_2]$ to give ourselves an idea of how the computer does this. The first element of $[P'']$ is $\varepsilon\frac{A_1}{A}B_1B_2$ and it corresponds to a multi-arrival observable, so $[\mathcal{O}_>](1,1)=1$ and $[\mathcal{O}_1](1,1) = [\mathcal{O}_2](1,1) = 0$. The computer

concludes this because the sum of the first row of the tag matrices is greater than 1, and it assigns one to the first element of $[\mathcal{O}_{>}]$ and zero to the first element of $[\mathcal{O}_1]$ and $[\mathcal{O}_2]$. The second element of $[P'']$ is $\varepsilon\frac{A_1}{A}B_1(1-B_2)$ and it corresponds to a set of outcomes where there are two arrivals in pixel 1. As we mentioned earlier in the definition of the multi-arrival observable $\mathcal{O}_{>}$, multiple arrivals in a single pixel are designated as single arrival events, so we need the following elements for the observable matrices: so $[\mathcal{O}_{>}](2,1)=0$ and $[\mathcal{O}_1](2,1)=1$, and $[\mathcal{O}_2](2,1)=0$. The computer compares the values of $[{\varepsilon_1}'']$, $[{\varepsilon_2}'']$, $[{B_1}']$, and $[B_2]$ in the second row and assigns the proper values to the observable matrices.

Just like the first and second elements of $[P'']$, the third element also corresponds to a set of outcomes with more than one arrival. In this case, events are detected in more than one pixel, so this is considered a multi-arrival observable. The computer concludes this because the sum row three elements of the observable tag matrices is three, and it can only be greater than two if there are arrivals in more than one pixel. Consequently, $[\mathcal{O}_{>}](3,1)=1$, $[\mathcal{O}_1](3,1)=0$, and $[\mathcal{O}_2](3,1)=0$. The fourth row of [P''] is simple to interpret as a set of outcomes that should contribute to $\mathcal{P}_1$ because the fourth element of all the tag matrices is zero except for $[{\varepsilon_1}'']$(4,1)=1, so the computer assigns $[\mathcal{O}_{>}](4,1)=0$, $[\mathcal{O}_1](4,1)=1$, and $[\mathcal{O}_2](4,1)=0$.. This is basic premise for to parse the rows of the original tag matrices numerically and create new tag matrices that correctly pull out the observable probabilities.

In our actual experiment, four detectors register dark counts, fluorescent background, and photons from a single emitter either before or after a cut time $t_c$, so the number of terms in the overall probability matrix is much larger and there are more event tag matrices that must be sorted into the nine final observable matrices, $[\mathcal{O}_i]$, (where *i = 1a,2a,3a,4a,1b,2b,3b,4b,>*). However,

the procedure for generating the probability matrix and tag matrices remains the same, and we hope we have given the reader the tools to work out that scenario.

# CHAPTER 6. Resolving non-blinking emitters

This work is an extension of the time-resolved analysis method introduced in the previous chapter. As a reminder, we introduced the likelihood distribution $\mathcal{L}_T(X, Y; \{m_i\}, N)$ for the location $(X, Y)$ of an emitter given the set of counts $\{m_i\}$ arriving in the four pixels after *N* pulses had arrived. We incorporated the photon arrival time information into the distribution by sorting the counts based on whether each of their micro-times was shorter or longer than a designated cut time $t_c$ within the laser pulse period. For example, $m_{1a}$ was the number of times that a single count was registered in pixel 1 before $t_c$, and $m_{1b}$ was the number of times that a count was registered in pixel 1 after $t_c$. The set of counts $\{m_i\} = m_{1a}, m_{1b}, m_{2a}, m_{2b}$ ... included the contributions to the four pixels before and after $t_c$.

Now, we will extent the method to find the locations of *two* emitters by maximizing a likelihood distribution $\mathcal{L}_T(X_1, Y_1, X_2, Y_2; \{m_i\}, N)$ for the locations $(X_1, Y_1)$ and $(X_2, Y_2)$. Provided the emitters have different lifetimes, we will see that we can access both of their positions through the same set of counts $\{m_i\}$. Unlike most SR methods, this does not require blinking of the emitters to resolve them. It is analogous to multi-color SR imaging, in which nonblinking emitters can be resolved if they are spectrally different[100–102]. Here, we take advantage of the time regime rather than the energy regime.

We note that another method for extracting the locations of two nonblinking emitters based on disparities in lifetime was already developed by Heilemann, et. al[98]. This method (as far as we can tell) fits a bi-exponential $\psi(t) = \frac{w_1}{\tau_1} e^{-\frac{t}{\tau_1}} + \frac{w_2}{\tau_2} e^{-\frac{t}{\tau_2}}$ to the arrival time distribution in each pixel and uses the weights to divide the counts $m_k$ in each pixel into two subsets, $w_1 m_k$ and $w_2 m_k$.

Next, a likelihood distribution is maximized for a location $(X_1, Y_1)$ given the counts $w_1m_1, w_1m_2, w_1m_3, \ldots$. Additionally, a likelihood distribution is maximized for a location $(X_2, Y_2)$ given the counts $w_2m_1, w_2m_2, w_2m_3, \ldots$. The accuracy of this method no doubt suffers when the weights and lifetimes cannot be confidently determined. We have yet to compare its performance to our method.

## 6.1: Analyzing data with $\mathcal{L}_T$

To benchmark the analysis method, we first analyzed simulated data. Fig. 6.1a illustrates the capability of the technique to successfully resolve two emitters with disparate lifetimes. For the simulation, one emitter (QD1) with a lifetime of 5 ns was placed at the origin $(X_1, Y_1)$= (0, 0) nm, and another emitter (QD2) with a lifetime of 50 ns was placed 5 nm away at $(X_2, Y_2)$= (3.5, 3.5) nm. The simulation was run for 25 "seconds", and the locations of both emitters were found by maximizing $\mathcal{L}_T(X_1, Y_1, X_2, Y_2; \{m_i\}, N)$ for every time window $\Delta t$ = 0.25 sec. The locations plotted in blue correspond to the locations identified for QD1 and those in red correspond to the locations identified for QD2. The localization precision $(\sigma_{X1}, \sigma_{Y1})$= (1.3, 1.2) nm found for QD1 was the same as the localization precision $(\sigma_{X2}, \sigma_{Y2})$= (1.2, 1.3) nm for the emitter with the 50 ns lifetime; both of these were determined from the standard deviation of locations found for the respective emitters. We found their respective average locations $(\langle X_1 \rangle, \langle Y_1 \rangle)$ = (0.0±0.1, 0.0±0.1) nm and $(\langle X_1 \rangle, \langle Y_1 \rangle)$ = (3.6±0.1, 3.4±0.1) nm agreed (were practically indistinguishable) with the ones used to simulate the data[53].

[53] To maximize the likelihood with the "simplex method", we sampled the peak of $\mathcal{L}_T$with increasingly smaller step sizes. For analyzing this data, 0.1 nm step sizes were the smallest ones used in the routine.

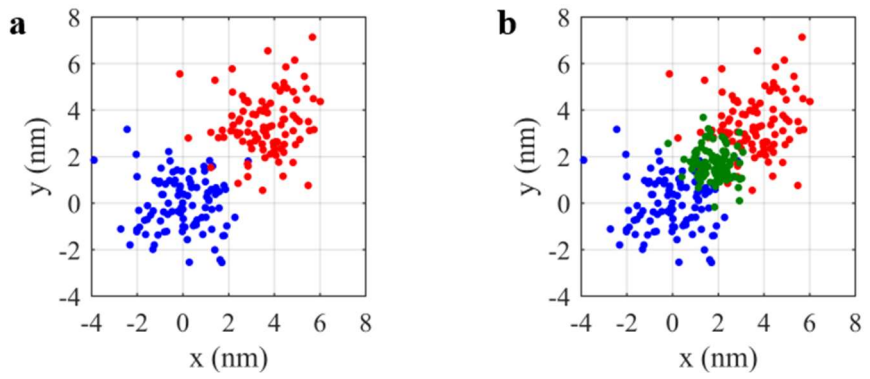


**Figure 6.1 Resolving nonblinking emitters with disparate lifetimes**. Simulated data of two emitters with lifetimes of 5 and 50 ns, located at (0, 0) nm and (3.5, 3.5) nm, respectively, is analyzed by maximizing $\mathcal{L}_T(X_1, Y_1, X_2, Y_2)$ to recover the locations $(X_1, Y_1)$ and $(X_2, Y_2)$ of both the emitters. (a) Pairs of locations found for each $\Delta t$ = 0.25 sec are plotted in blue and red for 25 sec of data, and their averages $(\langle X_1 \rangle, \langle Y_1 \rangle)$ = (0.0±0.1, 0.0±0.1) nm and $(\langle X_1 \rangle, \langle Y_1 \rangle)$ = (3.6±0.1, 3.4±0.1) agree with the true locations. (b) The superimposed locations in green are found by maximizing the likelihood distribution $\mathcal{L}_T(X, Y)$ for the location of a single emitter for each $\Delta t$ of the same simulated data, for which locations are found halfway between the two true locations of the emitters at (1.8±0.1, 1.7±0.1) on average.

Fig. 6.1b superimposes the locations (plotted in green) that are found by maximizing the likelihood distribution $\mathcal{L}_T(X, Y)$ derived in the previous chapter for the location $(X, Y)$ of *one* emitter[54]. These are found with a localization precision of $(\sigma_X, \sigma_Y)$= (0.7, 0.7) nm and their average (1.8±0.1, 1.7±0.1) is halfway between the locations of the two emitters, which is exactly what one expects to attain anytime they are locating two non-blinking emitters. This should remind readers of the SR imaging of QD pairs from Chapter 4, in which we were often identifying locations halfway between two nonblinking QDs. One wonders if we can now return to the same datasets and resolve them if they have disparate-enough lifetimes. We will attempt this in the next section.

To simulate the data shown Fig. 6.1, we selected a pulse period of $T$=400 ns and emission probabilities $\varepsilon_1 = \varepsilon_2 = 0.1$. Typically, experimental values for $\varepsilon$ are ~0.01, so we would have to

[54] When maximizing $\mathcal{L}_T$, these locations are used as a starting location for a global search that samples random locations about that starting location. Depending on the sample , the global search examines points ± 10-50 nm from the starting location before beginning the simplex method where increasingly smaller step sizes (down to 0.1-2 nm) are used to approach the peak.

collect experimental data for ten times as long to obtain the same level of counts. The background and dark count contributions were comparable to measured values from experiments. For these, we simulated a background with a lifetime of 2 ns, and probability per pulse of $B_k = 2.5e-4$ which was the same for each pixel, and a rate of dark counts $R_{Dk}$=500e-9 counts/sec which was also the same for each pixel. A $\Delta t$ of 0.25 sec was selected, meaning $N$ = 625,000[55]. The simulated and experimental data were analyzed with the same program which required two additional files: data collected with *only* the background and dark counts, and data collected with only the dark counts. The program used these to extract the values of $\{B_k\}, \phi_B$, $\{\phi_{Dka}\}$, and $\{\phi_{Dkb}\}$. To duplicate the experimental workflow, we simulated data of background and dark counts, and data containing contributions from only dark counts. We also included the instrument response function (IRF) some simulations to mimic experimental data[56]. This does not impact the localization accuracy provided that our selection or calculation of $\phi_{\varepsilon 1}$, $\phi_{\varepsilon 2}$, and $\phi_B$, appropriately incorporates the IRF.

When analyzing the simulated data shown in Fig. 6.1, we provided the localization algorithm with the counts $\{m_i\}$, the number of pulses $N$, the PSF widths in $x$ and $y$, and the lifetimes $\tau_1$ and $\tau_2$ of the emitters. We let the algorithm determine $\varepsilon_1, \varepsilon_2, \{B_k\}, \phi_B$, and $\{\phi_{Dka}\}$, for which it indeed extracted values that match the ones used to generate the simulation. Of the information provided to the localization algorithm, the $\{m_i\}$, $N$, and the PSF widths can easily be ascertained from experimental data[57]. However, that is not true for the $\tau_1$ and $\tau_2$ , which the simulation uses to

[55] It took 108 minutes to run this simulation on a Lenovo-920 laptop.

[57] See Section 3.3 for details on how to measure the PSF. We assume it is the same for both emitters when analyzing experimental data, which will not be the case if the emission wavelengths of the two emitters are substantially different since the width of the PSF is directly proportional to the wavelength of light.

compute the necessary parameters $\phi_{\varepsilon 1} = 1 - e^{-t_c/\tau_1}$ and $\phi_{\varepsilon 2} = 1 - e^{-t_c/\tau_2}$. For the analysis of experimental data that we do later in this section, we must estimate $\phi_{\varepsilon 1}$ and $\phi_{\varepsilon 2}$, which presents a significant hurdle.

We solved for $\varepsilon_1$ and $\varepsilon_2$ in a similar way that we solved for $\varepsilon$ in the previous chapter. Notice that the number of photons collected from both QDs before $t_c$ divided by the total number of pulses *N*,

$$\frac{\mathfrak{m}_{1a} + \mathfrak{m}_{2a} + \mathfrak{m}_{3a} + \mathfrak{m}_{4a}}{N} = \varepsilon_1 \phi_{\varepsilon 1} \sum_{k=1}^{4} C_k(X_1, Y_1) + \varepsilon_2 \phi_{\varepsilon 2} \sum_{k=1}^{4} C_k(X_2, Y_2), \tag{6.1}$$

is equal to the sum of the probabilities to detect a photon after a single pulse has arrived from one of the QDs in one of the pixels before a time $t_c$. Here, $\mathfrak{m}_{1a} + \mathfrak{m}_{2a} + \mathfrak{m}_{3a} + \mathfrak{m}_{4a}$ is the sum of the counts from *only* the two QDs. We determine them by subtracting the average background and detector dark count contributions from the total signal. These, as we discussed earlier, are measured independently of the emitter. The sum $\mathfrak{m}_{1b} + \mathfrak{m}_{2b} + \mathfrak{m}_{3b} + \mathfrak{m}_{4b}$ of the photons collected from both QDs after $t_c$ gives a second relationship:

$$\frac{\mathfrak{m}_{1b} + \mathfrak{m}_{2b} + \mathfrak{m}_{3b} + \mathfrak{m}_{4b}}{N} \tag{6.2}$$

$$= \varepsilon_1 (1 - \phi_{\varepsilon 1}) \sum_{k=1}^{4} C_k(X_1, Y_1) + \varepsilon_2 (1 - \phi_{\varepsilon 2}) \sum_{k=1}^{4} C_k(X_2, Y_2).$$

We use Eqns. 6.1 and 6.2 to solve for $\varepsilon_1$ and $\varepsilon_2$ in terms of $C_k(X_1, Y_1)$, $C_k(X_2, Y_2)$, $\phi_{\varepsilon 1}$, and $\phi_{\varepsilon 2}$. We must keep solving for $\varepsilon_1$ and $\varepsilon_2$ as we sample the likelihood distribution for different values of $X_1, Y_1, X_2$, and $Y_2$ because the collection probabilities $C_k$ depend on these locations, but this gives us an easy way to extract these parameters correctly, provided that we have supplied the correct values for $\phi_{\varepsilon 1}$ and $\phi_{\varepsilon 2}$. Alternatively, we can find for $\varepsilon_1$ and $\varepsilon_2$ by sampling the likelihood

distribution in six dimensions; this is done by maximizing $\mathcal{L}_T(X_1, Y_1, \varepsilon_1, X_2, Y_2, \varepsilon_2)$, but it is computationally costly. Both methods give the same $\varepsilon_1$ and $\varepsilon_2$.

Just as the selection of $t_c$ mattered in the previous chapter, it plays a role in the analysis here. We found the precision was optimized when the values of $\phi_{\varepsilon 1}$ and $\phi_{\varepsilon 2}$ were most disparate, and that disparity could be toggled with $t_c$. For the simulation in Fig. 6.1, a selection of $t_c = 14$ ns was used because that yielded values $\phi_{\varepsilon 1}$=0.94 and $\phi_{\varepsilon 2}$=0.24 which were farthest apart.

Unsurprisingly, the localization precision depended on the disparity of the emitters' lifetimes. Fig. 6.2 illustrates decrease in precision that occurs as the lifetimes of the two emitters grow close to one another. In these simulations, the emitter at the origin was given a lifetime of 50 ns, and the second emitter located 20 nm away at (14, 14) nm was given lifetimes of 10, 25, and 40 ns for the respective simulations. The locations found by analyzing the three simulations are plotted in Fig. 6.2(a-c). The red points correspond to the locations found for the emitter with the 50 ns lifetime, and the blue points correspond to the locations found for the emitter with the shorter lifetime. The localization precision and average locations for the three simulations are summarized in Table 6.1. Additionally, in Fig. 6.2c, we can start to see artifacts that arise when trying to resolve emitters with lifetimes that are too similar: the spread in localizations is skewed perpendicular to the separation vector between the two emitters. When this phenomenon occurs, we know that we are on the cusp of not being able to identify multiple locations, which occurs when the likelihood distribution develops ridges or multiple peaks of equal height.

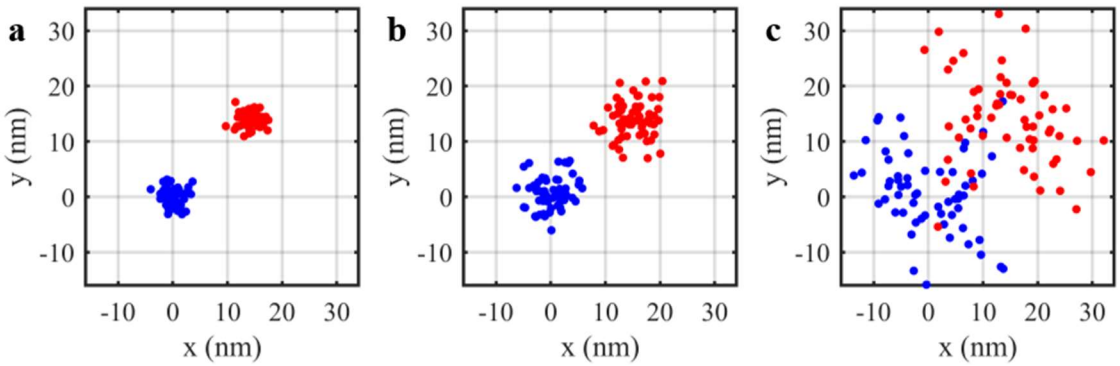


**Figure 6.2 Precision is related to the difference in lifetimes**. Pairs of locations are found with MLE for three different simulations of two emitters located at (0, 0) nm and (14, 14) nm, respectively. The respective locations found for the emitters are plotted with colors corresponding to the short (blue) and long (red) lifetimes of the emitters which were (a) 10 and 50 ns, (b) 25 and 50 ns, and (c) 40 and 50 ns, respectively.

Apart from the lifetime changes, the parameters in the simulations analyzed to generate Fig. 6.2 were identical to those used to generate the data for Fig. 6.1. Each simulation was run for 15 seconds and $\Delta t$ was 0.25 sec. For the analysis, $t_c$ was selected to maximize the difference between $\phi_{\varepsilon 1}$ and $\phi_{\varepsilon 2}$ which was achieved with values of 20 ns, 35 ns, and 45 ns for the respective simulations. The analysis program was provided with the true values of $\phi_{\varepsilon 1}$ and $\phi_{\varepsilon 2}$ for each of the simulations.

**Table 6.1.**

**Resolving simulated emitters with lifetimes approaching one another.**

| | $\tau_1$ (ns) | $\tau_2$ (ns) | $\sqrt{{\sigma_{X1}}^2 + {\sigma_{Y1}}^2}$ | $\sqrt{{\sigma_{X2}}^2 + {\sigma_{Y2}}^2}$ | $\langle X_1 \rangle$ | $\langle Y_1 \rangle$ | $\langle X_2 \rangle$ | $\langle Y_2 \rangle$ |
|---|---|---|---|---|---|---|---|---|
| Simulation 1 | 10 | 50 | 2.2 | 1.0 | 0.0 ± 0.2 | 0.1 ± 0.2 | 14.2 ± 0.2 | 14.0 ± 0.2 |
| Simulation 2 | 25 | 50 | 4.0 | 4.5 | 0.0 ± 0.4 | 0.7 ± 0.4 | 14.9 ± 0.4 | 13.9 ± 0.4 |
| Simulation 3 | 40 | 50 | 10.1 | 11.1 | 0.2 ± 0.9 | 0.9 ± 0.9 | 15 ± 1 | 14 ± 1 |

We were eager to apply this analysis method to experimental data collected from single QDs for which we had observed bi-exponential decays with distinct lifetimes. We wondered if the different radiative decay pathways were associated, on average, with different regions on the QD (or not), and if this method could be used to extract that information. While we would expect photons to be emitted symmetrically with respect to the QD center because the QD is a sphere, disorder may break that symmetry. We hypothesized that trapped charges, lattice defects, or interactions with the substrate might introduce asymmetries in the exciton migration before recombination that resulted in preferential recombination on specific regions of the QD. On spatial scales above the diffraction limit, similar time-resolved microscopy methods have been used to monitor the exciton lifetime in relation to the structure of a material[103,104], and our method would allow one to explore that relationship on smaller spatial scales.

We have applied the method to real data, but the results of our analysis hinge upon the values of $\phi_{\varepsilon 1}$ and $\phi_{\varepsilon 2}$ that we must provide to the algorithm[58]. We have found the method is extremely sensitive to the selection of these parameters, so we must figure out a way to obtain their values. This is where the problem currently stands.

## 6.2: Extending $\mathcal{L}_T$ for locating two emitters

We start by building a model that contains the probabilities of every possible set of outcomes after a single laser pulse arrives. Recall from Chapter 5 the various probabilities that were related to the QD emission: $\varepsilon$ was the probability that a photon was emitted by the QD after a laser pulse

[58] One way we have approached this issue is to pretend that we know the lifetime of one of the emitters is short (<7 ns) and select a $t_c$ value that is >~20 ns, then we can safely assume that $\phi_{\varepsilon 1}$ is equal to one. Then, we fit a mono-exponential with a rate $1/\tau$ to the tail of the arrival time distribution, and we assume that the second emitter's probability of arrival before $\phi_{\varepsilon 2} = e^{-t_c/\tau}$ can be accurately defined in terms of the tail fit.

arrived, and $C_k(X,Y)$ was the probability that the photon was collected in pixel $k$, which depended on the location $(X,Y)$ of the QD. To incorporate the temporal information, we defined the probability $\phi_\varepsilon$ that the photon arrived before $t_c$, and we assumed the lifetime of the QD was much shorter than the laser pulse period $T$, so $1-\phi_\varepsilon$ was the probability that the photon arrived after $t_c$ and before $T$. The probabilities of all possible outcomes for the QD emission after the arrival of a single laser pulse could then be identified as terms in an expansion of the product,

$$\big(\varepsilon+(1-\varepsilon)\big)\big(C_1+\cdots+C_4+(1-C_1-\cdots-C_4)\big)\big(\phi_\varepsilon+(1-\phi_\varepsilon)\big) \tag{6.1}$$

Now, we consider the contributions from two emitters which we will call QD1 and QD2 located at $(X_1,Y_1)$ and $(X_2,Y_2)$, respectively, that have respective emission probabilities $\varepsilon_1$ and $\varepsilon_2$, collection probabilities $C_k(X_1,Y_1)$ and $C_k(X_2,Y_2)$, and arrival time probabilities $\phi_{\varepsilon1}$ and $\phi_{\varepsilon2}$. The probabilities of all possible outcomes for the QDs' emission after the arrival time of a single laser pulse can be expressed as a product,

$$\begin{aligned}&\big(\varepsilon_1+(1-\varepsilon_1)\big)\Big(C_1(X_1,Y_1)+\cdots+C_4(X_1,Y_1)+\big(1-C_1(X_1,Y_1)-\cdots-\\&C_4(X_1,Y_1)\big)\Big)\big(\phi_{\varepsilon1}+(1-\phi_{\varepsilon1})\big)\big(\varepsilon_2+(1-\varepsilon_2)\big)\Big(C_1(X_2,Y_2)+\cdots+C_4(X_2,Y_2)+\\&\big(1-C_1(X_2,Y_2)-\cdots-C_4(X_2,Y_2)\big)\Big)\big(\phi_{\varepsilon2}+(1-\phi_{\varepsilon2})\big),\end{aligned} \tag{6.2}$$

of their respective emission probabilities $\varepsilon_1$ and $\varepsilon_2$, collection probabilities $C_k(X_1,Y_1)$ and $C_k(X_2,Y_2)$, and arrival time probabilities $\phi_{\varepsilon1}$ and $\phi_{\varepsilon2}$. Once again, we will assume that both QDs have much shorter lifetimes than $T$, so $1-\phi_{\varepsilon1}$ and $1-\phi_{\varepsilon2}$ are the probabilities that each of the QDs decay before the next pulse arrivals. Just as we saw in Chapter 5, contributions from the background and detector dark counts will extend the product,

$$\left(\varepsilon_1 + (1-\varepsilon_1)\right)\Big(C_1(X_1,Y_1) + \cdots + C_4(X_1,Y_1) + \big(1 - C_1(X_1,Y_1) - \cdots - C_4(X_1,Y_1)\big)\Big)\big(\phi_{\varepsilon 1} + (1-\phi_{\varepsilon 1})\big)\big(\varepsilon_2 + (1-\varepsilon_2)\big)\Big(C_1(X_2,Y_2) + \cdots + C_4(X_2,Y_2) + \big(1 - C_1(X_2,Y_2) - \cdots - C_4(X_2,Y_2)\big)\Big)\big(\phi_{\varepsilon 2} + (1-\phi_{\varepsilon 2})\big)\big(\phi_B + (1-\phi_B)\big)\prod_{k=1}^{4}\big(B_k + (1-B_k)\big)\prod_{k=1}^{4}(\phi_{Dka} + \phi_{Dkb} + (1-\phi_{Dka}-\phi_{Dkb})). \quad (6.3)$$

We then expand Eqn. 6.3 and express this as a sum of outcome probabilities. We have no way of distinguishing between every outcome, so we sort the outcomes into observable probabilities $\mathcal{P}_i(\varepsilon_1, \varepsilon_2, \{C_k(X_1,Y_1)\}, \{C_k(X_2,Y_2)\}, \phi_{\varepsilon 1}, \phi_{\varepsilon 2}, \{B_k\}, \phi_\varepsilon, \phi_B, \{\phi_{Dka}\}, \{\phi_{Dkb}\})$, where $i$ = *1a,2a,3a,4a,1b,2b,3b,4b,>*, using the matrix algebra method from Section 5.5.

To consider the system after $N$ pulses have arrived, we raise Eq. 6.3 to the $N^{\text{th}}$ power and write it as a multinomial expansion. A single term in the expansion is equal to the probability to observe $\{m_i\}$ given $N$ pulses and the set $\{P_i\}$ of observable probabilities. Reversing the dependent and independent variables, we end up with the likelihood distribution for the locations of both emitters,

$$\mathcal{L}_T(X_1, Y_1, X_2, Y_2; \{m_i\}, N, \{\mathcal{P}_i\}) \quad (6.4)$$
$$= \left(\prod_i \mathcal{P}_i{}^{m_i}\right)\left(1 - \sum_i \mathcal{P}_i\right)^{N - \sum_i m_i} \binom{N}{m_>, m_{1a}, m_{1b}, m_{2a}, m_{2b}, \ldots},$$

which readers may recognize as the same form for the likelihood distribution that was written in Eqn. 5.12. For every $N$ pulses, we use the downhill simplex method to identify the maximum of $\ln(\mathcal{L}_T)$ in four dimensions, $X_1, Y_1, X_2$, and $Y_1$, which corresponds to the most likely locations of both emitters.

# CHAPTER 7. Conclusion

Let us now summarize the key findings of this dissertation, which was devoted to understanding how the configuration of QDs within small clusters impacts their energy transfer. For this purpose, we developed a time-resolved super-resolution (SR) microscope capable of simultaneously monitoring the emission centroid with nanometer-scale localization precision and recording the arrival of single photons with sub-nanosecond temporal resolution. The development of the microscope is described in Chapter 2, along with its application to the study of single CdSe/CdS QDs and small clusters of QDs. We were able to resolve multiple regions of emission within clusters by virtue of their blinking, and we were able to identify the lifetime and intensity associated with different regions of the cluster. Moreover, correlated lifetime and intensity behavior confirmed that energy transfer was occurring within the clusters, and we localized regions responsible for accepting and donating energy within the clusters.

Electron microscopy was necessary for uncovering the number and configuration of QDs within the structure, and we acquired correlated images of QDs clusters with both the time-resolved SR microscope and SEM in Chapter 4. This allowed us to identify the lifetime and intensity associated with different quantum dots within the cluster. The success of this experiment has implications for future studies of (blinking) photoluminescent nanostructures, for which we now have the capability of discerning the lifetime and intensity of different regions of the nanostructure with nanometer-scale precision.

Unlike the clusters presented in Chapter 2, we could not confirm the presence of energy transfer for the clusters examined with correlated imaging. Their behavior could be explained in

terms of a superposition of the emission from single QDs, without needing to expand the model to include energy transfer. In addition, we showed that knowing the lifetime and intensity of the individual QDs within cluster of QDs would not provide sufficient information for extracting the rate of energy transfer. At a minimum, quantifying the energy transfer rate would require knowledge about the lifetime or intensity of one of the QDs within the cluster when it is isolated. While we are capable of measuring the lifetime and intensity of isolated QDs, these are significantly different for each QD, which means the values we select for the single QD will dictate the energy transfer rate that we extract.

A discovery was made in Chapter 4 when we sought to explain the relationship between the intensities and lifetime of different single QDs. The tail of the distribution for *every* single QD showed the intensity was linearly proportional to the lifetime. The tail behavior could be explained by a system containing a nonradiative and radiative pathway for which the nonradiative pathway turns on and off and there are no modifications to the radiative rate.

Much of this thesis was devoted to constructing likelihood distributions for the location of an emitter given the counts collected in our four-pixel detection scheme. The likelihood distribution is maximized to identify the most likely location of the emitter. In Chapter 3, we took readers through the derivation of a distribution that is widely used in SR literature. A significant assumption of CW excitation is made in this formulation, and we were wary of using this likelihood distribution for analyzing our data given that we used pulsed excitation.

In Chapter 5, we returned to the formulation of a likelihood distribution for the emitter location because we were interested in incorporating the photon arrival time information that is recorded in each pixel, suspecting that would increase the amount of information we could extract from our system. In Chapters 2-4, our position analysis had been agnostic to the arrival times in

each pixel. The new likelihood distribution formulated in Chapter 5 allowed us to incorporate the photon arrival time information into the localization procedure, and we demonstrated that the temporal information is beneficial when identifying emitters in the presence of high levels of background. An unintended benefit to formulating the time-resolved likelihood distribution was that it correctly accounted for the pulsed excitation. In Chapter 6, we extended the time-resolved likelihood distribution so that it anticipated the presence of two emitters. This allowed us to identify the locations of two simulated emitters by maximizing the distribution, provided they have disparate lifetimes.

Currently, our group is applying the time-resolved likelihood distribution to analyze experimental data from several different systems. We are examining DNA templates with a dye molecule and QD separated by known distances for which we will be able to localize both the dye and QD using the time-resolved likelihood distribution. We will also attempt to quantify the rate of energy transfer between the QD and the dye. In addition, we are examining "tadpole" nanostructures[105] which have unique lifetimes associated with the head and tail portions of the structure.

For sufficient photon counts, the localization precision of the time-resolved distribution is smaller than the size of a single QD. The bi-exponential decay rates that we observed in single QDs may be evidence that two radiative decay pathways exist. If one of these pathways is caused by a localized defect on the QD, our method should be able to identify its location. We will pursue this hypothesis in the future.

# REFERENCES


[1] Ekimov AI, Efros AL, Onushchenko AA. Quantum size effect in semiconductor microcrystals. Solid State Commun 1985;56:921–4. https://doi.org/10.1016/S0038-1098(85)80025-9.

[2] Kuno M. Model Quantum Mechanics Problems. Introd. Nanosci. Phys. Chem. Concepts, Garland Science; 2012, p. 137–78.

[3] Brus LE. Electron-electron and electron-hole interactions in small semiconductor crystallites: The size dependence of the lowest excited electronic state. J Chem Phys 1984;80:4403. https://doi.org/10.1063/1.447218.

[4] Ekimov AI, Hache F, Ricard D, Flytzanis C. Absorption and intensity-dependent photoluminescence measurements on CdSe quantum dots: assignment of the first electronic transitions. J Opt Soc Am 1993;10:100–7.

[5] Efros AL, Rosen M. The electronic structure of semiconductor nanocrystals. Annu Ev Mat Sci 2000;30.

[6] Barceló I, Guijarro N, Lana-Villarreal T, Gómez R. Recent Progress in Colloidal Quantum Dot-Sensitized Solar Cells. Quantum Dot Sol. Cells, Springer, New York, NY; 2014, p. 1–38. https://doi.org/10.1007/978-1-4614-8148-5_1.

[7] Kim T, Kim KH, Kim S, Choi SM, Jang H, Seo HK, et al. Efficient and stable blue quantum dot light-emitting diode. Nature 2020;586:385–9. https://doi.org/10.1038/s41586-020-2791-x.

[8] Park YS, Roh J, Diroll BT, Schaller RD, Klimov VI. Colloidal quantum dot lasers. Nat Rev Mater 2021;6:382–401. https://doi.org/10.1038/s41578-020-00274-9.

[9] Wegner KD, Hildebrandt N. Quantum dots: Bright and versatile in vitro and in vivo fluorescence imaging biosensors. Chem Soc Rev 2015;44:4792–834. https://doi.org/10.1039/c4cs00532e.

[10] Sayevich V, Robinson ZL, Kim Y, Kozlov O V., Jung H, Nakotte T, et al. Highly versatile near-infrared emitters based on an atomically defined HgS interlayer embedded into a CdSe/CdS quantum dot. Nat Nanotechnol 2021;16:673–9. https://doi.org/10.1038/s41565-021-00871-x.

[11] Bentolila LA. Photoluminescent quantum dots in imaging, diagnostics and therapy. Appl. Nanosci. Photomed., Cambridge: Woodhead Publishing; 2015, p. 77–104. https://doi.org/10.1533/9781908818782.77.

[12] Nirmal M, Dabbousi BO, Bawendi MG, Macklin JJ, Trautman JK, Harris TD, et al. Fluorescence intermittency in single cadmium selenide nanocrystals. Nat Lett 1996;383:802–4.

[13] Efros AL, Rosen M. Random Telegraph Signal in the Photoluminescence Intensity of a

Single Quantum Dot. Phys Rev Lett 1997;78:1110–3.

[14] Shimizu KT, Neuhauser RG, Leatherdale CA, Empedocles SA, Woo WK, Bawendi MG. Blinking statistics in single semiconductor nanocrystal quantum dots. Phys Rev B 2001;63. https://doi.org/10.1103/PhysRevB.63.205316.

[15] Efros AL, Nesbitt DJ. Origin and control of blinking in quantum dots. Nat Nanotechnol 2016;11:661–71. https://doi.org/10.1038/NNANO.2016.140.

[16] Rosen S, Schwartz O, Oron D. Transient Fluorescence of the Off State in Blinking CdSe/CdS/ZnS Semiconductor Nanocrystals Is Not Governed by Auger Recombination. PRL 2010;104. https://doi.org/10.1103/PhysRevLett.104.157404.

[17] Neuhauser RG, Shimizu KT, Woo WK, Empedocles SA, Bawendi MG. Correlation between Fluorescence Intermittency and Spectral Diffusion in Single Semiconductor Quantum Dots. Phys Rev Lett 2000;85.

[18] Galland C, Ghosh Y, Steinbrück A, Sykora M, Hollingsworth JA, Klimov VI, et al. Two types of luminescence blinking revealed by spectroelectrochemistry of single quantum dots. Nature 2011;479:203–7. https://doi.org/10.1038/nature10569.

[19] Peterson JJ, Nesbitt DJ. Modified Power Law Behavior in Quantum Dot Blinking: A Novel Role for Biexcitons and Auger Ionization. Nano Lett 2009;9.

[20] Chepic D, Efros L, Ekimov A, Ivanov M, Kharchenko V, Kudriavtsev lA, et al. Auger ionization of semiconductor quantum drops in a glass matrix. J Lumin 1990;47:113–27.

[21] Kuno M, Fromm DP, Hamann HF, Gallagher A, Nesbitt DJ. “On”/“off” fluorescence intermittency of single semiconductor quantum dots. J Chem Phys 2001;115:3117. https://doi.org/10.1063/1.1377883.

[22] Yuan G, Gómezgómez DE, Kirkwood N, Boldt K, Mulvaney P. Two Mechanisms Determine Quantum Dot Blinking Article. ACS Nano 2018;12. https://doi.org/10.1021/acsnano.7b09052.

[23] Klimov VI, Mikhailovsky AA, Mcbranch DW, Leatherdale CA, Bawendi MG. Quantization of Multiparticle Auger Rates in Semiconductor Quantum Dots Downloaded from. Sci Reports 2000;287.

[24] Mahler B, Spinicelli P, Buil S, Quelin X, Hermier JP, Dubertret B. Towards non-blinking colloidal quantum dots. Nat Mater 2008;7:659–64. https://doi.org/10.1038/nmat2222.

[25] Xie R, Kolb U, Li J, Basché T, Mews A. Synthesis and Characterization of Highly Luminescent CdSe-Core CdS/Zn 0.5 Cd 0.5 S/ZnS Multishell Nanocrystals. J Am Chem Soc 2005;127. https://doi.org/10.1021/ja042939g.

[26] Peng X, Schlamp MC, Kadavanich A V, Alivisatos AP. Epitaxial Growth of Highly Luminescent CdSe/CdS Core/Shell Nanocrystals with Photostability and Electronic Accessibility. J Am Chem Soc 1997;119.

[27] Reiss P, Protière M, Li L. Core/Shell Semiconductor Nanocrystals. Small 2009;5:154–68. https://doi.org/10.1002/smll.200800841.

[28] Orfield NJ, Majumder S, Hu Z, Yik- F, Koh C, Htoon H, et al. Kinetics and Thermodynamics of Killing a Quantum Dot. Cite This ACS Appl Mater Interfaces 2020;12:30701. https://doi.org/10.1021/acsami.0c05980.

[29] Pal BN, Ghosh Y, Brovelli S, Laocharoensuk R, Klimov VI, Hollingsworth JA, et al. "Giant" CdSe/CdS core/shell nanocrystal quantum dots as efficient electroluminescent materials: Strong influence of shell thickness on light-emitting diode performance. Nano Lett 2012;12:331–6. https://doi.org/10.1021/nl203620f.

[30] Kagan CR, Murray CB, Nirmal M, Bawendi MG. Electronic Energy Transfer in CdSe Quantum Dot Solids. 1996.

[31] Kagan CR, Murray CB, Bawendi MG. Long-range resonance transfer of electronic excitations in close-packed CdSe quantum-dot solids 1996;54:8633–43.

[32] Algar WR, Massey M, Krull UJ. Semiconductor Quantum Dots and FRET. FRET - Förster Reson. Energy Transf. From Theory to Appl., Wiley-VCH Verlag; 2013, p. 475–605. https://doi.org/10.1002/9783527656028.ch12.

[33] Kodaimati MS, Lian S, Schatz GC, Weiss EA. Energy transfer-enhanced photocatalytic reduction of protons within quantum dot light-harvesting-catalyst assemblies. PNAS 2018;115:8290–5. https://doi.org/10.1073/pnas.1805625115.

[34] Chou KF, Dennis AM. Förster resonance energy transfer between quantum dot donors and quantum dot acceptors. Sensors (Switzerland) 2015;15:13288–325. https://doi.org/10.3390/s150613288.

[35] Mork AJ, Weidman MC, Prins F, Tisdale WA. Magnitude of the Förster radius in colloidal quantum dot solids. J Phys Chem C 2014;118:13920–8. https://doi.org/10.1021/jp502123n.

[36] Crooker SA, Hollingsworth JA, Tretiak S, Klimov VI. Spectrally Resolved Dynamics of Energy Transfer in Quantum-Dot Assemblies: Towards Engineered Energy Flows in Artificial Materials. Phys Rev Lett 2002;89:18–21. https://doi.org/10.1103/PhysRevLett.89.186802.

[37] Lunz M, Bradley AL, Chen W-Y, Gun'ko YK. Two-Dimensional Förster Resonant Energy Transfer in a Mixed Quantum Dot Monolayer: Experiment and Theory. J Phys Chem 2009;113:3084–8. https://doi.org/10.1021/jp8087034.

[38] Achermann M, Petruska MA, Crooker SA, Klimov VI. Picosecond Energy Transfer in Quantum Dot Langmuir-Blodgett Nanoassemblies. J Phys Chem B 2003;107:13782–7. https://doi.org/10.1021/jp036497r.

[39] Kim D, Okahara S, Nakayama M, Shim Y. Experimental verification of Förster energy transfer between semiconductor quantum dots. Phys Rev B 2008;78. https://doi.org/10.1103/PhysRevB.78.153301.

[40] Moreels I, Justo Y, Rainò G, Stöferle T, Hens Z, Mahrt RF, et al. Impact of the Band-Edge Fine Structure on the Energy Transfer between Colloidal Quantum Dots. Adv Opt Mater 2014;2:126–30. https://doi.org/10.1002/adom.201300263.

[41] Yu M, Van Orden A. Enhanced fluorescence intermittency of CdSe-ZnS quantum-dot

clusters. Phys Rev Lett 2006;97:1–4. https://doi.org/10.1103/PhysRevLett.97.237402.

[42] Shepherd DP, Whitcomb KJ, Milligan KK, Goodwin PM, Gelfand MP, Van Orden A. Fluorescence intermittency and energy transfer in small clusters of semiconductor quantum dots. J Phys Chem C 2010;114:14831–7. https://doi.org/10.1021/jp105150x.

[43] Whitcomb KJ, Geisenhoff JQ, Ryan DP, Gelfand MP, Van Orden A. Photon Antibunching in Small Clusters of CdSe/ZnS Core/Shell Quantum Dots. J Phys Chem B 2015;119:9020–8. https://doi.org/10.1021/jp5083856.

[44] Small AR, Stahlheber S. Fluorophore localization algorithms for super-resolution microscopy. Nat Methods 2014;11:267–79. https://doi.org/10.1038/nmeth.2844.

[45] Sage D, Kirshner H, Pengo T, Stuurman N, Min J, Manley S, et al. Quantitative evaluation of software packages for single-molecule localization microscopy. Nat Methods 2015;12. https://doi.org/10.1038/nmeth.3442.

[46] Li H, Vaughan JC. Switchable Fluorophores for Single-Molecule Localization Microscopy. Chem Rev 2018;118:9412–54. https://doi.org/10.1021/acs.chemrev.7b00767.

[47] Vu TQ, Lam WY, Hatch EW, Lidke DS. Quantum dots for quantitative imaging: from single molecules to tissue. Cell Tissue Res 2015;360:71–86. https://doi.org/10.1007/s00441-014-2087-2.

[48] Petryayeva E, Algar WR, Medintz IL. Quantum dots in bioanalysis: A review of applications across various platforms for fluorescence spectroscopy and imaging. Appl Spectrosc 2013;67:215–52. https://doi.org/10.1366/12-06948.

[49] Ryan DP, Goodwin PM, Sheehan CJ, Whitcomb KJ, Gelfand MP, Van Orden A. Mapping Emission from Clusters of CdSe/ZnS Nanoparticles. J Phys Chem C 2018;122:4046–53. https://doi.org/10.1021/acs.jpcc.7b10924.

[50] Ryan DP, Goodwin PM, Sheehan CJ, Whitcomb KJ, Gelfand MP, Van Orden A. Correlating structure and fluorescence dynamics of quantum dot clusters using super-resolution imaging. Single Mol Spectrosc Superresolution Imaging IX 2016;9714:97140T. https://doi.org/10.1117/12.2211150.

[51] Dunlap MK, Ryan DP, Goodwin PM, Werner JH, Majumder S, Hollingsworth JA, et al. Super-resolution photoluminescence lifetime and intensity mapping of interacting CdSe/CdS quantum dots. Appl Phys Lett 2020;116:021103. https://doi.org/10.1063/1.5132563.

[52] Whitcomb KJ, Ryan DP, Gelfand MP, Van Orden A. Blinking statistics of small clusters of semiconductor nanocrystals. J Phys Chem C 2013;117:25761–8. https://doi.org/10.1021/jp407659y.

[53] Huszka G, Gijs MAM. Super-resolution optical imaging: A comparison. Micro Nano Eng 2019;2:7–28. https://doi.org/10.1016/J.MNE.2018.11.005.

[54] Von Diezmann A, Shechtman Y, Moerner WE. Three-Dimensional Localization of Single Molecules for Super-Resolution Imaging and Single-Particle Tracking 2017. https://doi.org/10.1021/acs.chemrev.6b00629.

[55] Yildiz A, Forkey JN, McKinney SA, Ha T, Goldman YE, Selvin PR. Myosin V walks hand-over-hand: Single fluorophore imaging with 1.5-nm localization. Science 2003;300:2061–5. https://doi.org/10.1126/science.1084398.

[56] Weisenburger S, Boening D, Schomburg B, Giller K, Becker S, Griesinger C, et al. Cryogenic optical localization provides 3D protein structure data with Angstrom resolution. Nat Methods 2017;14:141–4. https://doi.org/10.1038/nmeth.4141.

[57] Israel Y, Tenne R, Oron D, Silberberg Y. Quantum correlation enhanced super-resolution localization microscopy enabled by a fibre bundle camera. Nat Commun 2017;8:1–5. https://doi.org/10.1038/ncomms14786.

[58] Antolovic IM, Burri S, Bruschini C, Hoebe RA, Charbon E. SPAD imagers for super resolution localization microscopy enable analysis of fast fluorophore blinking. Sci Rep 2017;7:1–11. https://doi.org/10.1038/srep44108.

[59] Castello M, Tortarolo G, Buttafava M, Deguchi T, Villa F, Koho S, et al. SI. A robust and versatile platform for image scanning microscopy enabling super-resolution FLIM. Nat Methods 2019;16:175–8. https://doi.org/10.1038/s41592-018-0291-9.

[60] Krishnaswami V, Van Noorden CJF, Manders EMM, Hoebe RA. Towards digital photon counting cameras for single-molecule optical nanoscopy. Opt Nanoscopy 2014;3:1. https://doi.org/10.1186/2192-2853-3-1.

[61] Bronzi D, Villa F, Tisa S, Tosi A, Zappa F. SPAD Figures of Merit for Photon-Counting, Photon-Timing, and Imaging Applications: A Review. IEEE Sens J 2016;16:3–12. https://doi.org/10.1109/JSEN.2015.2483565.

[62] Aßmann M. Quantum-Optically Enhanced STORM (QUEST) for Multi-Emitter Localization. Sci Rep 2018;8:7829. https://doi.org/10.1038/s41598-018-26271-1.

[63] Lessard GA, Goodwin PM, Werner JH. Three-dimensional tracking of individual quantum dots. Appl Phys Lett 2007;91:22–5. https://doi.org/10.1063/1.2819074.

[64] Wells NP, Lessard GA, Goodwin PM, Phipps ME, Cutler PJ, Lidke DS, et al. Tracking in Live Cells 2010:4732–7. https://doi.org/10.1021/nl103247v.

[65] Keller AM, Ghosh Y, Devore MS, Phipps ME, Stewart MH, Wilson BS, et al. 3-Dimensional tracking of non-blinking “giant” quantum dots in live cells. Adv Funct Mater 2014;24:4796–803. https://doi.org/10.1002/adfm.201400349.

[66] Keller AM, Devore MS, Stich DG, Vu DM, Causgrove T, Werner JH. Multicolor Three-Dimensional Tracking for Single-Molecule Fluorescence Resonance Energy Transfer Measurements. Anal Chem 2018;90:51. https://doi.org/10.1021/acs.analchem.8b00244.

[67] Chen O, Zhao J, Chauhan VP, Cui J, Wong C, Harris DK, et al. Compact high-quality CdSe-CdS core-shell nanocrystals with narrow emission linewidths and suppressed blinking. Nat Mater 2013;12:445–51. https://doi.org/10.1038/nmat3539.

[68] Hell SW, Sahl SJ, Bates M, Zhuang X, Heintzmann R, Booth MJ, et al. The 2015 super-resolution microscopy roadmap. J Phys D Appl Phys 2015;48. https://doi.org/10.1088/0022-3727/48/44/443001.

[69] Castello M, Tortarolo G, Buttafava M, Deguchi T, Villa F, Koho S, et al. A robust and versatile platform for image scanning microscopy enabling super-resolution FLIM. Nat Methods 2019;16:175–8. https://doi.org/10.1038/s41592-018-0291-9.

[70] Thiele JC, Helmerich DA, Oleksiievets N, Tsukanov R, Butkevich E, Sauer M, et al. Confocal Fluorescence-Lifetime Single-Molecule Localization Microscopy n.d. https://doi.org/10.1021/acsnano.0c07322.

[71] Smith CS, Joseph N, Rieger B, Lidke KA. Fast, single-molecule localization that achieves theoretically minimum uncertainty. Nat Methods 2010;7:373–5. https://doi.org/10.1038/nmeth.1449.

[72] Jungmann R, Avendaño MS, Dai M, Woehrstein JB, Agasti SS, Feiger Z, et al. Quantitative super-resolution imaging with qPaint. Nature 2016;13:439. https://doi.org/10.1038/nmeth.3804.

[73] Rust MJ, Bates M, Zhuang X. Sub-diffraction-limit imaging by stochastic optical reconstruction microscopy (STORM). Nat Methods 2006;3:793–5. https://doi.org/10.1038/nmeth929.

[74] Betzig E, Patterson GH, Sougrat R, Lindwasser OW, Olenych S, Bonifacino JS, et al. Imaging intracellular fluorescent proteins at nanometer resolution. Science (80- ) 2006;313:1642–5. https://doi.org/10.1126/science.1127344.

[75] Sharonov A, Hochstrasser RM. Wide-field subdiffraction imaging by accumulated binding of diffusing probes. 2006.

[76] Patterson G, Davidson M, Manley S, Lippincott-Schwartz J. Superresolution Imaging using Single-Molecule Localization 2010. https://doi.org/10.1146/annurev.physchem.012809.103444.

[77] Norris DJ, Nirmal M, Murray CB, Sacra A, Bawendi MG. Size dependent optical spectroscopy of II-VI semiconductor nanocrystallites (quantum dots). Zeitschrift Für Phys D Atoms, Mol Clust 1993;26:355–7. https://doi.org/10.1007/BF01429193.

[78] van Embden J, Jasieniak J, Mulvaney P. Mapping the Optical Properties of CdSe/CdS Heterostructure Nanocrystals: The Effects of Core Size and Shell Thickness. J Am Chem Soc 2009;131:14299–309. https://doi.org/10.1021/ja9030209.

[79] Murray CB, Norris DJ, Bawendi MG. Synthesis and characterization of nearly monodisperse CdE (E = sulfur, selenium, tellurium) semiconductor nanocrystallites. J Am Chem Soc 1993;115:8706–15. https://doi.org/10.1021/ja00072a025.

[80] Press, W. H., Teukolzky, S. A., Vetterling, W. T., and Flannery BP. Least Squares as a Maximum Likelihood Estimator. Numer. Recipes Art Sci. Comput. 3rd ed., Cambridge Univ. Press; 2007, p. 776–7.

[81] Bevington PR. Data reduction and error analysis for the physical sciences. New York: McGraw-Hill; 2003.

[82] Huang T, Junhu S, Wang X, Xiao L, Jia S. Photon emission characteristics of avalanche photodiodes. Opt Eng 2005;44:074001. https://doi.org/10.1117/1.1950087.

[83] Press, W. H., Teukolzky, S. A., Vetterling, W. T., and Flannery BP. Downhill Simplex Method in Multidimensions. Numer. Recipes Art Sci. Comput. 3rd ed., Cambridge Univ. Press; 2007, p. 502–7.

[84] Bevington, P. R., Robinson DK. Direct Application of the Maximum-Likelihood Method. Data Reduct. Error Anal. Phys. Sci. Ed. 3, 2003, p. 190–1.

[85] Gutiérrez-Arzaluz L, Ahmed GH, Yang H, Shikin S, Bakr OM, Malko A V., et al. Correlation of Photoluminescence and Structural Morphologies at the Individual Nanoparticle Level. J Phys Chem A 2020;124:4855–60. https://doi.org/10.1021/acs.jpca.0c02340.

[86] Orfield NJ, Mcbride JR, Keene JD, Davis LM, Rosenthal SJ. Correlation of Atomic Structure and Photoluminescence of the Same Quantum Dot: Pinpointing Surface and Internal Defects That Inhibit Photoluminescence 2014. https://doi.org/10.1021/nn506420w.

[87] McBride JR, Mishra N, Click SM, Orfield NJ, Wang F, Acharya K, et al. Role of shell composition and morphology in achieving single-emitter photostability for green-emitting "giant" quantum dots. J Chem Phys 2020;152:124713. https://doi.org/10.1063/5.0002772.

[88] Rutherford E, Soddy F. Radioactive Change. Philos Mag 1903;5:576–91. https://doi.org/10.1080/14786440309462960.

[89] Qin W, Shah RA, Guyot-Sionnest P. CdSeS/ZnS Alloyed Nanocrystal Lifetime and Blinking Studies under Electrochemical Control. ACS Nano 2012;6. https://doi.org/10.1021/nn2044388.

[90] Lindhoud S, Westphal AH, Van Mierlo CPM, Visser AJWG, Borst JW. Rise-time of FRET-acceptor fluorescence tracks protein folding. Int J Mol Sci 2014;15:23836–50. https://doi.org/10.3390/ijms151223836.

[91] Small AR, Parthasarathy R. The Annual Review of Physical Chemistry is online at. Annu Rev Phys Chem 2014;65:107–25. https://doi.org/10.1146/annurev-physchem-040513-103735.

[92] Kuno M. Time-Dependent Pertubation Theory. Introd. Nanosci. Phys. Chem. Concepts, Garland Science; 2012.

[93] Dunlap MK, Ryan DP, Goodwin PM, Werner JH, Majumder S, Hollingsworth JA, et al. Single molecule localization with four avalanche photodiode detectors. In: Gregor I, Erdmann R, Koberling F, editors. Single Mol. Spectrosc. Superresolution Imaging XIII, vol. 11246, SPIE; 2020, p. 23. https://doi.org/10.1117/12.2546573.

[94] Hermon K, Schidorsky S, Razvag Y, Yakovian O, Sherman E. Time-correlated single molecule localization microscopy enhances resolution and fidelity. Sci Rep 2020;10:16212. https://doi.org/10.1038/s41598-020-72812-y.

[95] Schwartz O, Oron D. Improved resolution in fluorescence microscopy using quantum correlations. Phys Rev A 2012;85:33812. https://doi.org/10.1103/PhysRevA.85.033812.

[96] Schwartz O, Levitt JM, Tenne R, Itzhakov S, Deutsch Z, Oron D. Superresolution Microscopy with Quantum Emitters. Nano Lett 2013;13:5832–6.

https://doi.org/10.1021/nl402552m.

[97] Tenne R, Rossman U, Rephael B, Israel Y, Krupinski-Ptaszek A, Lapkiewicz R, et al. Super-resolution enhancement by quantum image scanning microscopy. Nat Photonics 2019;13:116–22. https://doi.org/10.1038/s41566-018-0324-z.

[98] Heilemann M, Herten DP, Heintzmann R, Cremer C, Muller C, Tinnefeld P, et al. High-Resolution Colocalization of Single Dye Molecules by Fluorescence Lifetime Imaging Microscopy. AnalChem 2002;74:3511–7. https://doi.org/10.1021/ac025576g.

[99] Heinlein T, Biebricher A, Schlüter P, Roth CM, Herten D-P, Wolfrum J, et al. High-Resolution Colocalization of Single Molecules within the Resolution Gap of Far-Field Microscopy. ChemPhysChem 2005;6:949–55. https://doi.org/10.1002/cphc.200400622.

[100] Ryan D, Dunlap MK, Majumder S, Sheehan CJ, Werner JH, Hollingsworth JA, et al. Dual-color super-resolution imaging of quantum dot clusters. Proc SPIE Single Mol Spectrosc Superresolution Imaging XIII 2020;11246:10. https://doi.org/10.1117/12.2542352.

[101] Gunkel M, Erdel F, Rippe K, Lemmer P, Kaufmann R, Hörmann C, et al. Dual color localization microscopy of cellular nanostructures. Biotechnol J 2009;4:927–38. https://doi.org/10.1002/biot.200900005.

[102] Yan R, Moon S, Kenny SJ, Xu K. Spectrally Resolved and Functional Super-resolution Microscopy via Ultrahigh-Throughput Single-Molecule Spectroscopy. Acc Chem Res 2018;51:697–705. https://doi.org/10.1021/acs.accounts.7b00545.

[103] Huang J-H, Teng C-M, Hsiao Y-S, Yen F-W, Chen P, Chang F-C, et al. Nanoscale Correlation between Exciton Dissociation and Carrier Transport in Silole-Containing Cyclopentadithiophene-Based Bulk Heterojunction Films. J Phys Chem C 2011;115:14. https://doi.org/10.1021/jp1090894.

[104] Huang J-H, Li K-C, Chien F-C, Hsiao Y-S, Kekuda D, Chen P, et al. Correlation between Exciton Lifetime Distribution and Morphology of Bulk Heterojunction Films after Solvent Annealing. J Phys Chem 2010;114:9062–9. https://doi.org/10.1021/jp9120639.

[105] Deutsch Z, Schwartz O, Tenne R, Popovitz-Biro R, Oron D. Two-color antibunching from band-gap engineered colloidal semiconductor nanocrystals. Nano Lett 2012;12:2948–52. https://doi.org/10.1021/nl300638t.

[106] Anderson NC, Hendricks MP, Choi JJ, Owen JS. Ligand Exchange and the Stoichiometry of Metal Chalcogenide Nanocrystals: Spectroscopic Observation of Facile Metal-Carboxylate Displacement and Binding Scheme 1. Nanocrystal Ligand Binding Motifs According to the Covalent Bond Classification Method. J Am Chem Soc 2013;25:29. https://doi.org/10.1021/ja4086758.

[107] Mangum BD, Ghosh Y, Hollingsworth JA, Htoon H. Disentangling the effects of clustering and multi-exciton emission in second-order photon correlation experiments. Opt Express 2013;21:7419. https://doi.org/10.1364/oe.21.007419.

[108] DeVore MS, Stich DG, Keller AM, Ghosh Y, Goodwin PM, Phipps ME, et al. Three dimensional time-gated tracking of non-blinking quantum dots in live cells. Proc SPIE 9338 2015:933812. https://doi.org/10.1117/12.2082943.

[109] Vicidomini G, Schönle A, Ta H, Han KY, Moneron G, Eggeling C, et al. STED Nanoscopy with Time-Gated Detection: Theoretical and Experimental Aspects. PLosS ONE 2013;8. https://doi.org/10.1371/journal.pone.0054421.

[110] Moffitt JR, Osseforth C, Michaelis J. Time-gating improves the spatial resolution of STED microscopy. Opt Express 2011;19:4242–54. https://doi.org/10.1364/oe.19.004242.

[111] Vicidomini G, Ta H, Honigmann A, Mueller V, Clausen MP, Waithe D, et al. STED-FLCS: An Advanced Tool to Reveal Spatiotemporal Heterogeneity of Molecular Membrane Dynamics. Nano Lett 2015;15:5912–8. https://doi.org/10.1021/acs.nanolett.5b02001.

# LIST OF ABBREVIATIONS

| | |
|---|---|
| APD | avalanche photodiode |
| CCD | charge-coupled device |
| CW | continuous wavelength |
| FCS | fluorescence correlation spectroscopy |
| FRET | Förster resonance energy transfer |
| HOMO | highest occupied molecular orbital |
| IR | infrared |
| IRF | instrument response function |
| LP | long pass |
| LUMO | lowest unoccupied molecular orbital |
| MLE | maximum likelihood estimation |
| NA | numerical aperture |
| NIM | nuclear instrumentation module |
| PSF | point spread function |
| QD | quantum dot |
| SMLM | single molecule localization spectroscopy |
| SP | short pass |
| SPAD | single photon avalanche photodiode |
| SR | super-resolution |
| STED | stimulated emission depletion |
| TCSPC | time-correlated single photon counting |
| TIRF | total internal reflection |
| TR | time-resolved |
| TTL | transistor-transistor logic |